This is the peer-reviewed, final accepted version for American Mineralogist, published by the Mineralogical Society of America.
The published version is subject to change. Cite as Authors (Year) Title. American Mineralogist, in press.
DOI: https://doi.org/10.2138/am-2021-7938. http://www.minsocam.org/

MSA REVIEW PAPER:

Pauling's rules for oxide-based minerals-A re-examination based on quantum mechanical constraints and modern applications of bond-valence theory to earth materials

Gerald V. Gibbs[1], Frank C. Hawthorne[2], and Gordon E. Brown, Jr.[3,*]
[1]Departments of Geosciences and Materials Science and Engineering, Virginia Tech, Blacksburg, VA 24061, USA
[2] Department of Geological Sciences, University of Manitoba, Winnipeg, MB R3T 2n2, CANADA
[3] Department of Geological Sciences, School of Earth, Energy & Environmental Sciences, Stanford University, Stanford, CA 94305-2115, USA

Submitted to American Mineralogist: Journal of Earth and Planetary Materials
on December 22, 2020 and re-submitted in revised form on May 15, 2021

Abstract

Since their introduction in 1929, Pauling's five rules have been used by scientists from many disciplines to rationalize and predict stable arrangements of atoms and coordination polyhedra in crystalline solids; amorphous materials such as silicate glasses and melts; nanomaterials, poorly crystalline solids; aqueous cation and anion complexes; and sorption complexes at mineral-aqueous solution interfaces. The predictive power of these simple yet powerful rules was challenged recently by George et al. (2020), who performed a statistical analysis of the performance of Pauling's five rules for about 5,000 oxide crystal structures. They concluded that only 13% of the oxides satisfy the last four rules simultaneously and that the second rule has the most exceptions. They also found that Pauling's first rule is satisfied for only 66% of the coordination environments tested and concluded that no simple rule linking ionic radius to coordination environment will be predictive due to the variable quality of univalent radii.

This is the peer-reviewed, final accepted version for American Mineralogist, published by the Mineralogical Society of America.
The published version is subject to change. Cite as Authors (Year) Title. American Mineralogist, in press.
DOI: https://doi.org/10.2138/am-2021-7938. http://www.minsocam.org/

We address these concerns and discuss quantum mechanical calculations that complement Pauling's rules, particularly his first (radius sum and radius ratio rule) and second (electrostatic valence rule) rules. We also present a more realistic view of the bonded radii of atoms, derived by determining the local minimum in the electron density distribution measured along trajectories between bonded atoms known as bond paths, i.e., the bond critical point (r_c). Electron density at the bond critical point is a quantum mechanical observable that correlates well with Pauling bond strength. Moreover, a metal atom in a polyhedron has as many bonded radii as it has bonded interactions, resulting in metal and oxygens atoms that may not be spherical. Oxygen atoms, for example, are not spherical in many oxide-based crystal structures. Instead, the electron density of a bonded oxygen is often highly distorted or polarized, with its bonded radius decreasing systematically from ~1.38 Å when bonded to highly electropositive atoms like sodium to 0.64 Å when bonded to highly electronegative atoms like nitrogen. Bonded radii determined for metal atoms match the Shannon (1976) radii for more electropositive atoms, but the match decreases systematically as the electronegativities of the M atoms increase. As a result, significant departures from the radius ratio rule in the analysis by George et al. (2020) is not surprising. We offer a modified, more fundamental version of Pauling's first rule and demonstrate that the second rule has a one-to-one connection between the electron density accumulated between the bonded atoms at the bond critical point and the Pauling bond strength of the bonded interaction.

Pauling's second rule implicitly assumes that bond strength is invariant with bond length for a given pair of bonded atoms. Many studies have since shown that this is not the case, and Brown and Shannon (1973) developed an equation and a set of parameters to describe the relation between bond length and bond strength, now redefined as bond valence to avoid confusion with Pauling bond-strength. Brown (1980) used the valence-sum rule, together with the path rule and

the valence-matching principle, as the three axioms of Bond-Valence Theory (BVT), a powerful method for understanding many otherwise elusive aspects of crystals and also their participation in dynamic processes. We show how a priori bond-valence calculations can predict unstrained bond-lengths and how bond-valence mapping can locate low-Z atoms in a crystal structure (e.g., Li) or examine possible diffusion pathways for atoms through crystal structures.

In addition, we briefly discuss Pauling's third, fourth, and fifth rules, the first two of which concern the sharing of polyhedron elements (edges and faces) and the common instability associated with structures in which a polyhedron shares an edge or face with another polyhedron and contains high-valence cations. The olivine (α-$(Mg_xFe_{1-x})_2SiO_4$) crystal structure is used to illustrate the distortions from hexagonal close-packing of oxygens caused by metal-metal repulsion across shared polyhedron edges.

We conclude by discussing several applications of BVT to Earth materials, including the use of BVT to (1) locate H^+ ions in crystal structures, including the location of protons in the crystal structures of nominally anhydrous minerals in Earth's mantle, (2) determine how strongly bonded (usually anionic) structural units interact with weakly bonded (usually cationic) interstitial complexes in complex uranyl-oxide and uranyl-oxysalt minerals using the valence-matching principle, (3) calculate Lewis acid strengths of cations and Lewis base strengths of anions, (4) determine how (H_2O) groups can function as bond-valence transformers by dividing one bond into two bonds of half the bond valence, (5) help characterize products of sorption reactions of aqueous cations (e.g., Co^{2+} and Pb^{2+}) and oxyanions (e.g., selenate $(Se^{6+}O_4)^{2-}$ and selenite $(Se^{4+}O_3)^{2-}$) at mineral-aqueous solution interfaces and the important role of protons in these reactions, and (6) help characterize the local coordination environments of highly charged cations (e.g., Zr^{4+}, Ti^{4+}, U^{4+}, U^{5+}, and U^{6+}) in silicate glasses and melts.

Keywords: Pauling's Rules, Bonded Radii, Bonded Interactions, Bond Paths, Bond Valence Theory, Bond Valence Analysis of Crystal Structures, Bond Valence Analysis of Water in Nominally Anhydrous Mantle Minerals, Bond Valence Analysis of Proton, Cation, and Oxyanion Sorption Complexes, Application of Bond-Valence Theory to Uranyl-Oxide and Uranyl-Oxysalt Minerals, Bond-Valence Analysis of Proton, Cation, and Oxyanion Adsorption at Mineral-Aqueous Solution Interfaces, Bond-Valence and XAFS Analysis of the Local Coordination Environments of Highly Charged Cations in Silicate Glasses

INTRODUCTION

Although the concept of atoms and their indivisible nature dates back to the ideas of Leucippus and his student Democritus in 440 B.C.E., John Dalton (1808) formulated the first modern description of atoms as the fundamental, non-destructible, spherical building blocks of all matter. Dalton also suggested that the atoms of a given element are identical, that different atoms have different sizes and masses, and that all materials consist of combinations of atoms in well-defined ratios (the law of definite composition and its extension - the law of multiple proportions). Further, the product of a chemical reaction was considered to result in a rearrangement of the reacting atoms. But the structures of the reaction products were unknown until William Barlow (1883,1894) speculated that the Na and Cl atoms in a cubic crystal of rock salt are spherical and arranged in a periodic close-packed chessboard pattern in 3-space. Barlow (as well as Evgraf Fedorov and Arthur Moritz Schoenflies) also deduced that there are only 230 unique ways of arranging symmetry elements in 3-space (the space groups) that describe the symmetry of any periodic array of atoms in a crystalline material. His insightful conjecture that the atoms in halite are arranged in a three-dimensional periodic pattern preceded by 30 years the famous X-ray diffraction experiments on sphalerite crystals by Max von Laue and his colleagues Walter Friedrich and Paul Knipping (Friedrich et al., 1912). Based on these results, Sir Lawrence Bragg and his father Sir William H. Bragg were quick to recognize the significance of Barlow's conjecture and von Laue's X-ray diffraction patterns (W. H. Bragg, 1912; W. L. Bragg, 1913a,b;

W. H. Bragg and W. L. Bragg, 1913). Primed with the knowledge that atoms in crystals are arranged in periodic patterns in 3-space, and that the dimensions of the atoms are comparable to the wavelength of an X-ray beam, the younger Bragg re-interpreted the X-ray diffraction pattern observed by Friedrich et al. (1912) as X-ray reflection by planes of atoms in the crystal. The elder Bragg (1913) built a single-crystal diffractometer, and he and his son recorded diffraction data for a cube of halite that verified Barlow's brilliant speculations. Without a doubt, the determination of the crystal structure of halite was a fundamental breakthrough in understanding the structures of crystals as periodic arrays of bonded atoms in 3-space, a discovery that was not only a great advance in field of crystal chemistry but also the basis for Pauling's rules.

With the advent of X-ray diffraction, early structural crystallographers including Bragg, Goldschmidt, Pauling, Huggins, and Zachariasen interpreted X-ray diffraction patterns within the framework of space group theory and the context of the close packing of spherical atoms, and solved the crystal structures of many minerals and synthetic materials. Bragg (1920) found that interatomic distances in crystals can be reproduced by the sum of the radii of the bonded atoms. In addition, he derived a set of atomic radii where the sum of the radii reproduces the bond lengths for 100's of crystals to within ~ 0.06 Å. Landé (1920) also assumed that halogen ions are in mutual contact in the structures of the lithium halogenides and assigned the sizes of ions accordingly. Hüttig (1920) concluded that the coordination number adopted by cations is determined by radius ratio considerations, the larger the ratio, the larger the expected coordination number of the cations. Using the connection between mole refraction and ionic volume, Wasastjerna (1923) produced a more extensive set of ionic radii that was extended by Goldschmidt (1926) and Pauling (1927). Collectively, this work concluded that anions are larger (over 1.35 Å) than cations. Goldschmidt (1926) used Hüttig's (1920) coordination number arguments to predict coordination numbers for

This is the peer-reviewed, final accepted version for American Mineralogist, published by the Mineralogical Society of America.
The published version is subject to change. Cite as Authors (Year) Title. American Mineralogist, in press.
DOI: https://doi.org/10.2138/am-2021-7938. http://www.minsocam.org/

a wide range of cations. Pauling (1929) collected these ideas, developed others, and consolidated them as a set of relatively simple yet powerful rules for understanding and predicting stable atomic arrangements in oxide-based minerals. The radii of the metal ions were assumed to decrease systematically from left to right in each row of the periodic table and to increase as the row numbers of the atoms increase. Pauling (1929) also observed that individual metal-oxygen (M-O) bond lengths tend to decrease with increasing valence, v, and decreasing coordination number, κ, of the M cation. He defined the strength of an M-O bond as $s = v/\kappa$, and found that the sum of the bond strengths incident at a bonded O^{2-} ion often closely matches the valence of that ion. Pauling (1929) also observed that O-O edges shared between cation-containing oxygen-coordinated polyhedra are shorter than unshared edges, a feature he ascribed to the reduction of the repulsive forces between the metal cations across the shared edge. These ideas about favorable atom arrangements in stable oxide-based structures were incorporated by Pauling (1929, 1960) in the following set of five rules.

Pauling's first rule (Pauling, 1960**)** states that "a coordination polyhedron of anions is formed about each cation, the cation-anion distance being determined by the radius sum and the ligancy of the cation by the radius ratio," a concept that he adopted from Goldschmidt **(**1926**)**. **Pauling's second rule** (Pauling, 1960) postulates that "in a stable ionic structure the valence of each anion with changed sign, is exactly or nearly equal to the sum of the strengths of the electrostatic bonds to it from adjacent corners; that is,

$$\zeta e = \sum s_i = \sum z_i/v_i$$

in which ζe is the electric charge of the anion and the summation is taken over the cations at the centers of all the polyhedral of which the anion forms a corner." This 2nd rule is also known as

the electrostatic valence principle. **Pauling's third rule (**Pauling, 1960**)** states that "the presence of shared edges and especially of shared faces in a coordinated structure decreases its stability; this effect is large for cations with large valence and small ligancy." **The fourth rule (**Pauling, 1960**)** states "in a crystal containing different cations those of large valence and small coordination number tend not to share polyhedral elements with each other," and his **fifth rule (**Pauling, 1929**)** states "the number of essentially different kinds of constituents in a crystal tends to be small."

We also include here a statement by Pauling (1960) concerning how he formulated his "rules": From: Section 13-6: "The Principles Determining the Structure of Complex Ionic Crystals" The Nature of the Chemical Bond (1960) – Third Edition, pp. 543-562. "It has been found possible to formulate a set of rules about the stability of complex ionic crystals, as described in the following paragraphs. These rules were obtained in part by induction from the structures known in 1928 and in part by deduction from the equations for crystal energy. They are not rigorous in their derivation or universal in their application, but they have been found useful as a criterion for the probable correctness of reported structures for complex crystals and as an aid in the x-ray investigation of crystals by making possible the suggestion of reasonable structures for experimental test. The rules are, moreover, of some significance for molecules and complex ions." (Pauling, 1960, pp. 543-544).

"Minerals, including the silicate minerals, many of which have been thoroughly investigated by X-ray methods, provide excellent illustrations for the rules given in the preceding paragraphs. The sulfide minerals, on the other hand, show general lack of agreement with the rules; their bonding is largely covalent." (Pauling, 1960, p. 562).

As is well known, Pauling's rules are based on the approximations that bonded atoms are spherical and that bond lengths are determined by the radius sum of the bonded ions. At the time

This is the peer-reviewed, final accepted version for American Mineralogist, published by the Mineralogical Society of America.
The published version is subject to change. Cite as Authors (Year) Title. American Mineralogist, in press.
DOI: https://doi.org/10.2138/am-2021-7938. http://www.minsocam.org/

these rules were proposed, little was known about the actual sizes and shapes of bonded atoms other than that their radii sum reproduced observed bond lengths. However, electron density distributions recently determined experimentally and calculated theoretically for many minerals show that the radius of the bonded oxygen atom is not fixed but increases systematically in parallel trends as the bonded radii of the M atoms increase (Gibbs et al. 2013a, 2014). In addition, Gibbs et al. (2013a) found strong evidence that the Pauling bond strength-bond length of a M-O bonded interaction is very similar to the average accumulation of the electron density at the bond critical point ($<\rho(\mathbf{r}_c)>$) between bonded pairs of metal and oxygen atoms. On the basis of the correspondence between equations relating $<\rho(\mathbf{r}_c)>$ [$<R(M–O)> = 1.46<\rho(\mathbf{r}_c)>/\mathbf{r}^{-0.19}$] and $<\boldsymbol{s}>$ [$<R(M–O)> = 1.46<\boldsymbol{s}>/\mathbf{r}^{-0.21}$] to bond length, Gibbs et al. (2013a) concluded that the Pauling bond strength might serve as an estimate of the accumulation of electron density between bonded M–O atoms. In these equations, $<\rho(\mathbf{r}_c)>$ is the average electron density accumulated at the bond critical point, $\mathbf{r}_c$, of an M-O bond, <R(M-O)> is the average experimental M-O bond length, $<\boldsymbol{s}>$ is the average Pauling bond strength of an M-O bond, and **r** is the Periodic Table row number of the M atom.

One of our motivations for writing this review paper is to address a recent paper by George et al. (2020) entitled “The Limited Predictive Power of the Pauling Rules”, which questions the applicability of Pauling’s first and second rules in particular, based on a statistical analysis of the success of Pauling’s rules when applied to 5000 or so crystal structures in the Inorganic Crystal Structure Database. George et al. (2020) make the following comment: “Our work therefore calls for the development of new empirical rules beyond the almost one-century old Pauling rules. Our analysis and the data set of connectivity and local environment provided is a first step towards building this new theory……”. This statement ignores the large amount of theoretical and

This is the peer-reviewed, final accepted version for American Mineralogist, published by the Mineralogical Society of America.
The published version is subject to change. Cite as Authors (Year) Title. American Mineralogist, in press.
DOI: https://doi.org/10.2138/am-2021-7938. http://www.minsocam.org/

experimental work done on oxide-based solids since Pauling proposed his rules. In the same spirit of wishing to move forward in understanding and predicting details of inorganic crystal structures, we discuss some of this subsequent work and comment on some future directions that can be pursued.

Other motivations are (1) to examine the relation between Pauling's rules and the results of modern quantum mechanical calculations, (2) to address the common misapprehension that Pauling's rules apply only to "ionic compounds", (3) to review the use of some of these more recent developments and applications of bond-valence theory (BVT) in the fields of mineralogical and inorganic crystallography, inorganic geochemistry, and metal-oxide surface/interface chemistry, and (4) to emphasize that departures from Pauling's rules by specific structures and classes of structures are important indicators of unusual crystal-chemical effects and the possible presence of economically important physical properties.

PRELIMINARY CONSIDERATIONS

Doing science consists of making observations and developing models that order these observations into a rational hierarchy and (if possible) make predictions. Pauling's rules (Pauling, 1929, 1960) are a set of rules (also referred to as "principles" by Pauling himself) that systematize various features of the crystal structures of oxide and oxysalt crystals. Thus, Pauling's rules are a model for oxide and oxysalt crystals, but one that has undergone continuous development to the present time, resulting in better understanding and more accurate prediction of structural features than was possible in 1929. Quantum-mechanical models were also developed around the same

time (1925-1934); they have since undergone immense development and are now applicable to a very wide array of scientific topics. Indeed, quantum-mechanical models such as Density Functional Theory (Hohenberg and Kohn, 1964; Kohn and Sham, 1965) have strongly influenced the evolution of quantum mechanics over the past 50 years and have been so successful in chemistry that there has been a tendency to regard them as "truth" and to criticize alternative models on the basis of their differences from quantum-mechanical models. However, such criticism is irrational as models are human constructs and can only be judged on their success in ordering and predicting the phenomena with which they are concerned. In comparing these predictions with experimental results, poor parameterization will give rise to inaccurate or even erroneous results no matter how sophisticated the theory.

From a mineralogical perspective, both quantum-mechanical methods (e.g., Gatti, 2005; Prencipe, 2019) and methods suggested by Pauling's rules (e.g., Brown 2002a, 2016) are of great importance. As we show here, quantum-mechanical methods can give insight into the detailed behavior of electron density and its derivative physical properties for small, ordered chemical systems, while methods derived from Pauling's rules can give insight into the behavior and properties of large disordered chemical systems. This is an issue of particular importance for mineralogy as the majority of minerals and solid solutions show extensive disorder. The essence of the message here is that both quantum-mechanical methods and those methods suggested by Pauling's rules provide insight into the behavior of minerals in geological and planetary processes, and are not competitive methods.

Stability

This is the peer-reviewed, final accepted version for American Mineralogist, published by the Mineralogical Society of America.
The published version is subject to change. Cite as Authors (Year) Title. American Mineralogist, in press.
DOI: https://doi.org/10.2138/am-2021-7938. http://www.minsocam.org/

Crystallographers, mineralogists, geochemists, and petrologists have different meanings for the word "stability". In crystallography, a crystal structure is stable if it can exist under any external conditions. Thus, the structural arrangement of forsterite (ideally Mg_2SiO_4) is stable because we observe it. A structure of composition Mg_4SiO_4, for example, cannot exist because it is not electroneutral….it is unstable. In mineralogy, geochemistry, and petrology, a mineral is stable where it occurs in equilibrium with a set of external conditions and is unstable where it does not occur in equilibrium with another set of external conditions. Forsterite is stable at high temperature (< 1890°C) and pressure (<136 kb corresponding to depths in the Earth of 0-410 km). Thus, it is important to understand the context in which the term "stability" is used when referring to minerals and mineral structures.

IONIC RADII, BONDED RADII, BONDED INTERACTIONS, AND BOND PATHS

Ionic Radii: Heuristic Considerations

In high-symmetry coordination polyhedra, e.g., in NaCl or MgO structures, all bond lengths are equal and each ion can be considered as spherical, i.e., it has the same radius along each bond. However, in lower-symmetry coordination polyhedra (e.g., $(SiO_4)^{4-}$ in the quartz structure), all bond lengths are not equal and each ion cannot be considered spherical: partitioning a bond length into two parts will give unequal “radii” for the two atoms along each bond. Thus the “radii” of ions in a specific bond-pair must vary with distortion of the coordination polyhedron away from holosymmetry. This is a simple geometrical effect and the behavior of the electron density in the structure must accord with this constraint. This effect will be enhanced where there are non-uniform bond-valence (bond-strength) constraints. Consider the M2 site in diopside: $CaMgSi_2O_6$ (Clark et al., 1969). The O1, O2, and O3 oxygen anions receive Pauling bond-strengths of 1.92, 1.58, and 2.50 v.u. (valence units), respectively. Accordingly, coordination

polyhedra distort to produce the following bond-length ranges for diopside: Si-O: 1.585-1.687 Å: Mg-O: 2.050-2.115 Å; and Ca-O: 2.352-2.717 Å. As a consequence, there will be a wide range of "radii" for each ion along the different bond paths in the diopside structure.

This idea is not new. Pauling and Hendricks (1925) suggested that the distorted octahedral coordination of Al^{3+} and Fe^{3+} in the crystal structures of corundum (α-Al_2O_3) and hematite (α-Fe_2O_3), respectively, result in electrons in the outer shells of these cations having different effective radii in different directions. They concluded that "the structures determined for hematite and corundum show that these crystals consist of a compact arrangement of approximately, but not exactly, spherical ions of oxygen and of iron or aluminum, held together by inter-ionic forces which are probably electrostatic in nature."

According to Shannon (1976), the radius of the [4]-coordinated O^{2-} ion is 1.38 Å – a value that results in a minimum O-O separation of 2.76 Å. Zemann (1986) listed the closest O-O distance not involved in a low-coordination oxyanion (in a silicate) as 2.75 Å, which is very close to the predicted minimum O-O separation. However, O-O distances down to ~ 2.22 Å occur in oxyanions such as $(BO_3)^{3-}$ and $(CO_3)^{2-}$, and as shared edges of coordination polyhedra of highly charged cations (e.g., 2.23 Å in andalusite (Al_2SiO_5); Winter and Ghose, 1979). These values suggest that to ask whether the ionic radius of O^{2-} is correct or not is to ask the wrong question. These numbers suggest that O^{2-} should be considered as a soft sphere that to some extent adapts its radius to its local coordination environment.

Of course, the above simple geometrical argument requires only that the radii in such cases differ along different bond paths. The degree to which they differ may be derived from experimental and/or theoretical electron density distributions (e.g., Gibbs et al., 2013a).

Bonded Radii – A Modern View of the Radii of Atoms

In a study of the structures of molecules and bonded interactions, Slater (1964) argued that the bonded radius of an atom can be determined on the basis of the topology of the electron density distribution that connects bonded atoms. While a Post-Doctoral Fellow at MIT, Richard F. W. Bader undertook a virial partitioning of the distributions of electron density for several molecules and discovered that the only features in the distributions that appear 'bond-like' in nature are ridges of maximum electron density that connect pairs of bonded atoms, ridges that he named bond paths (Runtz et al., 1977). As the electron density distribution is a quantum mechanical observable, any derivative of the distribution must itself be an observable. As a bond path is a maximum in the electron density distribution, measured along a particular trajectory in space, a bond path is likewise an observable. Later, Bader (1990) concluded that a pair of atoms is bonded only if the pair is connected by a bond path. Given that the bonded radius of an atom is defined as the distance between the nucleus of the atom and the minimum in the electron density measured along a bond path, the bonded radius of an atom is likewise an observable. By mapping the bond paths, not only are the bonded radii of bonded atoms determined but also the polarization of electron density distributions of an atom can be assessed. Further, the number of bond paths that radiate from a given atom uniquely defines the coordination number of the atom.

Table 1 compares crystal radii (r_c) and averaged bonded radii ($<r_b>$), from which it is clear that bonded radii determined on the basis of the electron density distribution differ substantially, on average, from the ionic radii (r_i) of Shannon (1976). **Table 1** also shows that the average bonded radii of O atoms ($<r_b(O)>$) decrease systematically as the shared character of the M-O bonded interactions increases. It also reveals that larger metal atoms display a wider range of bonded radii values than smaller metal atoms.

Bonded Interactions and Bond Paths

The electron density distribution and bond critical points calculated for the cubic garnet pyrope, $^{[8]}Mg_3{}^{[6]}Al_2{}^{[4]}Si_3O_{12}$ (Gibbs and Smith, 1965), show that four non-equivalent bond paths radiate from each O atom, one along the $^{[4]}$Si-O bond path, one along the $^{[6]}$Al-O bond path and two along two nonequivalent $^{[8]}$Mg-O bond paths (Gibbs et al., 2013a). The bonded radius of the O atom is not fixed but ranges from 0.95 Å, measured along the $^{[4]}$Si-O bond path, to 1.12 Å, measured along the $^{[6]}$Al-O bond path, to 1.26 Å and 1.36 Å, measured along the two nonequivalent $^{[8]}$Mg-O bond paths. Clearly, on the basis of the bonded oxygen radii, the electron density of the O atom is highly polarized, with its four bonded radii ranging between 0.95 Å and 1.36 Å. The radius of the Si atom measured along its four equivalent bond paths is single valued with a bonded radius of 0.67 Å. The bonded radius of the Al atom measured along its six equivalent bond paths is also single valued with a larger bonded radius of 0.79 Å. In contrast, the Mg atom has two nonequivalent sets of bond paths, the shorter (0.94 Å) involving the shorter $^{[8]}$Mg-O bonded interaction (2.20 Å) and the longer (0.99 Å) involving the longer $^{[8]}$Mg-O bond (2.35 Å).

The crystal structure of calcite, $^{[6]}Ca^{[3]}CO_3$, (Catti et al., 1993) is a framework structure of corner-sharing CaO_6 octahedra in which each O atom is bonded to two equivalent $^{[6]}$Ca atoms and one $^{[3]}$C atom. The six bonded radii of the Ca atom are each 1.17 Å and the three bonded radii of the C atom are each 0.83 Å, a result that shows the bond critical points of both atoms are distributed spherically about the nuclei of the two atoms. On the other hand, the bonded radius of the O atom measured along the C-O bond path is 0.46 Å, much shorter than those measured along the two equivalent Ca-O bond paths, 1.14 Å (Skinner et al.,1994; Gibbs et al., 2013a), demonstrating that the O atom is likewise highly polarized.

In contrast, the bonded radii of the O atoms in the silica polymorphs quartz, cristobalite, and coesite are single valued with the O atoms showing little evidence of polarization. The bonded

radii of the Si and O atoms, measured along the twelve nonequivalent Si-O bond paths for the three polymorphs are each r_b ($^{[2]}$O) = 0.95 Å and r_b ($^{[4]}$Si) = 0.67 Å, respectively. Four Si-O bond paths radiate from each Si atom to a minimum in the electron density at a distance of 0.67 Å, defining the bonded radii of the Si atoms. Two O-Si bond paths radiate from each O to a minimum in the electron density at a distance of 0.95 Å, defining the bonded radius of the O atom **(Figure 1)** (Gibbs et al., 1999; Gibbs et al., 2013a). For the high-pressure silica polymorph stishovite, each Si atom is bonded to six O atoms and each O atom is bonded to three Si atoms. The bonded radii of Si and O atoms, measured along each Si-O bonded interaction, are r_b ($^{[6]}$Si) = 0.72 Å and r_b ($^{[3]}$O) = 1.06 Å, respectively. Three bond paths radiate from each O atom to a minimum in the electron density at 1.06 Å, the bonded radius of the O atom, and six paths radiate to a minimum in the electron density at 0.72 Å from the Si atom, the bonded radius of the $^{[6]}$Si atom (Gibbs et al., 1992). As expected, the bonded radii of the Si and O atoms in stishovite are 0.05 Å larger than those in quartz, cristobalite, and coesite, given that each Si atom is bonded to six O atoms in stishovite, whereas the Si atoms are bonded to four O atoms in quartz, cristobalite, and coesite (Gibbs et al., 2009). Furthermore, because each Si atom in stishovite is bonded to six equal-sized O atoms and that each Si atom in the other three silica polymorphs is bonded to four equal-sized O atoms, the Si and O atoms are unpolarized.

The bonded radius of the Si atom determined for pyrope and the framework silica polymorphs are virtually the same, whereas the bonded radii of the O atoms display a large range of values. Gibbs et al. (2013a) showed that the bonded radius of the O atom is not fixed but increases as the M-O bond length and the row number of the M atom increase.

DISCUSSION AND ANALYSIS OF PAULING'S RULES

This is the peer-reviewed, final accepted version for American Mineralogist, published by the Mineralogical Society of America.
The published version is subject to change. Cite as Authors (Year) Title. American Mineralogist, in press.
DOI: https://doi.org/10.2138/am-2021-7938. http://www.minsocam.org/

Pauling's First Rule

According to Pauling's first rule, M-O bond lengths are equal to the radius sum of the bonded atoms, and the coordination number of the M atom is determined by the radius ratio of the bonded pair.

The classic test of the radius-ratio rule involves the AB structures and the following structure types: CsCl, NaCl (halite), ZnS (sphalerite), and ZnS (wurtzite). As is apparent from **Figure 2(a)**, the separation of structure types by radius ratio is not very good as 38 of 99 structures fall in the wrong fields. Moreover, different structure types overlap and are not well-separated into unique fields by ionic radii.

Almost 50 years ago, pseudopotential radii (Simons and Bloch, 1973; Zunger and Cohen, 1978; Cohen 1980) were used to try and produce a better sorting of AB structures and were quite effective. The indices $R_\sigma^{AB} = |(r^A_p + r^A_s) - (r^B_p + r^B_s)| = |(r^A_\sigma - r^B_\sigma)$ and $R_\Pi^{AB} = |(r^A_{p\Pi} + r^A_{s\Pi}) - (r^B_{p\Pi} + r^B_{s\Pi})| = |(r^A_\Pi - r^B_\Pi)|$, where r^A_s and r^A_p are the s- and p-orbital radii for an atom A, r^B_s and r^B_p are the s- and p-orbital radii for an atom B, r^A_σ and $r^A_{p\Pi}$ are the sigma and pi bonding radii of an atom A, and r^B_σ and $r^B_{p\Pi}$ are the sigma and pi bonding radii of an atom B, work quite well in this regard. Chelikowsky and Phillips (1977), Zunger (1980), and Bloch and Schatteman (1980) produced a much better sorting of structure types, but no a priori predictions of the location of the field boundaries. Burdett et al. (1981) showed that r^A_σ and r^B_σ have a much-improved structural mapping (Figure 2b), although again they do not accurately predict coordination numbers from Pauling's first rule.

At the time the radius-ratio rule was proposed, it was thought that, in a given valence state and for a given coordination number, the radius of a bonded atom is constant; however, more recent work has shown this not to be the case. Electron density distributions for a relatively large

number of minerals (Gibbs et al., 2001) show that the bonded radius of the oxygen atom is not fixed but increases systematically in parallel trends as the bonded radii of the M atoms increase. George et al. (2020) recently reported in a 'statistical study' of Pauling's (1929) first rule that only 66% of the time did the radius ratio of the metal ions and the O ions agree with Pauling's radius-ratio rule, using univalent radii as recommended by Pauling (1960). Given that the bonded radius of the O atom is not fixed but increases systematically as the bonded radii of the metal atoms increase, significant departures from the radius-ratio rule are not surprising.

Figure 3(a) shows the range in cation-coordination numbers as a function of Lewis acidity of the cation (values from Gagné and Hawthorne, 2017) for all elements in their various valence states for which good crystal-structure data are available (~10,000 inorganic structures) from H^{+} to Cm^{3+}. If Pauling's first rule were adhered to exactly, all data in **Figure 3(a)** should lie within the dashed red lines, i.e., should show only one or two coordination numbers for a given anion, e.g., O^{2-}. Pauling's first rule involves radius ratios for [4]-, [6]-, [7]-, [8]-, [9], and [12]-coordination (Pauling, 1960, page 545). **Figure 3(b)** shows the mean observed coordination number for all ions, and the broken lines show which ions fall within this range (i.e., most of them). It is apparent that most ions show a much wider range of coordination numbers than predicted by Pauling's first rule, particularly those ions of lower Lewis acidity.

Brown (1988) examined the factors determining cation-coordination numbers using primarily the valence-matching principle from BVT (Brown, 2002a, 2016), which states that stable structures will form when the Lewis acidity of the cation closely matches the Lewis basicity of the anion. As an example, consider schiavinatoite (ideally $Nb(BO_4)$) (Demartin et al., 2001), and behierite, ideally $Ta(BO_4)$ (Mrose and Rose, 1962). The Lewis basicity of the $(BO_4)^{5-}$ oxyanion is 0.42 v.u., the Lewis acidities of Nb^{5+} and Ta^{5+} are 0.835 and 0.822 v.u. (Gagné and Hawthorne,

2017), and the mean observed coordination numbers) for Nb^{5+} and Ta^{5+} are 5.99(2) and 6.09(2) for 250 and 152 polyhedra (Gagné and Hawthorne, 2020), respectively. The Lewis acidities of Nb^{5+} and Ta^{5+} do not match the Lewis basicity of the $(BO_4)^{5-}$ oxyanion, and the criterion for a stable structure is not met for [6]-coordinated Nb^{5+} and Ta^{5+}. This forces Nb^{5+} and Ta^{5+} into higher coordination numbers; schiavinatoite and behierite adopt the zircon structure with Nb^{5+} and Ta^{5+} in [8]-coordination and effective Lewis acidities of 5 / 8 = 0.63 v.u.. The match is now significantly closer: 0.42 vs. 0.63 v.u., and a structure is possible, although highly strained (Hawthorne, 2018).

Brown (1988) also concluded that in order to predict both coordination numbers and interatomic distances in oxide-oxysalt structures, it is necessary to use a variable radius for O^{2-}, expressed as $rO^{2-} = 1.12 + 0.23 \ln(N - 2)$ Å where N is the cation-coordination number involved. This result parallels that of Gibbs et al. (2013a) who showed that the radius of O^{2-} in particular is quite variable as a function of its local environment (including interatomic distances).

Based on the electron density distributions and bond paths determined for silicates and oxides by Gibbs and co-workers, Pauling's first rule might be modified to read 'A coordination polyhedron of oxygen atoms is formed about each metal atom M, the M-O distance being given by the sum of the bonded radii of the M and O atoms and the coordination numbers of the atoms being determined by the number of bond paths that radiate from the atoms' (Gibbs et al., 2001; 2013a). However, an alternative modification of Pauling's first rule is offered here: 'A coordination polyhedron of oxygen atoms is formed about each metal atom M, the M-O distance and the bonded radii of the M and O atoms being determined by the characteristic forces between the two atoms forming the bond and the coordination numbers of the atoms being determined by the number of bond paths that radiate from the atoms'. As pointed out by Bader (2009), the characteristic forces associated with a bond path are the Feynman force exerted on nuclei

(Feynman, 1939) and the Ehrenfest force exerted on the electrons of the bonded atoms (Pendás and Hernández-Trujillo, 2012).

These suggested modifications of Pauling's first rule do not allow a simple back-of-the-envelope prediction of bond lengths because the interatomic forces characteristic of the atoms in a chemical bond must be calculated for each bond using a quantum mechanical model such as density functional theory to optimize molecular geometries (bond lengths and angles), followed by determining the minimum in electron density, the bond-critical point, along the bond path (Gibbs et al., 2003).

Pauling's Second Rule

As observed in the Introduction, few definitions have had more impact as a basis for understanding bond-length variations and bonded interactions in minerals than Pauling's (1929) definition of bond strength, $s = \nu/\kappa$, of a M-O bonded interaction. One of the beauties of this simple yet powerful definition is that the sum of the bond strengths involved in a bonded interaction often closely matches the magnitude of the valence of the anion that is bonded to the M cation. Pauling's second rule was formulated in part from a comprehensive knowledge of the crystal structures of minerals and other materials known prior to 1929, from Born's elegant work on lattice energy, and likely from Pauling's (1960) knowledge of resonance theory for the bonded interactions in molecules and his belief that the rule holds equally well for crystals. It is important to realize that the rule was considered to be neither rigorous nor global in its application, but as pointed out later by Pauling (1960), it has been successfully used to verify the structures of a number of minerals, as will be discussed in the Applications section. Further, as observed by Sir Lawrence Bragg (1937), the rule favors a system of low potential energy and, accordingly, high stability. He added that although the rule is simple, it imposes rigorous constraints on the topology of the bonded

interactions in a crystal. Indeed, as pointed out by George et al. (2020), the rule accounts for the Si-O bonded interactions of quartz, where the sum of the bond strengths of the bonded interactions match the valence of the O atom in the structure exactly.

With the discovery that the Si-O bond lengths and Si-O-Si angle of the H_6Si_2O molecule are virtually the same as those in quartz (Gibbs, 1982), Gibbs et al. (1987) did molecular orbital geometry optimization calculations for the structures of a number of simple oxyhydride molecules containing first- and second-row metal atoms. The bond lengths, $R(M\text{-}O)^{Mol}$, generated in the calculations scatter along two well-defined parallel power-law trends when plotted against the Pauling bond strength, *s*, of the M-O bonded interactions (**Figure 4(a**)) and scatter along a single trend when plotted against *s*/r, where r is the row number of the atoms in the periodic table. Regression analysis of the molecular data set resulted in the power-law expression $R(M\text{-}O)^{Mol} = 1.39(s/r)^{-0.22}$ (**Figure 4(b**)) with more than 95 percent of the variation of R(M-O) dependent on *s*/r.

To determine the extent to which the bond lengths, $R(M\text{-}O)^{Mol} = 1.39(s/r)^{-0.22}$, observed for molecules, match the bond lengths in crystals calculated using the sum of the ionic radii, $R(M\text{-}O)^{Shan} = r_c(M) + 1.24$ Å, $R(M\text{-}O)^{Mol}$ was plotted in terms of $R(M\text{-}O)^{Shan}$ (**Figure 5**), where $r_c(M)$ are the Shannon crystal radii of the atoms M and 1.24 Å is the assumed radius of the bonded O atom (Gibbs et al., 2015). The agreement between the Shannon bond lengths and the bond lengths generated with the molecular power law-based expression indicates that the bonded interactions observed for molecules are comparable with those observed for crystals, as argued earlier by Gibbs et al. (1987). This agreement suggests that the bond lengths in oxide crystals are governed in large part by short-ranged molecular forces (Gibbs, 1982; Gibbs *et al*., 1987). Despite the relative simplicity of the $R(M\text{-}O)^{Mol}$ expression, it reproduces 40% of the Shannon bond lengths to within 0.05 Å, 75% to within 0.10 Å, 85% to within 0.15 Å, and 95% to within 0.20 Å. (Gibbs *et al*.,

2015). The success of the molecular-based expression in matching the bond lengths in crystals is ascribed to a one-to-one connection between the electron density accumulated between the bonded atoms and the Pauling bond strength of the bonded interactions.

In a theoretical study of several perovskite crystals, geometry optimized with quantum mechanical density functional methods at pressures as high as 80 GPa, Gibbs et al. (2012) (see also Gibbs et al., 2013b) found that the value of the electron density, $\rho(r_c)$, determined at the bond critical points, r_c, of the bonded interactions, scatter along four roughly parallel power-law trends when plotted against the geometry-optimized, second-row Al-O bond lengths, the third-row Ca-O and Sn-O bond lengths, the fourth-row Y-O bond lengths, and the fifth-row La-O bond lengths (**Figure 6(a)**), generated as a function of pressure. When the bond lengths were plotted against $\rho(r_c)/r$, where $\rho(r_c)$ is the value of the electron density determined at the bond critical point of the bonded interaction, the trends match those between R(M-O) and *s*/r for the molecules almost exactly (**Figure 6(b)**), demonstrating that the Pauling bond strength of a M-O bonded interaction is in 'exact' agreement with the accumulation of the electron density at the bond critical points of the bonded interactions.

In another study of Pauling's rules based on the experimental and calculated electron density distributions determined for M-O bonded interactions, Gibbs et al. (2014) showed that the results accord with Pauling's first two rules. Recasting the expressions $R(M\text{-}O) = 1.39(s/r)^{-0.22}$ and $R(M\text{-}O) = 1.41(\rho(r_c)/r)^{-0.21}$ in terms of *s* and $\rho(r_c)$, respectively, the expressions $s = r(1.39/R(M\text{-}O)^{4.54}$ and $\rho(r_c) = (1.41/([R(M\text{-}O)])^{4.76}$ show that *s* and $\rho(r_c)$ agree to within ~5% (**Figure 7**). The close agreement between the bond strength of a bonded interaction and $\rho(r_c)$ is a testament to Pauling's genius in choosing a simple yet powerful parameter, *s*, as a measure of the strength of a bonded interaction for the second rule. Pauling's first rule was modified above to satisfy the radius-

ratio constraints and coordination number of a bonded atom in terms of the bond paths and the bonded radii of the bonded atoms.

In the recent statistical study of Pauling's second rule, stressing the limits and range of the rule in terms of the chemistry and structures for about 5000 oxides, George et al. (2020) concluded that 'The rule was found to be 'nearly exactly fulfilled for roughly 20% of all oxygen atoms, indicating a much lower predictive power than expected'.

Comparison of Theory and Experiment

As discussed in several previous sections on Pauling's first and second rules, Density Functional Theory (CRYSTAL98 and TOPOND) and full potential linearized augmented plane wave theory (FLAPW and WIEN2k) were used by Gibbs and co-workers to calculate electron density distributions along bond paths of various crystalline materials (e.g., $YAlO_3$ and silicate minerals, including the silica polymorphs). The electron density distributions obtained using these different theoretical methods are in very close agreement. Moreover, Gibbs et al. (2007; 2009) showed that the predicted electron density distributions of these and other crystals (e.g., Fe- and Cu-sulfides) and siloxane molecules match those obtained with high-resolution single-crystal synchrotron X-ray diffraction (Kirfel et al., 2005). This body of work shows that DFT predictions of electron density distributions are consistent with experiment and with the predictions of Pauling's second rule in many cases.

Pauling's Third, Fourth, and Fifth Rules

Pauling's third rule is related to the presence of shared edges and shared faces of polyhedra in a crystal structure and their impact on the structure and stability of a crystal. Pauling observed that the edges shared in common between polyhedra are uniformly shorter than the unshared ones,

a feature he ascribed to reduction of the M-M repulsion between the metal atoms in adjacent edge- or face-sharing polyhedra. George et al. (2020) tested the rule by identifying all connected pairs of polyhedra and computing the fraction of the connected pairs that are corner- (63%), edge- (27%), or face-sharing (10%), concluding that 'This agrees well with Pauling's rule'.

An important departure from the third rule occurs in the α-Al_2O_3 structure type, which includes corundum, a mineral that forms in high pressure metamorphic rocks, and hematite (α-Fe_2O_3) and ilmenite ($FeTiO_3$), both of which form in low-temperature--low-pressure environments. Pauling and Hendricks (1925) solved the structures of corundum and hematite and found them to consist of somewhat distorted hexagonal close-packing of oxygens in which 2/3 of the octahedral interstices are occupied by M cations. These three minerals and others with this structure type consist of chains of face-sharing octahedra, which results in increased M^{3+}-M^{3+} repulsion.

The olivine structure-type ($^{[6]}M_2{}^{[4]}SiO_4$) provides an instructive example of Pauling's third rule and is commonly described as a somewhat distorted hexagonal close-packed array of oxygen anions in which one-eighth of the tetrahedral and one-half of the octahedral interstices are occupied by Si^{4+} and divalent M cations (most commonly Mg^{2+} and Fe^{2+}), respectively. **Figure 8(a)** shows the idealized HCP olivine structure. Cation-containing polyhedra in minerals and other crystalline solids are often distorted and thus can have a range of M-O bond lengths (**Table 2**).

The $M(1)O_6$ octahedron shares six of its twelve edges with other polyhedra (two with other $M(1)O_6$ octahedra, two with $M(2)O_6$ octahedra, and two with SiO_4 tetrahedra), whereas the $M(2)O_6$ octahedron shares only three edges (two with $M(l)O_6$ octahedra and one with a SiO_4 tetrahedron). Pauling's third rule predicts that the shared polyhedron edges in olivine will be shorter than unshared edges such that cation-cation distances across shared edges are maximized and

cation-cation repulsive forces are minimized. This rule is indeed obeyed in the actual olivine structure, which is shown in **Figure 8(b)**. The resulting polyhedron distortions are significant. The point group or site symmetries (given in Schoenflies notation with Hermann-Mauguin notation in parentheses) of the M(l)O_6 and M(2)O_6 octahedra are reduced from Oh (or 4/m 3-bar 2/m) in the ideal HCP structure to Ci (or 1-bar) and Cs (or m), respectively, in the actual structure, and that of the SiO_4 tetrahedron is reduced from Td (or 4-bar 3 m) in the HCP structure to Cs (or m) in the actual structure. However, for the purpose of spectral analysis, the point symmetries of the M(l)O_6 and M(2)O_6 octahedra in olivine are generally regarded as approximately D4h (or 4/mmm) and C3v (or 3m), respectively. The cause of these distortions has conventionally been attributed to cation-cation repulsions across shared edges following Pauling's third rule.

Comparison of the shared and unshared O-O edge lengths for MO_6 octahedra in forsterite **(Table 2)** shows that the shared O-O edges are indeed significantly shorter than the unshared edge lengths ($\Delta_{u\text{-}s}$ = 0.315 Å for M(1)O_6 octahedra and $\Delta_{u\text{-}s}$ = 0.225 Å for M(2)O_6 octahedra). Comparison of the shared and unshared O-O edge lengths for SiO_4-MO_6 edge sharing shows that the shared edge lengths are significantly shorter than the unshared O-O tetrahedron edges ($\Delta_{u\text{-}s}$ = 0.188 Å). In addition, comparison of the $M(1)_B$-$M(1)_B$ distance (2.977 Å) across the shared O(1)-O(2) edge and the $M(1)_B$-$M(2)_B$ distance (3.210 Å) across the O(1)-O(3) shared edge for forsterite are significantly longer than these distances for the ideal HCP olivine structure ($\Delta_{M(1)–M(1)}$ = 0.237 Å and $\Delta_{M(1)–M(2)}$ = 0.449 Å). The shorter O-O shared edge lengths and the longer M-M distances of the actual forsterite structure vs. the ideal HCP olivine structure are consistent with Pauling's idea that shared edges shorten and M-M distances lengthen across shared O-O edges in order to reduce M-M repulsion.

Another way of visualizing the effect of metal-metal repulsive forces in forsterite on bond angles and interatomic distances is to extract the structural cube of forsterite shown in **Figure 9(a)** and create planar projections of the unique M-O-M-O and M-O-Si-O faces of the distorted cube of nearest-neighbor cations and anions (**Figure 9(b)**), which show bond-angle strains and interatomic distances (**Figure 10**). The various interatomic distances shown in the planar projection of **Figure 10** were discussed in the previous paragraph. The bond-angle strains shown in **Figure 10** are consistent with the cation-cation repulsive interactions in forsterite.

The largest bond-angle strains are observed for the following angles (**Figure 10-right**): O(3)-$M(2)_B$-O(3) (-18.6°), O(3)-$M(1)_B$-O(2) (-15.3°), Si_B-O(3)-$M(1)_B$ (+19.1), Si_B-O(3)-$M(2)_B$ (+17.7°), and Si_B-O(2)-$M(1)_B$ (+17.3°), which reflects the greater repulsive forces between Si^{4+} and M^{2+} cations. As expected, the bond-angle strains shown in **Figure 10-left** are much smaller, ranging from +2.5° to -9.1°, and reflect the smaller repulsive forces between M^{2+} cations.

Pauling's fourth rule notes that in a crystal structure containing several cations, those of high valency and small coordination number tend not to share polyhedron elements. The olivine structure discussed above is a departure from this rule because SiO_4^{4-} tetrahedra share edges with both $M(1)O_6$ and $M(2)O_6$ octahedra that contain Mg^{2+} and Fe^{2+}. Although α-Al_2O_3 (corundum) and α-Fe_2O_3 (hematite) have only one type of cation, Al^{3+} and Fe^{3+} occupy octahedra that share faces and are highly distorted to minimize cation-cation repulsive forces (see Pauling and Hendricks, 1925). In their statistical analysis of Pauling's rules George et al. (2020) found that 40% of the tested structures departed from Pauling's fourth rule.

Pauling's fifth rule states that the number of different kinds of constituents in a crystal tends to be small (Rule of Parsimony). Quartz (α-$^{[4]}SiO_2$), with only one distinct tetrahedral site, and garnet [$^{[8]}X_3{}^{[6]}Y_2{}^{[4]}Si_3O_{12}$], which has one type of tetrahedron, one type of octahedron, and one

type of distorted dodecahedron (Novak and Gibbs, 1971), are examples of minerals with a small number of constituents or distinct cation sites. Amphibole-supergroup minerals $[^{[10-12]}A_{0-1}{}^{[8]}X_2{}^{[6]}Z_5{}^{([4]}((Si,Al,Ti)_8O_{22})(OH,F,Cl,O)_2]$, where A = □, Na, K, Ca, Pb^{2+}; X = Li, Na, Mg, Fe^{2+}, Mn^{2+}, Ca; Z = Li, Na, Mg, Fe^{2+}, Mn^{2+}, Zn, Co, Ni, Al, Fe^{3+}, Cr^{3+}, Mn^{3+}, V^{3+}, Ti, Zr (Hawthorne et al., 2012) are structurally more complex than garnet and can incorporate an extremely wide variety of different ions. An example of a mineral structure with a large number of distinct sites is manitobaite $(Na_{16}□)Mn^{2+}{}_{25}Al_8(PO_4)_{30}$, which has 80 distinct cation sites and 120 distinct anion sites (Tait et al., 2011). This structure clearly departs significantly from Pauling's Rule of Parsimony. George et al. (2020) also pointed out major departures from Pauling's fifth rule, particularly for alkali and alkaline-earth metals, which are accommodated in a wide range of local coordination environments, and a few main-group elements, including B, Ga, and Ge. Overall, George et al. (2020) found that only 13% of the tested structures satisfy the second to fifth rules, simultaneously.

BOND-VALENCE THEORY

Pauling's second rule defined bond strength as cation charge divided by cation coordination number and noted that the bond strength incident at an anion is approximately equal to the anion valence (with the sign reversed). Pauling's definition of bond strength implicitly assumes that all bonds within a given coordination polyhedron have the same bond strength. Zachariasen (1954) showed that bond strength varies with bond length, as shown in **Figure 11** for some uranyl compounds. Baur (1981) also pointed out that there is a strong correlation between bond length and Pauling bond strength.

What is now known as Bond-Valence Theory (BVT) gradually developed from this realization that the strength of a bond, now referred to as its bond valence in v.u. (valence units),

This is the peer-reviewed, final accepted version for American Mineralogist, published by the Mineralogical Society of America.
The published version is subject to change. Cite as Authors (Year) Title. American Mineralogist, in press.
DOI: https://doi.org/10.2138/am-2021-7938. http://www.minsocam.org/

correlates very strongly with its bond length. Brown and Shannon (1973) proposed a model in which a structure consists of atom cores held together by valence electrons associated with the chemical bonds between the atoms. They state explicitly that the valence electrons may be associated with chemical bonds in a symmetric (covalent) or asymmetric (ionic) manner. Thus a priori knowledge of the electron distribution is not required to use this approach. In addition, they proposed algebraic forms for the relation between bond valence and bond length and provided parameters for 25 cation-O^{2-} pairs derived from 417 crystal structures. Burdett and Hawthorne (1993) showed that the form of the bond-valence curves may be derived algebraically from a molecular-orbital description of a solid in which there is a significant energy gap between the interacting orbitals on adjacent atoms, whereas Preiser et al. (1999) gave an ionic justification of the bond-valence model. Thus, one may conclude that the bond-valence model is not a theory of "ionic" bonds or "covalent" bonds. It is a simple yet quantitative method that allows us to examine and analyze the stereochemistry and physical properties of inorganic solids. It is used primarily for crystals, but also can be used for oxide surfaces (Hiemstra et al., 1996; Bargar et al., 1997a; 1997b; 1997c; Schindler et al. 2004a, 2004b; Bickmore et al. 2004, 2006; Hawthorne & Schindler, 2014); poorly crystalline materials (e.g., ferrihydrite; Gilbert et al., 2013); silicate glasses (Farges et al., 1991, 1992); and silicate liquids (Brown et al., 1995; Farges and Brown, 1996; Farges et al., 1996).

Examples of applications of BVT in these different areas will be discussed in the Applications section. Although the idea of bond valence grew out of Pauling's second rule, the wide variety of its applications and subsequent examination of its theoretical underpinnings show that it is a theory of atomic arrangements in its own right, without any reference to specific models of the chemical bond. Its power lies in the fact that (1) it is a back-of-the-envelope method in which

the physical details are not obscured by complexities of computation, (2) it can be used for disordered crystal structures, such as solid solutions, and (3) it may be used to constrain the behavior of dynamic systems involving diffusion and adsorption, all of which are extremely common in minerals and other Earth materials.

Bond-Valence Curves

For any pair of bonded atoms, bond valence is inversely proportional to the length of the bond: large bond valences are associated with short bonds, and small bond valences are associated with long bonds. To obtain numerical values for the bond valences, each bond is assigned a bond valence such that the valence-sum rule is satisfied (Brown, 2002a): The sum of the bond valences at each atom is equal to the magnitude of the atomic valence. Thus, bond valences are scaled to the formal valences of the cations and anions involved in the chemical bonds. If this is done for a relatively large number of structures, one may derive numerical parameters, bond-valence parameters (or bond-valence curves) that may be used to calculate bond valences from bond lengths. Using a dataset of 180,194 bond lengths from 31,489 coordination polyhedra in 9,367 (filtered) crystal-structures, Gagné and Hawthorne (2015) tested 19 two-parameter and 7 three-parameter equations, showed that the expression of Brown and Altermatt (1985) is optimum, and calculated bond-valence parameters for 135 cations bonded to O^{2-}.

The Basic Axioms of Bond-Valence Theory

BVT has three principal axioms: (1) the valence-sum rule; (2) the path (loop) rule; and (3) the valence-matching principle, which are discussed below.

The valence-sum rule. The sum of the bond valences at each ion is equal to the magnitude of the atomic valence. For any field, Gauss's flux theorem relates the distribution of electric charge

This is the peer-reviewed, final accepted version for American Mineralogist, published by the Mineralogical Society of America.
The published version is subject to change. Cite as Authors (Year) Title. American Mineralogist, in press.
DOI: https://doi.org/10.2138/am-2021-7938. http://www.minsocam.org/

to the resulting electric field: the flux of the field intensity through a closed surface is related to the total net charge enclosed within that surface. The valence-sum rule is thus a corollary of Gauss's flux theorem applied to the electrostatic potential field. Preiser et al. (1999) show that the fluxes linking atoms correlate strongly with the bond valences assigned by the bond-valence method. Topological properties of the various fields associated with an array of atoms are discussed by Brown (2002b). Long-range Coulombic interactions are inductively transmitted through a crystal by the operation of Gauss's theorem on the Coulomb field at each atom in the crystal (Preiser et al., 1999). This was the first axiom to be developed and had its origins in Pauling's second (bond strength) rule.

The path rule. The sum of the directed bond-valences along any path between crystallographically equivalent ions is equal to zero (Gagné et al., 2017). This definition includes closed paths (≡ loops) as this was originally formulated just for loops (Brown, 1980). As bond valences are equal to bond fluxes, this rule is dictated by the conservation of electric charge via Maxwell's third equation.

The valence-matching principle. The Lewis-acid strength of a cation may be defined as its characteristic (bond) valence, which is equal to its atomic (formal) valence/mean coordination-number (Brown 1980, 2002a, 2016); comprehensive values (based on ~10,000 crystal structures) are given by Gagné and Hawthorne (2017). The Lewis-base strength of an anion can be defined as the characteristic valence of the bonds formed by the anion. If two ions form a bond, the magnitude of the strength of the bond from the cation to the anion is controlled by the Lewis-acid strength of that cation, and the magnitude of the strength of the bond from the anion to the cation is controlled by the Lewis-base strength of that anion. However, the bond from the cation to the anion is the same bond as that from the anion to the cation, and hence the magnitudes of the Lewis acid strength

and the Lewis base strengths of the constituent ions must be approximately the same for that bond to form. In other words, as a chemical bond involves both a cation and an anion, the electron-attracting capacity of the cation must match the electron-donating capacity of the anion for a chemical bond to form. This argument is based on the handshaking principle of Graph Theory (e.g., Wilson, 1979), and leads to a particular criterion for chemical bonding, the valence-matching principle (Brown 2002a, 2016): Stable structures will form where the Lewis-acid strength of the cation closely matches the Lewis-base strength of the anion. The valence-matching principle is the most important and powerful idea in BVT (Hawthorne 2012, 2015); it allows us not just to interpret known structures or compounds. We can test the stability of possible compounds (in terms of whether they can or cannot exist), which moves us from a posteriori to a priori analysis. Below, we discuss modern applications of BVT in crystal chemistry, mineralogy, and geochemistry.

A Priori Bond-Valence Calculations

The bond-valence model has two important theorems (see above): [1] the valence-sum rule, which states that the sum of the bond valences at each atom is equal to the magnitude of the atomic valence, and [2] the path rule which states that, in a structure, the sum of the directed bond-valences along any path of bonds beginning and ending on symmetrically equivalent ions is zero. Equations describing the valence-sum rule and the path rule may be written in terms of the constituent bond valences. These are collectively called network equations (Brown, 2016) and can be solved to calculate a priori bond-valences for a crystal structure (e.g., Gagné et al., 2017). A priori bond valences depend only on the formal valence of the ion at each site in the structure, and the bond-topological characteristics of the structure (i.e., the ion connectivity), and represent bond valences arising solely from the topological characteristics of the structure without any contribution from

effects due to the specific electronic characteristics of the constituent ions or to strain arising from mapping bond valences into bond lengths in three-dimensional Cartesian space. Bond-valence curves may be used to calculate the corresponding a priori bond-lengths, and topological strain can be evaluated by Distance-Least-Squares refinement of the resulting structure.

In some cases (e.g., spinel-supergroup minerals, garnet-supergroup minerals), the valence-sum equations are sufficient for solution. However, this is not usual, and for most structures, a combination of valence-sum and path equations is necessary for solution. Consider the structure of divalent-cation clinopyroxenes of the form $M(2)M(1)Si_2O_6$, e.g., diopside, $CaMgSi_2O_6$, and hedenbergite, $CaFe^{2+}Si_2O_6$, both of which are monoclinic, space group C2/c (Clark et al., 1969; Cameron et al., 1973). The generalized bond-valence table of the relevant charge-arrangement is shown as **Table 3**.

M(2) is [8]-coordinated with four crystallographically distinct M(2)-O distances, M(1) is [6]-coordinated with three crystallographically distinct M(1)-O distances, and Si is [4]-coordinated with four crystallographically distinct Si-O distances. There are two pairs of M(2)-O bonds (to O3) that are crystallographically distinct but topologically identical and hence there are only three distinct M(2)-O bond-valences (labelled a, b and c in **Table 3**). There are two Si-O bonds (to O3) and two pairs of M(1)-O bonds (to O1) that are similarly merged in the bond-valence table which thus has eight distinct bond-valences: a through h. The valence-sum rule for the cations gives the following equations:

$$2a + 2b + 4c = {}^{M(2)}V = 2 \quad [1]$$

$$4d + 2e = {}^{M(1)}V = 2 \quad [2]$$

$$f + g + 2h = {}^{Si}V = 4 \quad [3]$$

The valence-sum rule for the anions gives the following equations:

$$a + 2d + f = 2 \quad [4]$$

This is the peer-reviewed, final accepted version for American Mineralogist, published by the Mineralogical Society of America.
The published version is subject to change. Cite as Authors (Year) Title. American Mineralogist, in press.
DOI: https://doi.org/10.2138/am-2021-7938. http://www.minsocam.org/

$$b + e + g = 2 \quad [5]$$

$$2c + 2h = 2 \quad [6]$$

As these six equations are constrained by electroneutrality, there are five linearly independent valence-sum equations, and **eq. 6** was omitted from consideration. There are eight independent variables and hence the system is underdetermined considering just the valence-sum equations. Thus, we must use the path rule, the equations for which may be written in general form as $\sum s_{ij} = 0$ where the summation is over a path that starts and finishes on symmetrically equivalent vertices in the directed graph of the bond network of the structure. This rule introduces the idea of directed bond-valences, whereby bonds from a cation to an anion are considered positive and bonds from an anion to a cation are considered negative in sign. There are five linearly independent valence-sum equations and thus we need three linearly independent path equations to solve for the eight a priori bond-valences of divalent-cation clinopyroxene. Paths may be read off the bond-valence table (**Table 3**):

M(2) → O1 → M(1) → O2 → M(2), resulting in the following equation:

$$a - d + e - b = 0 \quad [7]$$

M(2) → O1 → Si → O2 → M(1) → O1 → Si → O3 → M(2), resulting in the following equation:

$$a - f + g - e + d - f + h - c = 0 \quad [8]$$

M(2) → O2 → Si → O3 → M(2), resulting in the following equation:

$$b - g + h - c = 0 \quad [9]$$

These equations (**Table 4**) may be written in matrix form as **Ax** = **b**, where **A** contains the coefficients of the network equations, **x** contains the a priori bond-valences (unknown) and **b**

contains the formal charges of the ions at the sites, together with the zeros associated with the path equations. These equations may be solved for a-h in the usual way; the resulting a priori bond-valences are given in **Table 5**, together with the corresponding a priori bond-lengths for diopside and hedenbergite, calculated with the bond-valence parameters of Gagné and Hawthorne (2015).

Comparison of the a priori and observed bond lengths (**Table 5**) shows reasonable accord between the two sets of data. The a priori bond lengths are not expected to agree with the observed values as the former are affected solely by the distribution of formal charges over the sites in the structure and the bond topology, whereas the latter will be affected by additional electronic effects such as coupled electronic-vibrational degeneracy (Gagné et al., 2017). Gagné and Hawthorne (2020) introduced two distortion indices, Δ_{topol} and Δ_{cryst}, that allow determination of the primary cause(s) of bond-length variation for individual coordination polyhedra and ion configurations, and quantify the distorting power of cations via electronic effects by subtracting the bond-topological contribution to bond-length variation.

Bond-Valence Mapping

An advantage of BVT is that one can look at dynamic processes such as adsorption, dissolution, and diffusion. For diffusion in particular, one may place an ion at a series of positions on a grid throughout a crystal and, using the bond-valence parameters for that specific ion and the ions to which it can bond, calculate the incident bond-valence sums at that ion throughout the crystal, and produce a contoured map of the net incident bond-valence for that anion at all positions in the crystal. One may use the resulting map either to (1) locate an ion in the crystal (e.g., Waltersson, 1978), or (2) examine possible diffusion paths for that ion through the crystal (e.g., Schindler et al., 2006a).

This is the peer-reviewed, final accepted version for American Mineralogist, published by the Mineralogical Society of America.
The published version is subject to change. Cite as Authors (Year) Title. American Mineralogist, in press.
DOI: https://doi.org/10.2138/am-2021-7938. http://www.minsocam.org/

Several vanadium oxides of the general form $(Li,Na)_x(V_3O_8)$ have potential as insertion electrodes for rechargeable Li batteries (e.g., Kumagai et al., 1997). These compounds consist of VO_5 and VO_6 polyhedra that share edges and vertices to form chains that are arranged in layers parallel to (101) (**Figure 12**). These structures can accommodate up to three additional Li^+ ions per formula unit without disrupting the vanadate layer, and this reversible intercalation-removal process is charge-balanced by reduction-oxidation of V^{5+}–V^{4+} in the vanadate layer (e.g., de Picciotto et al., 1993). The $M_{1+x}[V_3O_8]$ phases have also been tested as positive electrodes for Na and Mg (Novak et al., 1995) batteries. Kumagai et al. (1997) examined the Li_{1-x} $Na[V_3O_8]$ solid solution as a positive material for secondary Li batteries. Here, $Li_{0.7}Na_{0.3}[V_3O_8]$ showed the best electrochemical performance among several $Li_{1-x}Na[V_3O_8]$ compounds, which was attributed to a higher chemical diffusion coefficient of the interstitial cations between the vanadate sheets in this compound.

Schindler et al. (2006a) refined the crystal structures of $Li_{1.2}[V_3O_8]$, $Na_{1.2}[V_3O_8]$ and $Na_{0.7}Li_{0.7}[V_3O_8]$. They showed that in $Li_{1.2}[V_3O_8]$, Li fills the M(1) site, the remaining Li occupies the M(2) site, and the M(3) is vacant; in $Na_{1.2}[V_3O_8]$, Na fills the M(1) site and the remaining Na is equally distributed between the M(2) and M(3) sites; in $Na_{0.7}Li_{0.7}[V_3O_8]$, all Na occupies the M(1) site and Li is is distributed in decreasing amounts over the M(1), M(2) site and M(3) sites. **Figure 12** shows the M sites arranged between the layers of vanadate chains in $Na_{0.7}Li_{0.7}[V_3O_8]$. **Figure 13** shows bond-valence maps for Li in $Na_{0.7}Li_{0.7}[V_3O_8]$ in the ac-plane at y = 0.25 (a) calculated with the bond-valence parameter for V^{5+} and containing 15 contour levels at an interval of 0.30 v.u., and (**Figure 13(b)**) calculated without any information on V^{5+} and containing 15 contour levels at an interval of 0.35 v.u.

This is the peer-reviewed, final accepted version for American Mineralogist, published by the Mineralogical Society of America.
The published version is subject to change. Cite as Authors (Year) Title. American Mineralogist, in press.
DOI: https://doi.org/10.2138/am-2021-7938. http://www.minsocam.org/

Where the calculation involves V^{5+} (**Figure 13(a)**), there is a lot of detail within the vanadate chains, but this is not relevant to the diffusion of alkali-metal cations as the calculated bond valences are too large to allow alkali metals to occur there. Where the calculation omits consideration of V^{5+} (**Figure 13(b)**), there is no detail about the vanadate chains but the detail in the channels between the chains is more apparent. The alkali-metal sites lie within these channels, and contouring of the bond valence within these channels shows that all along the central axis of the channel, the bond valence for Li^+ is fairly close to ideal (1 v.u.) and Li^+ can move freely without major deviations from its bond-valence requirements. At the M(1) site, the sum for Na^+ is 1.3 v.u. and the sum for Li^+ is 0.5 v.u., and at the M(2) and M(3) sites, the sums for Li^+ are 0.70 v.u. and 1.2 v.u., respectively, in accord with the observed site-occupancies. Thus Li^+ may more easily diffuse along an individual channel. However, in order to move through the crystal, the diffusing ion must be able to move from one channel to another. The cross-section of the bond-balance sum at these connections between channels are shown in **Figure 13(c)**. For Li^+, the minimum bond-valence sum in the center of this connection is 1.4 v.u., whereas the minimum for the corresponding sum for Na^+ is 3.5 v.u.. Thus Li^+ may move from one channel to another whereas Na^+ is trapped in a single channel.

Figure 14(a) shows a bond-valence map for $Li[V_3O_8]$. Again, this map shows the prominent channels along which there are diffusion paths for Li^+ between the vanadate chains. The cross sections for Li^+ and Na^+ across the connections between the channels (**Figure 14(b)**) show that the barriers to diffusion between channels are somewhat larger (Li^+: 1.8 v.u.; Na^+: 4.3 v.u.) than is the case in $Na_{0.7}Li_{0.7}[V_3O_8]$ (Li^+: 1.3 v.u.; Na^+: 3.4 v.u.; **Figure 14(c)**, suggesting that diffusion should be easier in $Na_{0.7}Li_{0.7}[V_3O_8]$. This finding suggests that electrochemical performance in these (and other) compounds could be optimized from the viewpoint of chemical

composition by systematic bond-valence mapping for the range of possible chemical compositions.

SELECTED APPLICATIONS OF BOND-VALENCE THEORY TO EARTH MATERIALS

Use of Bond-Valence Theory to Locate H^+ Ions in Crystal Structures

Perhaps the most common use of BVT, apart from checking the probable correctness of a structure, is the location of H^+ ions, usually as constituents of $(OH)^-$ and/or (H_2O) groups. The first example of this was by Warren (1929) in his solution of the crystal structure of tremolite, ideally $Ca_2Mg_5Si_8O_{22}(OH)_2$. Prior to this work, the role of hydrogen in the very common and widely distributed amphibole-supergroup minerals was uncertain: was it there as $(OH)^-$, (H_2O), or as an analytical contaminant? The crystal structure of tremolite showed that the O(3) oxygen ion is coordinated by three [6]-coordinated Mg^{2+} ions for an incident bond strength of 0.333 x 3 = 1 v.u.. To accord with Pauling's second rule, the O^{2-} ion at the O(3) site must also bond to a H^+ ion, forming an $(OH)^-$ group. This was a very nontrivial result as it brought order and understanding to the numerous chemical analyses of amphiboles up to that time (Kunitz, 1930).

The positional parameters for H derived from X-ray data show significant systematic error. The electron density notionally associated with the H atom is partly delocalized into the O-H bond, leading to O-H distances that are shorter than the corresponding internuclear O-H distances and experimental H…O (hydrogen-bond) distances that are systematically longer than the H…O internuclear distances. One can obtain much better results during the refinement process by restraining the O_{donor}-H distance to be very close to an ideal distance, usually in the range 0.96-0.98 Å. Better O-H and H…O distances may be obtained using neutron diffraction, but this is not

practical for many materials for which the crystals are very small. To avoid possible bias present in X-ray data, Gagné and Hawthorne (2018) used only neutron data to derive bond-valence parameters for the H^{+}-O^{2-} bond.

Bond-Valence Analysis of Water in Nominally Anhydrous Mantle Minerals

Two of the great unanswered questions in Earth sciences are how much water, in the form of OH and/or H_2O groups, is stored in Earth's interior, and where this water is stored. Smyth (1987, 1994) and others (e.g., Bell and Rossman, 1992; Thompson, 1992; Kohlstadt et al., 1996); Ohtani et al., 2004; Huang et al., 2005) proposed that OH groups can be stored in nominally anhydrous minerals thought to be abundant in Earth's mantle, such as β-$(Mg_xFe_{1-x})_2SiO_4$ (wadsleyite) (at depths of 410-525 km) and γ-$(Mg_xFe_{1-x})_2SiO_4$ (ringwoodite) (at depths of 525-660 km), which are high-pressure polymorphs of olivine (α-$(Mg_xFe_{1-x})_2SiO_4$) (at depths of 0-410 km) (see Ito & Katsura (1989) for details). The crystal structure of wadsleyite is based on a slightly distorted cubic close-packing of oxygen anions, with four non-equivalent cations, one of which is Si^{4+} in tetrahedral coordination with oxygen and three of which are Mg^{2+} in octahedral coordination with oxygen (Horiuchi and Sawamoto, 1981). Wadsleyite is a sorosilicate with one of the oxygens (O(1)) bonded to five Mg^{2+} cations but not bonded to Si^{4+}. Smyth (1987) examined Pauling bond-strengths in the wadsleyite structure and showed that O(1) has a low incident bond-strength sum, 1.67 v.u., whereas the bond-strength sum is 2.33 v.u. for O(2) and 2.0 v.u. for the O(3) and O(4) oxygens. Based on this result and comparison of the electrostatic potentials of the oxygen sites in wadsleyite, which show that the O(1) oxygen potential is more similar to that of hydroxyl groups than oxygen, Smyth concluded that some of the O(1) oxygen sites are partially occupied by hydroxyl groups, with charge balance maintained by partial M-site vacancy. This study led Smyth (1987) to propose that β-$(Mg_xFe_{1-x})_2SiO_4$ may be a host phase for water in the middle part of

Earth's upper mantle (410-525 km). A later crystal structure analysis of monoclinic hydrous wadsleyite containing 2.24 wt% water and 4.95 wt% FeO by Smyth et al. (1997) showed that cation vacancies at Si sites and at the M(3) site are major charge-compensation mechanisms that control the amount of water in wadsleyite.

Smyth (1987) used classical Pauling bond strengths (i.e., 1.0 v.u. for $^{[4]}$Si-O bonds and 0.33 v.u. for $^{[6]}$Mg-O bonds) to calculate the bond-strength sums at the four oxygens of wadsleyite. This raises the question of how the four non-equivalent oxygens deviate from the valence-sum rule, based on Brown and Altermatt (1985) bond valences. Unlike Pauling bond strengths, the Brown-Altermatt bond valences take into account the inverse correlation between bond valence and bond length. The local coordination environments of the four non-equivalent oxygens in wadsleyite are summarized in **Table 6**, together with their bond lengths to cations, bond valences, and bond-valence sums.

Ringwoodite [γ-$(Mg_xFe_{1-x})_2SiO_4$], the highest-pressure cubic polymorph of olivine, is another candidate mineral in the Earth's deep mantle that has been proposed as a host for significant amounts of hydrogen. An experimental study by Kohlsteadt et al. (1996) on the stability of the three olivine polymorphs found up to 0.12 wt% water in olivine (Fo_{90}), up to 2.4 wt% water in hydrous wadsleyite, and up to 2.7 wt% water in hydrous ringwoodite. A recent study using IR and Raman spectroscopy, secondary ion mass spectrometry, and proton-proton scattering on ringwoodite, which is believed to be the most abundant mineral in the lower 150 km of Earth's transition zone, suggests that ringwoodite can incorporate up to 1.5 to 2 wt% H_2O as hydroxyl defects (Thomas et al., 2015).

Panero et al. (2013) did a synchrotron-based FTIR study of hydrous ringwoodite and resolved multiple IR stretching bands in Fe-bearing and Fe-free hydrous ringwoodite samples that

This is the peer-reviewed, final accepted version for American Mineralogist, published by the Mineralogical Society of America.
The published version is subject to change. Cite as Authors (Year) Title. American Mineralogist, in press.
DOI: https://doi.org/10.2138/am-2021-7938. http://www.minsocam.org/

they assigned primarily to O-H stretches at $_{Mg}$ + 2(H^+) defects. Purevjav et al. (2014; 2018) did neutron, time-of-flight, single-crystal Laue diffraction analysis of synthetic hydrous ringwoodite with the formula $Mg_{1.93}H_{0.28}Si_{0.98}O_4$ (corresponding to 1.9 (2) wt% of H_2O). They found that H^+ ions occur only at Mg sites in the ringwoodite structure, which compensates for the reduced occupancies of Mg^{2+} and Si^{4+} ions at octahedrally and tetrahedrally coordinated sites, respectively. The model most consistent with the neutron diffraction results assumes that three H^+ ions are at one vacant M site, which requires four Mg^{2+} vacancies and one Si^{4+} vacancy ($4Mg^{2+} + 1Si^{4+} \leftrightarrow 12H^+$). There is only one crystallographic M site in the ringwoodite structure, in contrast to the four different M sites in the wadsleyite structure, and a crystallographically constrained water capacity of 3.3 wt% (see Smyth, 1994). Considering the proposed exchange mechanism in ringwoodite, it has a larger water capacity in the lower half of the transition zone in Earth's mantle, compared with that of wadsleyite in the upper half of the mantle transition zone.

Based on these and other studies of the structure and properties of wadsleyite and ringwoodite (e.g., Hirschmann et al., 2005; Smyth et al., 2003, 2006; Smyth and Jacobsen, 2006; Schmandt et al., 2014), there is growing evidence that Earth's mantle could contain several ocean's worth of water in nominally anhydrous minerals such as wadsleyite and ringwoodite. Bond-valence analysis played an important role in the recognition that water in the form of hydroxyl groups is very likely present in these minerals in Earth's mantle.

Application of Bond-Valence Theory to Uranyl-Oxide and Uranyl-Oxysalt Minerals

Many oxide and oxysalt minerals conform well to the idea of binary representation of a structure wherein a complicated structure is considered as two constituents, a strongly bonded (usually anionic) structural unit and a weakly bonded (usually cationic) interstitial complex (Hawthorne, 1983). Where this is the case, we may look at the interaction between these two

constituents using the valence-matching principle (Brown, 2002a, 2016): Stable structures will form when the Lewis-acid strength of the cation closely matches the Lewis-base strength of the anion. The Lewis-acid strength of a cation can be defined as the characteristic valence of the bonds formed by that cation, and the Lewis-base strength of an anion can be defined as the characteristic valence of the bonds formed by that anion. Lewis-acid strengths of cations bonded to O^{2-} are given by Gagné and Hawthorne (2017). Lewis-base strengths for simple anions are too variable to be useful in examining structure. However, simple oxyanions, e.g., $(SO_4)^{2-}$, $(SiO_4)^{4-}$, show a much more limited variation (e.g., Brown, 2009; Hawthorne, 2012), and may be used effectively via the valence-matching principle. The valence-matching principle deals with single ion-ion interactions whereas the structural unit and the interstitial complex in many common hydroxy-hydrated oxysalt minerals are large aggregations of ions and (H_2O). If we can define a Lewis acidity for a structural unit and a Lewis basicity for an interstitial complex, we may look at the aggregate interaction between these units using the principle of correspondence of Lewis acidity-basicity (Hawthorne and Schindler, 2008), the mean-field equivalent of the valence-matching principle.

The role of (H_2O). The (H_2O) group is very important because of its polar nature: on the O^{2-} side, the group acts as an anion, whereas on the H^+ side, the group acts as a cation. As a result, an (H_2O) group may (1) moderate Lewis acidity, and (2) propagate chemical bonds to anions too distant from a cation to bond to it directly.

Consider the atomic arrangements in **Figures 15(a)** and **15(b)**. A cation, M, bonds to an anion S with a bond valence of v v.u., and a cation, M, bonds to an (H_2O) group, and the (H_2O) group bonds to anions, S. In **Figure 15(a)**, the anion receives one bond of bond valence v vu from the cation M. In **Figure 15(b)**, the donor O^{2-} ion of the (H_2O) group receives a bond valence of v v.u. from the cation; the bond-valence requirements of the donor O^{2-} ion are satisfied by two short

O^{2-}—H^{+} bonds of strength (1 – v/2) v.u.. Each H^{+} forms a hydrogen bond with an S anion to satisfy its own bond-valence requirements, and the S anion thus receives a bond valence of v/2 v.u., one half (**Figure 15(b)**) of what it received where it bonded directly to the M cation (**Figure 15(a)**). The (H_2O) group is functioning as a bond-valence transformer, dividing one bond into two bonds of half the bond valence; this type of (H_2O) group is called a transformer (H_2O) group (Hawthorne & Schindler, 2008). Consider next the atomic arrangement in **Figure 15(c)**: two cations bond to an (H_2O) group, which bonds to two anions. The O^{2-} ion receives a bond valence of 2v v.u. from the cations, and the valence-sum rule at this O^{2-} ion is satisfied by two short O-H bonds of strength (1 – v) v.u.. Each H^{+} forms a hydrogen bond with a neighboring anion, which receives the same bond valence (v v.u., **Figure 15(c)**) as where it is bonded directly to one M cation (**Figure 15(a)**). The (H_2O) group does not act as a bond-valence transformer, it is a non-transformer (H_2O) group. Consider the atomic arrangement in **Figure 15(d)**: (H_2O) is involved only in a hydrogen-bond network. In such an environment, the O^{2-} anion is usually [4]-coordinated, and the (H_2O) group participates in two O-H (donor-hydrogen) bonds and two H···O hydrogen bonds. Two hydrogen bonds of strength v v.u. are incident at the O atom of the (H_2O) group, the bond-valence requirements of the central O atom are satisfied by two O-H bonds of strength (1 – v) v.u., and each H atom forms a hydrogen bond of strength v v.u. to another anion (**Figure 15(d)**). Hence an (H_2O) group accepting two hydrogen-bonds does not modify the strengths of its existing chemical bonds, it propagates them to more distant anions, as is the case where the (H_2O) group is bonded to two cations (**Figure 15(c)**); this type of (H_2O) is also designated non-transformer (H_2O).

Calculation of Lewis-base strengths. Details of how to do this are provided by Hawthorne and Schindler (2008). To maintain electroneutrality of the entire structure, the bonds to the structural unit must neutralize the charge of the structural unit, and the Lewis basicity of the

This is the peer-reviewed, final accepted version for American Mineralogist, published by the Mineralogical Society of America.
The published version is subject to change. Cite as Authors (Year) Title. American Mineralogist, in press.
DOI: https://doi.org/10.2138/am-2021-7938. http://www.minsocam.org/

structural unit is the charge on the structural unit divided by the number of bonds to the structural unit. Thus, to calculate the Lewis basicity, we need to know (1) the effective charge on the structural unit, and (2) the number of bonds incident at the structural unit from adjacent interstitial complexes and neighboring structural units. For structural units with no H^+ ions, the effective charge on the structural unit is the formal charge. For structural units containing H^+ ions, it is necessary to account for the charge transferred from the structural unit by hydrogen bonds to external anions (commonly 0.20 v.u.; Brown, 1980; Hawthorne, 1992).

Hawthorne and Schindler (2008) defined the charge deficiency per anion (CDA) of a structural unit as its formal charge modified by any hydrogen bonds emanating from the structural unit divided by the number of anions. Examination of the crystal structures of well-refined uranyl-oxide and uranyl-oxysalt minerals shows that there is a relation between the number of bonds from the interstitial species to the structural unit and the CDA of the structural unit (**Figure 16**).

As shown in **Figure 16(a)**, the data define a band across the plot; this is to be expected as the aggregate Lewis acidity of the interstitial species depends on the Lewis acidity of the interstitial cations plus the transformer effect of interstitial (H_2O) groups. Thus, for a specific Lewis basicity of a structural unit, there is a range in the number of interstitial bonds per cation corresponding to variation in pH of the nascent aqueous solution from which the mineral crystallizes. Consider the structure of curite, $^{[9]}Pb^{2+}{}_3(H_2O)_2[(UO_2)_8O_8(OH)_6)](H_2O)$ (Li and Burns, 2000). The effective charge of the structural unit, $[(UO_2)_8O_8(OH)_6)]^{6-}$, is the formal charge minus the charge transferred from the structural unit by the constituent hydrogen bonds (-6 - 6 x 0.20) = -7.2 v.u.. There are 30 anions in the structural unit, and hence the CDA = -7.2 / 30 = 0.24 v.u.. Plotting this value on the abscissa of **Figure 16(b)** allows the range in number of bonds per anion to be read off the ordinate: 0.95-1.44. There are 30 anions in the structural unit in curite and hence the range in the number of

interstitial bonds is (0.95-1.44) x 30 = 28.5-43.2. The effective charge of the structural unit is -7.2 v.u., and hence the resulting range in Lewis basicity is 7.2 / (28.5-43.2) = 0.17-0.25 v.u..

The Lewis acidity of the interstitial complex is inversely correlated with the number of transformer (H_2O) groups and the coordination numbers of the interstitial cations. If more than one cation species is present in an interstitial complex, we may use the weighted arithmetic mean of their charge and coordination number. Where interstitial (OH^-) is present, we can sum the charges of the cation(s) and the interstitial (OH^-), and treat the complex as containing a cation of the resultant net charge, i.e., $M^{3+} + (OH)^- \equiv M^{2+}$. We may plot the range in basicity of a specific structural unit on a graph of the variation in Lewis acidity of cation complexes. Where the properties of the structural unit and the interstitial complexes intersect, the principle of correspondence of Lewis acidity-basicity is satisfied, and structures of those specific compositions are stable. Where the properties of the structural unit and interstitial complexes do not overlap, the principle of correspondence of Lewis acidity-basicity is not satisfied, and structures of those compositions are not stable.

Prediction of the amount of transformer H_2O in oxide and oxysalt structures. The variation in Lewis acidity of an interstitial complex may be shown graphically as a function of the number of transformer (H_2O) groups for specific charges and coordination numbers of cations (**Figure 17**). The range in Lewis basicity (0.17-0.25 v.u.) (calculated above) of the structural unit $[(UO_2)_8O_8(OH)_6]^{6-}$ is indicated in yellow in **Figure 17**. Immediately it is apparent that monovalent cations with coordination numbers < [6] will not occur whereas divalent cations with coordination numbers > [5] may occur with the appropriate numbers of transformer (H_2O) groups. Thus curite, $^{[9]}Pb^{2+}{}_3(H_2O)_2\{UO_2)_8O_8(OH)_6)](H_2O)$, and sayrite, $^{[9]}Pb^{2+}{}_2(H_2O)_4\{UO_2)_5O_6(OH)_6)]$, fall within the yellow band of agreement with the principle of correspondence of Lewis acidity-basicity and

are found as minerals. **Figure 18** compares the predicted and observed number of transformer H_2O groups per cation in a series of sheet-structure uranyl oxide and oxysalt minerals, and there is general correspondence within ±1 H_2O group per cation.

These arguments, based on BVT, can explain the role of, and successfully predict the amount of, transformer H_2O groups bonded to interstitial constituents in uranyl oxide and oxysalt minerals, and a variety of other oxysalt minerals: borates (Schindler and Hawthorne, 2001a,b,c), hydroxy-hydrated uranyl-oxide and oxysalts (Schindler and Hawthorne, 2004), sulfates (Schindler et al., 2006), and aluminofluorides (Hawthorne and Herwig, 2020).

Bond-Valence Analysis of Proton, Cation, and Oxyanion Adsorption at Mineral-Aqueous Solution Interfaces

The surfaces of metal-(oxyhydr)oxides and other oxide-based minerals, such as silicates, in contact with water have ionizable hydroxide sites, $\underline{X}OH$, that undergo protonation and deprotonation reactions (Stumm et al., 1970; Stumm, 1992; Schindler et al., 1976a, 1976b). These types of reactions are among the most important in the natural world (Stumm et al., 1987; Brown, 2001) and result in pH-dependent surface charge and potential, both of which are zero at a solid-specific pH value (i.e., the pH_{PZC} or pH_{PZNPC}) (Parks, 1965, 1967; Sverjensky, 1992). Although protons play a major role in the complex interfacial chemistry of oxide-based minerals in the presence of water, we have little molecular-level information about the role protons play in sorption/desorption reactions or about the structure and stoichiometry of reactive surface sites and sorption complexes at mineral-aqueous solution interfaces. As discussed below, BVT provides a simple means of placing chemically reasonable constraints on the local coordination environments and stoichiometries of mineral-aqueous solution interface species, the reactive sites on mineral surfaces to which these species adsorb, and the structural role of protons in sorption reactions.

BVT has also been used to predict pH_{PZC} values of minerals in contact with water (Sverjensky, 1992), intrinsic proton affinities of reactive surface groups of metal (hydr)oxides (Hiemstra et al., 1996), and acidity constants (pKa values) of oxyacids and hexaquo cations sorbed on oxide mineral surfaces (Bickmore et al., 2004, 2006). As shown below, the simple constraints provided by BVT can be quite useful in interpreting the results of spectroscopy and X-ray scattering experiments on mineral-aqueous solution interfaces.

The field of solid-water interface chemistry/geochemistry has experienced major growth over the past 50 years due in large part to the recognition that chemical reactions occurring at mineral-aqueous solution interfaces impact many natural and anthropogenic processes, including sorption/desorption of environmental contaminants and plant nutrients on/from mineral surfaces as well as the chemical weathering of minerals (Stumm, 1992; Brown et al., 1999). Another key reason for major advances in this field is the development of surface-sensitive **X-ray spectroscopic** (Hayes et al., 1987; Brown, 1990; Liu et al., 1999; Brown and Parks, 2001; Brown and Sturchio, 2002; Yamamoto et al., 2010; Brown and Calas, 2012) and **X-ray scattering** (Bedzyk et al., 1986, 1990; Eng et al., 2000; Fenter, 2002; Fenter and Sturchio, 2004; Trainor et al., 2004) methods that utilize very high brightness synchrotron X-ray sources. There have also been major advances in the application of synchrotron-based **X-ray photoelectron spectroscopy** (XPS), including near-ambient pressure XPS (AP-XPS) (Yamamoto et al., 2010; Newberg et al., 2011) and Standing Wave Ambient Pressure Photoelectron Spectroscopy (SWAPPS) (Nemsak et al., 2014). In addition, advances in surface-sensitive infrared spectroscopy (attenuated total reflectance Fourier transform infrared or ATR-FTIR) have resulted in improved understanding of the interaction of organic molecules, oxyanions, and water with mineral surfaces, including the surfaces of atmospheric aerosol particles and natural nanoparticles such as ferrihydrite (e.g., Arai

and Sparks, 2001; Al-Abadleh and Grassian, 2003a, 2003b; Usher et al., 2003; Yoon et al., 2004; Johnson et al., 2005; Carabante et al., 2010).

Synchrotron-based X-ray absorption fine structure (XAFS) spectroscopy has become the experimental method of choice for characterizing sorbed metal-ion complexes at mineral-water interfaces since it was first used for this purpose (Hayes et al., 1987). Synchrotron-based X-ray scattering methods, such as X-ray reflectivity and crystal truncation rod (CTR) diffraction, provide critical information on the average molecular-level structure of hydrated mineral surfaces, which is essential for understanding differences in chemical reactivity of different mineral surfaces. However, neither of these methods is capable of providing detailed information about the association of protons with oxo, hydroxo, or aquo groups on hydrated mineral surfaces. This is true because X-rays are relatively insensitive to protons due to their limited X-ray scattering power.

Quantum chemical modelling of mineral-water interfaces at the DFT level can also provide quantitative information on the structure and bonding of metal complexes on hydrated mineral surfaces as well as the distribution of surface-bound protons (e.g., Mason et al., 2009, 2010, 2011). However, such studies are relatively rare to date because of the complexity of these types of calculations, particularly those involving the structure and properties of interfacial water (e.g., Bandura et al., 2004; Aboud et al., 2011). Clearly consistent with the electron density distribution in minerals and molecules (see earlier section on Pauling's second rule), BVT provides a simple way of obtaining information of this type.

Our approach combines (1) BVT (Brown and Altermatt, 1985) to calculate bond valences of sorption complexes; (2) XAFS spectroscopy (e.g., Hayes et al., 1987) to determine the structure, stoichiometry, and mode of attachment of metal ion complexes to hydrated mineral surfaces; and (3) surface X-ray scattering (e.g., Trainor et al., 2004; Ghose et al., 2010) to determine the average

This is the peer-reviewed, final accepted version for American Mineralogist, published by the Mineralogical Society of America.
The published version is subject to change. Cite as Authors (Year) Title. American Mineralogist, in press.
DOI: https://doi.org/10.2138/am-2021-7938. http://www.minsocam.org/

hydrated surface structure. The variation of M-O bond valence, $s_{M\text{-}O}$, with M-O bond length ($r_{M\text{-}O}$) was defined by Brown and Altermatt (1985) as:

$$s_{M\text{-}O} = \exp [(r_0 - r_{M\text{-}O}) / 0.37] \text{ valence units (v.u.)} \quad [10]$$

where r_0 depends upon the identity and formal valence of the cation and values of r_0 were empirically determined by fitting **eq. 10** to known oxide crystal structures (Brown and Altermatt, 1985).

Bargar et al. (1997a,c) used the bond-valence approach, coupled with carefully determined O-H bond lengths in crystalline materials using neutron diffraction, to show that the range of O-H bond lengths at metal oxide-aqueous solution interfaces is approximately 1.03 Å to 0.95 Å, which results in bond valences of $0.68 \leq s_{OH} \leq 0.88$ v.u. for surface hydroxyls (Bargar et al., 1997a). The corresponding range of realistic hydrogen bond lengths was shown to be 1.65 Å to 2.50 Å, which gives a range of bond valences for H-bonds, $s_{o\ldots H}$, of 0.25 to 0.13 v.u., respectively. These results were used by Bargar et al. (1997c) to derive a more accurate description of O-H bond valence (**eq. 11**) (**Figure 19**) than **eq. 10**:

$$s_{OH} = 0.241 / (R_{OH} - 0.677) \text{ (v.u.)} \quad [11]$$

This bond-valence—bond-length relation for O-H bonds was used by Bargar et al. (1997a,b,c) and Towle et al. (1999) to constrain the types of hydrogen bonds and hydroxo and aquo groups that can form as a result of the sorption of aqueous Co^{2+} and Pb^{2+} on oriented single-crystal alumina and hematite surfaces in contact with water, as will be discussed below for alumina surfaces. We have also used this relation to help evaluate the stability of different types of surface complexes of selenate and selenite oxyanions sorbed at the α-FeOOH-aqueous solution interface, as discussed in the next sub-section.

This is the peer-reviewed, final accepted version for American Mineralogist, published by the Mineralogical Society of America.
The published version is subject to change. Cite as Authors (Year) Title. American Mineralogist, in press.
DOI: https://doi.org/10.2138/am-2021-7938. http://www.minsocam.org/

Sorption of selenate and selenite oxyanions at the goethite-water interface. We begin with the sorption of aqueous selenate $(Se^{6+}O_4)^{2-}$ and selenite $(Se^{4+}O_3)^{2-}$ oxyanions on α-FeOOH (goethite) surfaces in contact with water. Selenium in these oxidized forms is a toxic environmental contaminant in soils and groundwaters, particularly in the western U.S. and western China. Knowledge of the molecular-level speciation of Se is required to assess its potential toxicity and bioavailability (Pickering et al., 1995). To provide this type of information, we did an XAFS spectroscopic study of aqueous selenate and selenite oxyanions sorbed on goethite particles in contact with water (Hayes et al., 1987). The XAFS spectrum of selenate shows a single frequency corresponding to four $^{[4]}Se^{6+}$-O bonds with an average $^{[4]}Se^{6+}$-O bond length of 1.65 Å. This spectrum is identical to that of selenate oxyanions in a 25 mM aqueous solution (no goethite particles), and shows that selenate forms dominantly outer-sphere complexes on hydrated goethite particle surfaces (Hayes et al., 1987) (**Figure 20**). In contrast, the XAFS spectrum of selenite sorbed on goethite consists of two frequencies, which when Fourier transformed, correspond to three $^{[3]}Se^{4+}$-O bonds at 1.70 Å and two $^{[3]}Se^{4+}$-O-$^{[6]}Fe^{3+}$ linkages, with an Se-Fe distance of 3.38 Å. As illustrated in **Figure 20(e)**, the presence of two $^{[3]}Se^{4+}$-O-$^{[6]}Fe^{3+}$ linkages indicates that selenite is adsorbed dominantly as inner-sphere, bidentate complexes on hydrated goethite particle surfaces.

Also shown in **Figure 20** are the Brown-Altermatt bond valences of the Se-O bonds in selenate and selenite oxyanions (1.452 v.u. and 1.35 v.u., respectively, calculated using the empirical parameter r_0 of 1.788 Å for $^{[4]}Se^{6+}$-O and 1.811 Å for $^{[3]}Se^{4+}$-O). Beginning with selenate oxyanions, if we assume that an average oxygen on the hydrated goethite surface is bonded to one $^{[4]}Se^{6+}$ ion and two $^{[6]}Fe^{3+}$ ions but no protons (**Figure 20(e)**), with an $^{[4]}Se^{6+}$-O distance of 1.65 Å (Hayes et al., 1987) and an $^{[6]}Fe^{3+}$-O distances of ~2.10 Å (Wang et al., 2006), the bond-valence

sum at the oxygen is 2.25 v.u. (1.452 v.u. + 0.398 v.u. + 0.398 v.u.) (using an r_0 value of 1.759 Å for $^{[6]}Fe^{3+}$-O), which departs from the valence-sum rule. The lack of accord with the valence-sum rule is even greater if this oxygen is a hydroxo group (with a bond-valence contribution of ~ 0.8 v.u. and a bond-valence sum of ~3.05 v.u.) or if it is weakly H-bonded to a nearby water molecule (with a bond-valence contribution of ~ 0.2 v.u. and a bond-valence sum of ~2.45 v.u.). If we assume that a $^{IV}Se^{6+}$ ion and two $^{[6]}Fe^{3+}$ ions are bonded to an O1 oxygen at the goethite-water interface, using the Fe-O1 distance of 1.956 Å (Wang et al., 2006), which corresponds to a bond valence of 0.587 v.u., the bond-valence sum is ~2.63 v.u.. This bond-valence analysis indicates that fully hydrated selenate oxyanions should form dominantly outer-sphere complexes at the goethite-water interface, as was shown to be the case using XAFS spectroscopy. This result helps explain the ionic-strength dependence of selenate uptake from aqueous solution onto goethite particle surfaces as a function of pH. The reasoning here is that increasing ionic strength would move the isotherm for a weakly bound, outer-sphere sorption complex to lower pH values, as observed, but would not affect the isotherm of a strongly bound, inner-sphere complex, which we also observed. It also explains why significant uptake of selenate onto goethite does not begin until pH values well below the pH_{PZC} of goethite (~9.0: Sverjensky, 1994) (**Figure 21**), where the goethite surface in contact with water should have a near-zero charge. This type of behavior is consistent with an increasing electrostatic attraction between the negatively charged selenate oxyanion and the increasingly positively charged goethite surface as pH decreases.

A similar bond-valence analysis of selenite sorbed at the goethite-water interface is also consistent with our XAFS spectroscopy results, which show that selenite oxyanions form dominantly inner-sphere, bidentate surface complexes at the goethite-water interface. Assuming such a surface complex (**Figure 20(e)**), the bond-valence sum at an oxygen ion on the goethite

This is the peer-reviewed, final accepted version for American Mineralogist, published by the Mineralogical Society of America.
The published version is subject to change. Cite as Authors (Year) Title. American Mineralogist, in press.
DOI: https://doi.org/10.2138/am-2021-7938. http://www.minsocam.org/

surface bonded to a $^{[3]}Se^{4+}$ ion at a distance of 1.70 Å (1.35 v.u.) and to two $^{[6]}Fe^{3+}$ in the goethite surface structure, with an $^{[6]}Fe^{3+}$-O distance of ~2.10 Å (Wang et al., 2006) (0.398 v.u.) would be ~2.15 v.u.. Lengthening the two $^{[6]}Fe^{3+}$-O surface bonds to ~2.15 Å would reduce this sum to ~2.04 v.u. Adsorption of this type of selenite surface complex would also require deprotonation of the surface hydroxo group to which it bonds.

At the time this study was done, we did not have good structural models for the most common goethite surfaces (e.g., the (100) cleavage surface) in contact with water, so we assumed that the average structure of a goethite particle surface is a simple termination of the bulk structure, which is a slightly distorted hexagonal close-packed O-atom arrangement with Fe atoms occupying one-half of the octahedral interstices. The $^{[6]}Fe^{3+}O_6$ octahedra share edges to form double chains parallel to c. There are two distinct oxygen sites, O1 and O2, both of which are coordinated to three Fe^{3+} ions; the O2 oxygen is also bonded to a proton at a distance of 0.88 Å (Yang et al., 2006). The Fe-O1 distance is 1.956 Å, and the Fe-O_2H distances are 2.100 Å and 2.106 Å. Some years later, Ghose et al. (2010) procured a natural goethite specimen with a (100) cleavage surface suitable for crystal truncation rod diffraction analysis. Their study showed that the goethite (100)-water interface structure is a double-hydroxyl, double-water terminated interface with significant atom relaxations and an interface stoichiometry of (H_2O)-(H_2O)-OH_2-OH-Fe-O-O-Fe-R), where R represents the bulk goethite structure. Two types of terminal hydroxyls were identified by Ghose et al. (2010), based on bond-valence analysis, including a bidentate (B-type) hydroxo group and a monodentate (A-type) aquo group, both of which can act as Lewis base sites. This analysis assumed that adding a proton to a surface oxygen to form a hydroxo group resulted in a bond-valence contribution of ~0.8 v.u. to the oxygen, and that a hydrogen bond contributed ~0.2 v.u. (see **Figure 19**). The double hydroxyl-terminated surface

dominates, with an 89% contribution to the (100) cleavage surface structure. The B-type hydroxo groups are bonded to two $^{VI}Fe^{3+}$ ions. The surface Fe-OH bond lengths are 2.16 Å ± 0.03 Å and 2.09 Å ± 0.03 Å, which are close to the bulk-structure Fe-OH distances. Using these Fe-(O,OH) distances for the hydrated goethite surface to calculate bond valences results in values ranging from 0.409 v.u. to 0.338 v.u., which reduces the slight predicted excess bond-valence at the surface oxygen to which the selenite oxyanion is bonded ($\Sigma s = 2.04$ v.u.). The fact that selenate oxyanions form dominantly weakly-bound outer-sphere sorption complexes on common Fe^{3+}-oxyhydroxides and that selenite forms more strongly-bound bidentate inner-sphere complexes explains why selenate can easily desorb from goethite surfaces and be transported in surface and ground waters, resulting in a greater environmental impact than selenite.

Sorption of aqueous Pb^{2+} and Co^{2+} at alumina-water interfaces. Next, we show how bond-valence analysis can be combined with XAFS spectroscopic analysis and CTR diffraction results to determine the type(s) of sorption complexes of aqueous Pb^{2+} and Co^{2+} at surface functional groups on α-Al_2O_3 (0001) and (1-102) surfaces in the presence of water (Bargar et al., 1996, 1997a,b,c; Towle et al., 1999; Eng et al., 2000; Trainor et al., 2002).

There is dramatically less uptake of Pb^{2+} on the hydrated α-Al_2O_3 (0001) surface than on the hydrated α-Al_2O_3 (1-102) surface (sorption density $\Gamma = 0.1 \pm 0.05$ μmoles/m^2 on (0001) vs. $\Gamma = 1.7 \pm 0.1$ μmoles/m^2 on (1-102) (Bargar et al., 1997c). The density of surface functional groups is about the same on both surfaces, so the free energy of Pb^{2+} adsorption is roughly 20 times lower on the hydrated α-Al_2O_3 (0001) surface than on the hydrated α-Al_2O_3 (1-102) surface. XAFS spectroscopic measurements on Pb^{2+} sorbed on powdered α-Al_2O_3 in contact with water indicate that Pb^{2+} forms dominantly inner-sphere bidentate complexes with average Pb-O distances ranging from 2.2 to 2.3 Å, which are consistent with an average coordination number of 3 to 4 (oxygens)

This is the peer-reviewed, final accepted version for American Mineralogist, published by the Mineralogical Society of America.
The published version is subject to change. Cite as Authors (Year) Title. American Mineralogist, in press.
DOI: https://doi.org/10.2138/am-2021-7938. http://www.minsocam.org/

(Bargar et al., 1997a). In contrast, grazing-incidence (GI) XAFS spectroscopy showed that aqueous Pb^{2+} forms dominantly outer-sphere complexes on the α-Al_2O_3 (0001) surface in the presence of water (Bargar et al., 1996).

XAFS spectroscopy results for Pb^{2+} sorbed at the α-Al_2O_3(1-102)-aqueous solution interface indicate that Pb^{2+}forms dominantly inner-sphere complexes. When Pb^{2+} bonds to a 3-coordinated oxo group (i.e., Al_3-O) on the α-Al_2O_3 (1-102) surface, it becomes 4-coordinated by oxygens, with an average XAFS-derived $^{[4]}$Pb-O distance of 2.25 Å.

To help interpret the results of XAFS spectroscopic analysis, Bargar et al. (1997c) did a bond-valence analysis of the possible functional groups on the hydrated α-Al_2O_3 (0001) and (1-102) surfaces, assuming the surface structures are simple terminations of the bulk structure (**Figure 22; Tables 7** and **8**). This analysis revealed that α-Al_2O_3(0001) is dominated by Al_2-OH sites and indicates that an Al_2-OH-Pb bonding configuration is not stable because the oxygens in these complexes would be significantly oversaturated, with a bond-valence sum of 2.21 v.u. (**Figure 22**). In order for such a surface complex to form, Pb^{2+} adions must replace H^+ in the Al_2-OH surface groups; however, as shown in **Figure 22** (center surface complex), this replacement would cause a coordinatively saturated surface oxygen to become significantly undersaturated and therefore is unlikely to occur (Bargar et al., 1997c).

Instead, as shown by **eq. 12**, Pb^{2+} forms dominantly outer-sphere complexes:

$$\textbf{(}0001\text{):} \quad [^{Al}_{Al} > OH]_3 + Pb^{2+}(aq) = [^{Al}_{Al} > (OH)]_3 \cdot\cdot\cdot Pb^{2+} \qquad [12]$$

This prediction is consistent with the results of Pb L_3-edge XAFS spectroscopic analysis, which shows that Pb^{2+} forms dominantly outer-sphere complexes at the α-Al_2O_3 (0001)-aqueous solution interface (Bargar et al., 1996, 1997c). It is also consistent with our CTR diffraction study

This is the peer-reviewed, final accepted version for American Mineralogist, published by the Mineralogical Society of America.
The published version is subject to change. Cite as Authors (Year) Title. American Mineralogist, in press.
DOI: https://doi.org/10.2138/am-2021-7938. http://www.minsocam.org/

of the hydrated α-Al_2O_3 (0001) surface (Eng et al., 2000), which shows that doubly-coordinated surface functional groups (Al_2-OH) are the dominant type of surface site on the hydrated (0001) surface.

In the case of sorption of aqueous Pb^{2+} on α-Al_2O_3(1-102), bond-valence analysis (**Table 8**) predicts that the most stable bonding configuration is the bonding of Pb^{2+} to Al_3-O surface sites. A less favorable but plausible configuration is Pb^{2+} bonding to singly-coordinated hydroxo groups (Al-OH) (**Table 8**). Our CTR diffraction study of the hydrated α-Al_2O_3 (1-102) surface (Trainor et al., 2002), shows that this surface in the presence of water has roughly equal numbers of oxygens coordinated by one, two, and three $^{[6]}Al^{3+}$ ions. **Equation 13** was chosen to illustrate the reaction of aqueous $Pb^{2+}(H_2O)_4$ complexes with Al_3-O and Al-O surface functional groups on the α-Al_2O_3 (1-102) surface.

$$\text{(1-102):}\quad \left(\begin{matrix}\text{Al}\\ \text{Al}\end{matrix}\!\!>\text{O}\right) + (\text{Al-OH}_2) + \text{Pb}^{2+}(\text{H}_2\text{O})_4 = \left[\left(\begin{matrix}\text{Al}\\ \text{Al}\end{matrix}\!\!>\text{O}\right)(\text{Al-O})\right] \text{Pb}(\text{H}_2\text{O})_2 + 2\text{H}_3\text{O}^+ \qquad [13]$$

The $^{[4]}$Pb-O bond valence for the observed Pb-O distance (2.25 Å) is 0.53 v.u. using the I. D. Brown and Altermatt (1985) bond-valence parameters. Each of the $^{[6]}$Al-O bonds contributes ~0.5 v.u., so the sum of bond valences to a 4-coordinated surface oxo group on α-Al_2O_3(1-102) that is also bonded to $^{[4]}Pb^{2+}$ is ~2 v.u.. This bonding configuration satisfies Pauling's 2nd rule and thus is predicted to be stable (**Table 8**).

Grazing-incidence XAFS spectroscopic measurements of aqueous Co^{2+} sorbed on these two alumina surfaces show that Co^{2+} forms inner-sphere complexes (Co-O distances of 2.05 to 2.10 Å, depending on whether the X-ray beam was normal to the surface or perpendicular to it) on

This is the peer-reviewed, final accepted version for American Mineralogist, published by the Mineralogical Society of America.
The published version is subject to change. Cite as Authors (Year) Title. American Mineralogist, in press.
DOI: https://doi.org/10.2138/am-2021-7938. http://www.minsocam.org/

both the (0001) and the (1-102) surfaces of α-Al_2O_3 (Towle et al., 1999). From our CTR diffraction study of the hydrated α-Al_2O_3 (1-102) surface (Trainor et al., 2002), we know that this surface in contact with water has roughly equal numbers of oxygens coordinated by one, two, and three $^{VI}Al^{3+}$ ions.

The most plausible sorption reaction for aqueous Co^{2+} on the α-Al_2O_3 (0001) surface, based on XAFS and CTR results and bond-valence analysis (**Table 7**), is given by **eq. 14**,

(0001): $$\left[\begin{matrix}Al\\ \\ Al\end{matrix}\!\!>OH\right]_3 + Co^{2+}(H_2O)_6 = \left[\begin{matrix}Al\\ \\ Al\end{matrix}\!\!>OH\right]_3\ Co^{2+}(H_2O)_3 + 3H_2O \qquad [14]$$

which indicates that Co^{2+} adsorbs dominantly to doubly-coordinated hydroxo groups in a tridentate configuration above tetrahedra interstices (Bargar et al., 1997c; Towle et al., 1999). As shown in **Figure 19**, this bonding configuration results in a bond-valence sum of 2.03 v.u., whereas a similar bonding configuration for the hypothetical Al_2-OH-Pb inner-sphere sorption complex would have a bond-valence sum of 2.21 v.u. and is therefore predicted to be unstable. This difference in the bond-valence sums of the Al_2-OH-$^{[6]}Co^{2+}$ and Al_2-OH-$^{[3]}Pb^{2+}$ sorption complexes is due to the fact that the first coordination shell of sorbed Co^{2+} consists of six oxo or hydroxo groups ($^{[6]}Co^{2+}$-O bond valence of 0.35 v.u.), whereas the first coordination shell of sorbed Pb^{2+} would consist of only four oxo groups.

An example of a dominant sorption reaction of aqueous Co^{2+} on the α-Al_2O_3 (1-102) surface in the presence of water is shown in **eq. 15** (Bargar et al., 1997c).

(1-102): $$\left(\begin{matrix}Al\\ Al\!\!\geqslant O\\ Al\end{matrix}\right)_2 + (Al\text{-}OH_2)_3 + Co^{2+}(H_2O)_6$$

$$= \left[\left(\begin{matrix}Al\\ Al\!\!\geqslant O\\ Al\end{matrix}\right)_2 \left(\begin{matrix}Al\\ \\ Al\end{matrix}\!\!>OH\right)\ (Al\text{-}OH)\right] Co^{2+}(H_2O)_2 + 2H^+ + 5H_2O \qquad [15]$$

This is the peer-reviewed, final accepted version for American Mineralogist, published by the Mineralogical Society of America.
The published version is subject to change. Cite as Authors (Year) Title. American Mineralogist, in press.
DOI: https://doi.org/10.2138/am-2021-7938. http://www.minsocam.org/

Comparison of predictions of Bond Valence Theory with Density Functional Theory results for Pb^{2+} sorption on hydrated α-Al_2O_3 (1-102) and (0001). We now address the results of a density functional theory (DFT) study of Pb^{2+} sorption on the α-Al_2O_3 (0001) and (1-102) surfaces based on Pb/α-Al_2O_3 DFT surface geometry optimization (Mason et al., 2011) and compare the predictions with those from BVT.

Mason et al. (2011) used DFT-GGA to optimize the geometry of Pb^{2+} sorbed on the hydrated (0001) and (1-102) surfaces of α-Al_2O_3. They identified four optimized bonding configurations – one for the (0001) surface, which is dominated by doubly-coordinated Al_2-OH functional groups, and three for the hydrated (1-102) surface, which contains equal numbers of singly-, doubly-, and triply-coordinated functional groups (i.e., Al-O, Al_2-O), and Al_3-O). They ascribed the greater reactivity of the hydrated α-Al_2O_3 (1-102) surface relative to the α-Al_2O_3 (0001) surface with respect to aqueous Pb^{2+} cations to the ability of oxygen functional groups in the corrugated (1-102) surface to hybridize more effectively with Pb^{2+} electronic states than oxygen functional groups in the topologically flat (0001) surface. Mason et al. (2011) also did a bond-valence analysis of the four DFT geometry-optimized bonding configurations and found that the Pb^{2+} in the Pb^{2+}/(0001) configuration had significant excess bond-valence (sum of 2.30 v.u.), which is consistent with the bond-valence predictions made earlier for this bonding configuration by Bargar et al. (1997c). In contrast, Mason et al. (2011) found that their DFT-optimized Pb^{2+}/(1-102) configurations had bond-valence sums at the Pb^{2+} cations in the surface complexes of 1.71, 1.76, and 1.87 v.u.. They ascribe the non-ideal bond-valence sums to a break-down of the bond-valence model and suggest that a limitation of the bond-valence model in predicting surface complexation geometries is the parameterization, which relies on well-characterized bulk

reference structures. Mason et al. (2011) also suggest that the DFT Pb^{2+}/(1-102) configurations "are not severely under-coordinated, as indicated by the valence sums". Instead, they suggest that the bond-valence model needs to account for the angles between the central atom and all coordinating species. In the case of Pb^{2+}/(1-102) adsorption complexes, they point out that Pb-O bonding has a strong directional dependence and is able to "participate in bonding through both side-to-side and top-to-bottom orbital overlap with oxygen p states". Although the Mason et al. (2011) study did not account for the effects of explicit hydration, they suggested that the under-coordinated Pb^{2+} cations on the (1-102) surface will be reactive to water molecules. As shown in **Figure 19**, hydrogen bonding at distances of 1.65 Å to 2.50 Å between a water molecule and the Pb^{2+}/(1-102) surface complex would result in an additional bond-valence contribution of 0.25 to 0.13 v.u., which would reduce or eliminate the bond-valence deficiency at the Pb^{2+} cations in the surface complex.

Bond-Valence and XAFS Analysis of the Local Coordination Environments of Highly Charged Cations in Silicate Glasses

Bond-valence theory can also be used to constrain the local coordination environments of cations in aluminosilicate glasses and melts, as will be demonstrated below. Because these types of Earth materials have no long-range order at the molecular level, determining the local environments of cations in them is challenging. Most structural information on glasses and melts has come from X-ray scattering methods (e.g., vitreous SiO_2; Mozzi and Warren, 1969; $NaAlSi_3O_8$ (albite)-composition glass; Taylor and Brown, 1979). However, the development of XAFS spectroscopy in the early 1970's (Sayers et al., 1971), resulted in a new method that could provide quantitative, short-range structural information on virtually any element in all types of materials (gas, liquid, solid (crystalline or non-crystalline), and at mineral-water interfaces). By combining the results of XAFS spectroscopy with bond-valence analysis, we can gain additional insights

about the local coordination environments of cations in silicate glasses and melts. Here we examine the local coordination environment of a highly charged cation (Zr^{4+}) in aluminosilicate glass using this approach.

Bond-valence analysis of Zr^{4+}environments in aluminosilicate glasses. Farges et al. (1991) did a detailed XAFS spectroscopic study of the incompatible element Zr^{4+} in aluminosilicate glass and showed that plausible local structural models for Zr^{4+} and other ions in aluminosilicate glasses and melts can be developed using bond-valence theory. The following discussion draws heavily from our earlier study (Farges et al., 1991). Bond-length–bond-valence plots for each M-O bond type present in the glasses studied (**Figure 23**) can be used to adjust their classical Pauling bond strengths ($s_{(IV)Si-O}$ = 1.0 v.u.; $s_{(IV)Al-O}$ = 0.75 v.u.; $s_{(VI)Zr-O}$ = 0.67; $s_{(VIII)Zr-O}$ = 0.5 v.u.; $s_{(VI)Na-O}$ = 0.167 v.u.) for variations in bond length. However, the basic requirement of Pauling's second rule should still be valid in predicting the local coordination environments in these glasses, based on the observation by Gibbs (1982; 1987) that the short-ranged bonding forces in the simple oxyhydride molecule H_6Si_2O are similar to those in quartz and result in bond lengths and bond angles that are virtually the same. In developing possible models for the local environment of Zr^{4+} in silicate glasses, Farges et al. (1991) also accounted for the possibility of variations in individual cation-oxygen distances in a glass or melt structure, where the constraints of periodicity are relaxed. Consideration of numerous, well-refined sodium aluminosilicate structures showed that individual Si-O bonds may vary between about 1.54 Å and 1.70 Å, with bond valences ranging between 1.28 and 0.82 v.u., respectively, and that individual Al-O bonds can vary between about 1.63 Å and 1.82 Å, with bond valences between 1.04 and 0.63 v.u., respectively. Similarly, Na-O bond lengths may vary from about 2.2 Å to 3.4 Å with bond valences between 0.29 and < 0.02 v.u., respectively. Individual Zr-O bond lengths show less variation in

crystal structures, with values between about 2.03 Å and 2.11 Å for 6-coordinated Zr and 2.13 Å to 2.35 Å for 8- coordinated Zr, corresponding to bond valences between 0.78 and 0.30 v.u.. Adjustments of Si-O, Al-O, and Na-O bond lengths within these limits for a given molecular model (see **Figures 24** and **25**) such that the total bond valence to each type of oxygen is near 2.0 v.u. can be made to test the validity of different models with R(Zr-O) fixed at the XAFS-derived value (2.07 Å).

This modeling indicates that 6-coordinated Zr^{4+} cannot bond directly to a bridging oxygen in the albite-composition glass/melt network at the observed R(Zr-O) distance (2.07 Å) without significantly lengthening (Si,Al)-O bonds and disrupting the tetrahedral network. For example, if $^{[6]}$Zr bonded directly to Si-O-Si or Si-O-Al linkages (**Figure 24(a)**), the Si-O and Al-O bonds would be required to lengthen beyond their observed maximum value in aluminosilicates in order to result in a bond valence near 2.0 v.u.. This is unlikely. It is possible that $^{[6]}$Zr bonds in part to Al-O-Al linkages. Although such linkages are less likely than Si-O-Si and Si-O-Al linkages in sodium aluminosilicate glasses, they may be stabilized by $^{[6]}$Zr. However, it is unlikely that a major portion of the Zr in the glass studied bonds preferentially to bridging oxygens in Al-O-Al linkages because of the observed decrease in Zr solubility in peraluminous melts relative to peralkaline melts (Watson, 1979). An alternative configuration could have $^{[6]}$Zr bonding to a Si-O linkage without other charge-balancing cations (**Figure 24(a)**); however, this would require the Si-O bond to shorten its minimum observed value, which is also unlikely. A more likely structural configuration is the linkage of $^{[6]}$Zr to several non-bridging oxygens as shown in **Figure 24(b)**. In this model, the bond-valence sums at the three types of oxygens shown are within 0.1 v.u. of satisfying the valence-sum rule and our XAFS results. In contrast, 8-coordinated Zr is predicted to bond preferentially to bridging oxygens (**Figure 25(b)**) rather than non-bridging oxygens (**Figure**

This is the peer-reviewed, final accepted version for American Mineralogist, published by the Mineralogical Society of America.
The published version is subject to change. Cite as Authors (Year) Title. American Mineralogist, in press.
DOI: https://doi.org/10.2138/am-2021-7938. http://www.minsocam.org/

24(a)) on the basis of similar bond-valence bond-length reasoning. However, better local charge balance can be achieved where $^{[8]}Zr$ bonds to Al-O-Si linkages rather than to Si-O-Si linkages. In the latter case, Si-O bonds would be required to lengthen to their maximum values, whereas in the former case much less change in length from average observed values is required. The thermodynamic activity of Zr would be predicted to be highest in a melt with a local environment like those shown in **Figures 24(a) and 25(a)** and lowest in a melt where Zr is bonded stably to nonbridging (**Figure 24(b)**) or bridging oxygens (**Figure 25(b)**).

Based on the above analysis of Zr^{4+} in albite-composition glass, $^{[6]}Zr^{4+}$ should locally depolymerize the glass/melt tetrahedral network in order to accord with the valence-sum rule. The small amount of 8-coordinated Zr detected in albite-composition glass would most likely be accommodated within voids in the tetrahedron network if the voids expand around $^{[8]}Zr$ relative to the Zr-free albite-composition glass structure (i.e., the Si-O and Al-O bonds locally lengthen and their bond valences are lowered) (**Figure 22(b)**).

Bond-valence analysis of $U^{4+,5+,6+}$ and Ti^{4+} environments in aluminosilicate glasses. A similar XAFS-bond valence approach was used by Farges et al. (1992) to constrain the local coordination environments of U^{4+}, U^{5+}, and U^{6+} cations in silicate glasses and melts. Bond valence-bond length calculations and constraints placed on loca1 bonding by the valence-sum rule suggest that U^{4+} and U^{5+} in 6-coordinated sites in silicate melts will preferentially bond to nonbridging oxygens (NBO's) rather than bridging oxygens (BO's). The unusually low 6-fold coordination of U^{4+} and U^{5+} in relatively depoIymerized silicate melts (e.g., peralkaline and halogen-rich melts) results in a high U-O bond valence in the melt that is not observed in crystalline U-bearing minerals. This difference in bond valence is partially responsible for the small crystal-melt partition coefficients of U^{4+}.

Farges et al. (1996a,b) did a similar XAFS-bond-valence analysis to determine the local coordination environments of Ti^{4+} in Na-, K-, and Ca-titanosilicate glasses, resulting in the discovery that [5]-coordinated Ti^{4+} in distorted square pyramids ($(^{[5]}TiO)O_4$) is the dominant Ti species in the glasses, with one short Ti=O titanyl distance (1.67-1.70 ± 0.03 Å) and four long Ti-O distances (1.94-1.95 ±0.02 Å). In addition, minor amounts of $^{[4]}$Ti were detected, with the proportion of $^{[4]}$Ti increasing in the order: Na glasses < K glasses. Bond-valence modeling explains why the relative proportions of $^{[4]}$Ti and $^{[5]}$Ti change when the type of low-field-strength cation (Na^+, K^+) or the type of network-forming cation ($^{[4]}Si^{4+}$ vs. $^{[4]}P^{5+}$) changes in oxide glasses. These models also provide a structural basis for the study of glasses and melts at higher temperatures Farges et al. (1996a,b).

IMPLICATIONS

Experimental and calculated electron-density distributions determined for oxide and silicate crystals and siloxane molecules during the last decade have provided a new perspective on the classic foundation of the crystal chemistry of oxide-based minerals, including atomic/ionic radii, the radius-ratio rule, and the connection of Pauling's bond strength with resonance bond number and bond length. The electron density of a bonded oxygen atom is often highly distorted with its bonded radius decreasing systematically from 1.38 Å, when bonded to highly electropositive atoms like sodium, to 0.64 Å, when bonded to highly electronegative atoms like nitrogen. Bonded radii determined for metal atoms match the Shannon (1976) radii for the more electropositive atoms, but the match decreases systematically as the electronegativities of the M atoms increase.

George et al. (2020) concluded that their statistical study of Pauling's rules calls for a new set of empirical rules that extend and improve the rules. They go on to say "Our analysis and the

data set of connectivity and local environment provide a first step towards building a new theory that could potentially benefit from the recent growth in the use of "machine learning techniques in chemistry and materials science". This statement is surprising as George et al. (2020) have not considered the large body of work that has built on Pauling's rules and has greatly expanded our understanding of crystal structures and their participation in dynamic processes such as adsorption, dissolution and diffusion. We subscribe to the authors' citation of several of our theoretical calculations, but are puzzled by the omission of the information content and the conclusions contained in our published papers that support the conclusions drawn from the studies presented here. These studies show the close agreement obtained between the Pauling strength of a bonded interaction and the accumulation of electron density in a Si-O bonded interaction. This is compelling evidence of Pauling's genius in choosing a simple yet powerful parameter, the bond strength, as a measure of the strength of a bonded interaction. Further, the bond paths of the atoms in a crystal structure, as stated in our modification of Pauling's first rule, not only define the bonded radii of atoms, but also constrain their coordination numbers and bond strengths and the connections between the bonded interactions and the electron density as was done by Gibbs et al. (2013a). This study also shows that the O atom is not in general spherical with a well-defined radius, but it is often highly polarized when bonded to several different metal atoms with different valences, electronegativities, and bonded radii. However, the electron density distributions for the O atoms comprising crystals that contain only one kind of M atom, like the silica polymorphs where r_b(O) ranges between 0.995 Å and 0.946 Å for quartz, 0.937 Å and 0.938 Å for cristobalite, 0.932 Å and 0.952 Å for coesite and 1.047 Å and 1.071 Å for stishovite, are undistorted by the bonded interactions.

Pauling's second rule assigns a bond strength to a bonded pair of atoms that depends only on the formal valence and the coordination number of the central cation or anion. Later studies showed that the bond strength is an inverse function of bond length (e.g., Zachariasen (1954); Brown and Shannon (1973)), and the resulting bond strengths calculated from the observed chemical bonds are called bond valences to avoid confusion with Pauling bond-strengths. Brown (1980) developed Bond-Valence Theory, which has evolved enormously over the last 40 years (Brown, 2002, 2016). BVT is based on three axioms: (1) The valence-sum rule (a generalization of Pauling's second rule): The sum of the bond valences at each ion is equal to the magnitude of the atomic valence, which is a corollary of Gauss's flux theorem applied to the electrostatic potential field. (2) The path rule (originally described as the loop rule): The sum of the directed bond-valences along any path between crystallographically equivalent ions is equal to zero, which is dictated by the conservation of electric charge via Maxwell's third equation. (3) The valence-matching principle: Stable structures will form where the Lewis-acid strength of the cation closely matches the Lewis-base strength of the anion, which is based on the handshaking principle in Graph Theory. The valence-matching principle is the most powerful idea in BVT as it allows us to interpret known structures or compounds. We can also test the stability of possible compounds (in terms of whether they can or cannot exist), which moves us from a posteriori to a priori analysis.

We also briefly discussed Pauling's third, fourth, and fifth rules, the first two of which involve the sharing of edges and faces of polyhedra. The olivine (α-$(Mg_xFe_{1-x})_2SiO_4$) crystal structure was used to illustrate the distortions from hexagonal close packing of oxygens caused by metal-metal repulsion across shared polyhedron edges, as predicted by Pauling's third rule.

George et al. (2000) conclude from their statistical work that new empirical rules are needed to extend our understanding of crystal chemistry beyond the almost one-century old

Pauling's rules. We feel that this statement ignores the tremendous development of quantum mechanical methods and bond-valence theory that provides vastly increased understanding of the chemical composition, bond topology, crystal chemistry, stereochemistry, and behavior of crystals in dynamic processes. One area that has not kept pace with these advances is the treatment of inorganic structures, particularly minerals, in introductory chemistry and mineralogy text books. These text books tend to present Pauling's rules as our current understanding of inorganic structures and need to be brought up to date.

Among the many applications of BVT to Earth materials, we show how a priori bond-valence calculations can predict unstrained bond-lengths in crystal structures and how bond-valence mapping can locate low-Z ions (e.g., Li) in a crystal structure and examine possible diffusion paths for ions through crystal structures. BVT may also provide considerable insight into the chemical compositions and bond topologies of complicated minerals. Here we give an example involving uranyl oxide and oxysalt minerals, where we show that a detailed examination of the bond topology and valences of the constituent ions can provide a rationale for the chemical compositions of the weakly bonded parts of the structures (involving monovalent and divalent cations, OH, and H_2O groups), including reasonably accurate predictions for the amounts and coordination numbers of the cations and the amounts and coordination numbers of the H_2O groups.

Another important application of BVT discussed in this review is its use to locate the positions of H^+ ions in the crystal structures of hydrous minerals and nominally anhydrous minerals, particularly olivine (α-$(Mg_xFe_{1-x})_2SiO_4$) and its high-pressure polymorphs wadsleyite (β-$(Mg_xFe_{1-x})_2SiO_4$) and ringwoodite (γ-$(Mg_xFe_{1-x})_2SiO_4$), which are widely considered to be the most abundant minerals in Earth's mantle over the depth ranges 100-410 km, 410-525 km, and 525-660 km, respectively. Pauling bond strength sums were used to identify bond-valence

deficient oxygens in these nominally anhydrous minerals that could bond to protons and satisfy the valence-sum rule (Smyth, 1987, 1994). When the enormous volumes of these mantle minerals are considered, there is growing evidence that Earth's mantle could contain several ocean's worth of water in nominally anhydrous minerals such as olivine, wadsleyite, and ringwoodite. (e.g., Hirschmann et al., 2005; Smyth et al., 2003, 2006; Smyth and Jacobsen, 2006; Schmandt et al., 2014).

We have also discussed how BVT, in combination with synchrotron-based XAFS spectroscopy, can be used to constrain the compositions and molecular-level structures of aqueous oxyanions [e.g., selenate: $(^{[4]}Se^{6+}O_4)^{2-}$ and selenite $(^{[3]}Se^{4+}O_3)^{2-}$] and aqueous cations [e.g., $^{[3]}Pb^{2+}(H_2O)_3$ and $^{[6]}Co^{2+}(H_2O)_6$] sorbed at metal oxide-aqueous solution interfaces. In addition, BVT combined with crystal truncation rod X-ray diffraction studies can provide information on the composition, structure, and relative stabilities of different types of reactive functional groups on mineral surfaces in contact with aqueous solutions. The information resulting from the combination of synchrotron-based X-ray spectroscopy and scattering and BVT is particularly important because it is critical in understanding and predicting the sequestration/release, transport, bioavailability, and fate of common environmental contaminants in soils, surface waters, and groundwater. These developments helped spawn the field of molecular environmental science in the 1980's. The important role of protons in these types of sorption reactions cannot be determined by X-ray spectroscopy and scattering methods but can be evaluated using BVT.

A final application of BVT in this review is its use to constrain the local structural environments of high-valence, incompatible cations such as Zn^{4+}, Ti^{4+}, U^{4+}, U^{5+}, and U^{6+} in silicate glasses and melts in combination with XAFS spectroscopy. These studies show the importance of BVT in understanding why these and other high-valence cations are incompatible, i.e., they do not

partition readily from silicate melts to common silicate minerals during the crystallization of silicate magmas because high-valence cations cannot be stably accommodated in common silicate mineral structures.

Acknowledgments

The preparation of this review was stimulated by the recent paper of George et al. (2020), which evaluated the success of Pauling's five rules, both singly and in combination, in predicting stable atom and polyhedron arrangements in over 5,000 oxide-based crystal structures in the Inorganic Crystal Structure Data Base.

The Three Amigos, who have known each other professionally for the past 50+ years, decided to write this review with the hope that it might help students in a broad range of scientific disciplines, as well as their mentors, understand the major contribution made by Linus Pauling when he introduced his rules in 1929, and by David Brown, who introduced BVT in 1980. We were all fortunate to get to know both Linus Pauling and David Brown – the two stars of this review. GB wishes to thank his co-author and Ph.D. mentor (GVG) for introducing him to the principles of crystal chemistry, X-ray crystallography, and structural chemistry, as well as for his unfailing guidance and friendship over the past 55 years. GB also wishes to acknowledge Linus Pauling for writing "The Nature of the Chemical Bond and the Structure of Molecules and Crystals: An Introduction to Modern Structural Chemistry," first published in 1939. The 3rd Edition of this book, published in 1960, has had a major influence on our understanding of chemical bonding in Earth materials. In addition, GB wishes to thank his many excellent graduate students, postdocs, and faculty colleagues at Stanford over the past 47 years, particularly Dr. John Bargar (SLAC National Accelerator Laboratory), the late Dr. Steven Towle, Prof. Peggy O'Day (U.C. Merced), and the late Prof. George Parks (Stanford University) for the stimulating and fruitful

collaborations we had involving adsorption reactions of aqueous cations and oxyanions at mineral-aqueous solution interfaces. GB also thanks former postdoc Professor Francois Farges (Muséum National d'Histoire Naturelle, Paris) who was responsible for much of the work on our joint studies of the local structural environments of high-valence cations in aluminosilicate and titanosilicate glasses and melts. Finally, GB wishes to thank the U.S. National Science Foundation (Chemistry and Geosciences Directorates) and the U.S. Department of Energy, Basic Energy Sciences and Biological and Environmental Research for their generous support of his research program over the past 45 years and their support of the two main synchrotron light sources (the Stanford Synchrotron Radiation Lightsource at SLAC National Accelerator Laboratory and the Advanced Photon Source at Argonne National Laboratory) where most of GB's synchrotron-based studies of sorption complexes at mineral-water interfaces and his studies of structure-property relations in silicate glasses and melts were done. GVG owes a debt to the late Professor Richard Bader for tutoring him about the Feynman force exerted on the nuclei and the Ehrenfest force exerted on the electrons of the bonded atoms. Another of us (FCH) was a graduate student from 1968 to 1973 at McMaster University, working in the Materials Research Institute where he was exposed on a daily basis to David Brown, Bob Shannon, and other scientific luminaries at coffee breaks and lunch. The result was a friendship between a geologist, a physicist, and a chemist that has lasted until the present time, with innumerable emails concerning the physics and chemistry of chemical bonding and its influence on the properties and behavior of solids. FCH takes pleasure in acknowledging the enormous influence that David and Bob have had on his knowledge and understanding of crystals.

Finally, we wish to thank several anonymous reviewers as well as American Mineralogist Editor Prof. Don Baker for careful reviews of our manuscript.

References

Al-Abadleh, H.A., and Grassian, V.H. (2003a) Oxide surfaces as environmental interfaces. Surface Science Reports, 52(3-4), 63-161.

Al-Abadleh, H.A., and Grassian, V.H. (2003b) FT-IR study of water adsorption on aluminum oxide surfaces. Langmuir, 2, 341-347.

Aboud, S., Wilcox, J., and Brown, G.E., Jr. (2011) Density functional theory investigation of the interaction of water with α-Al_2O_3 and α-Fe_2O_3 (1-102) surfaces: Implications for surface reactivity. Physical Review B, 83(12), 125407(1-16).

Arai, Y., and Sparks, D.L. (2001) ATR-FTIR spectroscopic investigation on phosphate adsorption mechanisms at the ferrihydrite-water interface. Journal of Colloid & Interface Science, 241(2), 317-326.

Bader, R.F.W. (1990) Atoms in Molecules: A Quantum Theory, Oxford University Press: Oxford, U.K.

Bader, R.F.W. (2009) Bond paths are not chemical bonds. Journal of Physical Chemistry A, 113, 10391-10396.

Bandura, A.V., Sykes, D.G., Shapovalov, V., Troung, T.N., Kubicki, J.D., and Evarestov, R.]A. (2004) Adsorption of water on the TiO_2 (rutile) (110) surface: A comparison of periodic and embedded cluster calculations. Journal of Physical Chemistry A, 108(23), 7844-7853.

Bargar, J.R., Brown, G.E., Jr., and Parks, G.A. (1997a) Surface complexation of Pb(II) at oxide-water interfaces: I. XAFS and bond-valence determination of mononuclear and polynuclear Pb(II) sorption products on aluminum oxides. Geochimica et Cosmochimica Acta, 61, 2617-2637.

Bargar, J.R., Brown, G.E., Jr., and Parks, G.A. (1997b) Surface complexation of Pb(II) at oxide-water interfaces: II. XAFS and bond-valence determination of mononuclear Pb(II) sorption products and surface functional groups on iron oxides.. Geochimica et Cosmochimica Acta, 61, 2639-2652.

Bargar, J.R., Towle, S.N., Brown, G.E., Jr., and Parks, G.A. (1996) Outer-sphere lead(II) adsorbed at specific surface sites on single crystal α-alumina. Geochimica et Cosmochimica Acta, 60, 3541-3547.

Bargar, J.R., Towle, S.N., Brown, G.E., Jr., and Parks, G.A. (1997c) Structure, composition, and reactivity of Pb(II) and Co(II) sorption products and surface functional groups on single-crystal α-Al_2O_3. Journal of Colloid & Interface Science, 185, 473-493.

Barlow, W. (1883) Probable nature of the internal symmetry of crystals. Nature, 29, 186-188.

Barlow, W. (1894) Ueber die geometrischen Eigenschaften homogener starrer Structuren und ihre Anwendung auf Krystalle. Zeitschrift für Kristallographie, 23, 1.

Baur, W.H. (1981) In: Structure and Bonding in Crystals, Vol. II (Eds.: M. O'Keeffe, A., Navrotsky), Academic Press: London, Chapter 31.

Bedzyk, M.J., Bilderback, D., White, J., Abruna, H.D., and Bommarito, G.M. (1986) Probing electrochemical interfaces with X-ray standing waves. Journal of Physical Chemistry, 90, 4926-4928.

Bedzyk, M.J., Bommarito, G.M., Caffrey, M., and Penner, T.L. (1990) Diffuse double layer at a membrane-aqueous interface measured with X-ray standing waves. Science, 248, 52-56.

Bell, D.R., and Rossman, G.R. (1992) Water in the Earth's mantle: The role of nominally anhydrous minerals. Science, 255, 139l-1397.

Bickmore, B.R., Tadanier, C.J., Rosso, K.M., Monn, W.D., and Eggett, D.L. (2004) Bond-valence methods for pKa prediction: Critical reanalysis and a new approach. Geochimica et Cosmochimica Acta, 68, 2025-2042.

Bickmore, B.R., Rosso, K.M., Tadanier, C.J., Bylaska, E.J., and Doud, D. (2006) Bond-valence methods for pKa prediction: II. Bond-valence, electrostatic, molecular geometry, and solvation effects. Geochimica et Cosmochimica Acta, 70, 4057-4071.

Birle, J.D., Gibbs, G.V., Moore, P.B., and Smith, J.V. (1968) Crystal structures of natural olivines. American Mineralogist, 53, 807-824.

Bloch, A.N., and Schatteman, G.C. (1980) Quantum-defect orbital radii and the structural chemistry of simple solids. Structure and Bonding in Crystals, (Eds.: M. O'Keeffe and A. Navrotsky), Vol. 1, Academic Press, New York, pp. 49-72.

Bragg, W.H. (1912) X-rays and crystals. Nature, 90, 360-361.

Bragg, W.H. (1913) The reflection of X-rays by crystals. Proceedings of the Royal Society of London, 89A, 248-277.

Bragg, W.L. (1913a) The diffraction of short electromagnetic waves by a crystal. Proceedings of the Cambridge Philosophical Society, 17, 43-57.

Bragg, W.L. (1913b) The structure of some crystals as indicated by their diffraction of X-rays. Proceedings of the Royal Society of London, A89, 248.

Bragg, W.L. (1920) The arrangement of atoms in crystals. London, Edinburgh, and Dublin Philosophical Magazine and Journal of Science, 40, 169-189.

Bragg, W.L. (1937) Atomic Structure of Minerals. Cornell University Press, Ithaca, NY.

Bragg, W.H., and Bragg, W.L. (1913) The reflection of X-rays by crystals. Proceedings of the Royal Society of London, 88A, 428-438.

Brown, G.E., Jr. (1980) Crystal chemistry of the olivines and silicate spinels. Reviews in Mineralogy, 5, 275-381.

Brown, G.E,. Jr. (1990) Spectroscopic studies of chemisorption reaction mechanisms at oxide/water interfaces. Reviews in Mineralogy, 23, 309-363.

Brown, G.E., Jr. (2001) How minerals react with water. Science, 294, 67-69.

Brown, G.E., Jr., and Calas, G. (2012) Mineral-aqueous solution interfaces and their impact on the environment. Geochemical Perspectives, 1(4-5), 483-742.

Brown, G.E., Jr., and Parks, G.A. (2001) Sorption of trace elements from aqueous media: Modern perspectives from spectroscopic studies and comments on adsorption in the marine environment. International Geology Reviews, 43, 963-1073.

Brown, G.E., Jr., and Sturchio, N.C. (2002) An overview of synchrotron radiation applications to low temperature geochemistry and environmental science. Reviews in Mineralogy and Geochemistry, 49, 1-115.

Brown G.E., Jr., Farges, F., and Calas, G. (1995) X-ray scattering and x-ray spectroscopy studies of silicate melts. Reviews in Mineralogy, 32, 317-410.

Brown, G.E., Jr., Henrich, V.E., Casey, W.H., Clark, D.L., Eggleston, C., Felmy, A., Goodman, D.W., Grätzel, M., Maciel, G., McCarthy, M.I., Nealson, K., Sverjensky, D.A., Toney, M.F., and Zachara, J.M. (1999) Metal oxide surfaces and their interactions with aqueous solutions and microbial organisms. Chemical Reviews, 99, 77-174.

Brown, I.D. (1981) The bond-valence method: an empirical approach to chemical structure and bonding. in: Structure and Bonding in Crystals (Eds.: M. O'Keeffe and A. Navrotsky), Vol. II, Academic Press, New York, pp. 1–30.

Brown, I.D. (1988) What factors determine cation coordination number. Acta Crystallographica B, 44, 545-553.

Brown, I.D. (2002a) The Chemical Bond in Inorganic Chemistry. The Bond Valence Model. Oxford University Press, U.K.

Brown, I.D. (2002b) Topology and chemistry. Structural Chemistry, 13, 339-355.

Brown, I.D. (2009) Recent developments in the methods and applications of the bond valence model. Chemical Reviews, 109, 6858-6919.

Brown, I.D. (2016) The Chemical Bond in Inorganic Chemistry. The Bond Valence Model. 2nd Edition, Oxford University Press, U.K.

Brown, I.D., and Altermatt, D. (1985) Bond-valence parameters obtained from a systematic analysis of the Inorganic Crystal Structure Database. Acta Crystallographica B, 41, 244-247.

Brown, I.D., and Shannon, R.D. (1973) Empirical bond-strength--bond-length curves from oxides. Acta Crystallographica A, 29, 266-282.

Burdett, J.K., and Hawthorne, F.C. (1993) An orbital approach to the theory of bond valence. American Mineralogist, 78, 884-892.

Burdett, J.K., Price, G.D., and Price, S.L. (1981) Factors influencing solid-state structure – An analysis using pseudopotential radii structural maps. Physical Review B, 24(6), 2903-2912.

Cameron, M., Sueno, S., Prewitt, C.T., and Papike, J.J. (1973) High-temperature crystal chemistry of acmite, diopside, hedenbergite, jadeite, spodumene and ureyite. American Mineralogist, 58(7-8), 594-618.

Carabante, I., Grahn, M., Holmgren, A., and Hedlund, J. (2010) In situ ATR-FTIR studies on the competitive adsorption of arsenate and phosphate on ferrihydrite. Journal of Colloid & Interface Science, 351(2), 525-531.

Catti, M., Pavese, A., and Price, G.D. (1993) Quantum mechanical Hartree-Fock study of calcite ($CaCO_3$) at variable pressure, and comparison with magnesite ($MgCO_3$). Phys. Chem. Minerals, 20, 104-110.

Chelikowsky, J.R., and Phillips, J.C. (1977) Orbital model of thermochemical parameters. Physical Review Letters, 39, 1687.

Clark, J.R., Appleman, D.E., and Papike, J.J. (1969) Crystal-chemical characterization of clinopyroxenes based on eight new structure refinements. Mineralogical Society of America Special Paper, 2, 31-50.

Cohen, M.L. (1980) Pseudopotentials and crystal structure. In: Structure and Bonding in Crystals (Eds.: M. O'Keeffe and A. Navrotsky), Vol. I, Academic Press, New York, pp. 25-48.

Dalton, J. (1808) A New System of Chemical Philosophy. 15 Chapters, p. 1-587, R. Bickenstar, Strand, London.

Demartin, F., Diella, V., Gramaccioli, C.M., and Pezzotta, F. (2001) Schiavinatoite, $(Nb,Ta)BO_4$, the Nb analogue of behierite. European Journal of Mineralogy, 13, 159-165.

Eng, P.J., Trainor, T.P., Brown, G.E., Jr., Waychunas, G.A., Newville, M., Sutton, S.R., and Rivers, M.L. (2000) Structure of the hydrated α-Al_2O_3 (0001) surface. Science, 288, 1029-1033.

Farges, F., and Brown, G.E., Jr. (1996) An empirical model for the anharmonic analysis of high-temperature XAFS spectra of oxide compounds with applications to the coordination

environment of Ni in NiO, γ-Ni_2SiO_4, and Ni-bearing Na-disilicate glass and melt. Chemical Geology, 128, 93-106.

Farges, F., Ponader, C.W., and Brown, G.E., Jr. (1991) Structural environments of incompatible elements in silicate glass/melt systems: I. Zr at trace levels. Geochimica et Cosmochimica Acta, 55, 1563-1574.

Farges, F., Brown, G.E., Jr., Navrotsky, A., Gan, H., and Rehr, J.J. (1996a) Coordination chemistry of titanium(IV) in silicate glasses and melts. Part II. Glasses at ambient and pressure. Geochimica et Cosmochimica Acta, 60, 3039-3053.

Farges, F., Brown, G.E., Jr., Navrotsky, A., Gan, H., and Rehr, J.J. (1996b) Coordination chemistry of titanium(IV) in silicate glasses and melts. Part III. Glasses and melts from ambient to high temperatures. Geochimica et Cosmochimica Acta, 60, 3055-3065.

Farges, F., Ponader, C.W., Calas, G., and Brown, G.E., Jr. (1992) Structural environments of incompatible elements in silicate glass/melt systems: II. $U^{(IV)}$, $U^{(V)}$, and $U^{(VI)}$. Geochimica et Cosmochimica Acta, 56, 4205-4220.

Fenter, P.A. (2002) X-ray reflectivity as a probe of mineral-fluid interfaces: A user guide. Reviews in Mineralogy and Geochemistry, 49, 149-220.

Fenter, P.A., and Sturchio, N.C. (2004) Mineral-water interfacial structures revealed by synchrotron X-ray scattering. Progress in Surface Science, 77(5-8), 171-258.

Feynman, R.P. (1939) Forces in molecules. Physical Review, 56(4), 340–343.

Friedrich, W., Knipping, P., and von Laue, M. (1912) Interferenz-Erscheinungen bei Röntgenstrahlen. Sitzungsberichte der mathematisch-physikalischen Classe. K. B. Akademie der Wissenschaften zu Munchen, 42, 303–322

Gagné, O.C., and Hawthorne, F.C. (2015) Comprehensive derivation of bond-valence parameters for ion pairs involving oxygen. Acta Crystallographica B, 71, 562–578.

Gagné, O.C., and Hawthorne, F.C. (2017) Empirical Lewis-acid strengths for 135 cations bonded to oxygen. Acta Crystallographica B, 73, 956-961.

Gagné, O.C., and Hawthorne, F.C. (2018) Bond-length distributions for ions bonded to oxygen: Results for the non-metals and discussion of lone-pair stereoactivity and the polymerization of PO_4. Acta Crystallographica B, 74, 79-96.

Gagné, O.C., and Hawthorne, F.C. (2020) Bond-length distributions for ions bonded to oxygen: Results for the transition metals and quantification of the factors underlying bond-length variation in inorganic solids. International Union of Crystallography Journal, 7, 581-629.

Gagné, O.C., Mercier, P.H.J., and Hawthorne, F.C. (2017) A priori bond-valence and bond-length calculations in rock-forming minerals. Acta Crystallographica B, 74, 470-482.

Gatti, C. (2005) Chemical bonding in crystals: new directions. *Z. Kristallogr.* **220**, 399-457.

George, J., Waroquiers, D., Stefano, D., Petretto, G., Rignanese, G-M., and Hautier, G. (2020) The limited predictive power of the Pauling Rules. Angewandte Chemie International Edition, 132, 7639-7645.

Ghose, S.K. Waychunas, G.A., Trainor, T., and Eng, P.J. (2010) Hydrated goethite (alpha-FeOOH) (100) interface structure: Ordered water and surface functional groups. Geochimica et Cosmochimica Acta, 74, 1943-1953.

Gibbs, G.V. (1982) Molecules as models for bonding in silicates. American Mineralogist, 67, 421-450.

Gibbs, G.V., and Smith, J.V. (1965) Refinement of the crystal structure of synthetic pyrope, American Mineralogist, 50, 2023-2039.

Gibbs, G.V., Finger, L.W., and Boisen, M.B. Jr. (1987) Molecular mimicry of the bond length-bond strength variations in oxide crystals. Physics and Chemistry of Minerals, 14, 327-331.

Gibbs, G.V., Ross, N.L., and Cox, D.F. (2015) Bond length estimates for oxide crystals with a molecular power law expression. Physics and Chemistry of Minerals, 42, 587-593.

Gibbs, G.V., Spackman, M.A., and Boisen, M.B. Jr. (1992) Bonded and promolecule radii for molecules and crystals. American Mineralogist, 7(7-8), 741-750.

Gibbs, G.V., Boisen, M.B., Jr., Beverly, L.L., and Rosso, K.M. (2001) A computational quantum chemical study of the bonded interactions in earth materials and structurally and chemically related molecules. Reviews in Mineralogy, 42, 345-381.

Gibbs, G.V., Ross, N.L., Cox, D.F., and Rosso, K.M. (2014) Insights into the crystal chemistry of Earth materials rendered by electron density distributions: Pauling's rules revisited. American Mineralogist, 99, 1071-108

Gibbs, G.V., Cox, D.F., Boisen, M.B., Jr., Downs, R.T., and Ross, N.L. (2003) The electron localization function: a tool for locating favorable proton docking sites in the silica polymorphs. Physics and Chemistry of Minerals, 30, 305-316.

Gibbs, G.V., Rosso, K.M., Teter, D.M., Boisen, M.B., Jr., and Bukowinski, M.S.T. (1999) Model structures and properties of the electron density distribution for low quartz at pressure: a study of the Si-O bond. Journal of Molecular Structure, 485, 13-25.

Gibbs, G.V., Ross, N.L., Cox, D.F., Rosso, K.M., Iverson, B.B., and Spackman, M.A. (2013a) Bonded radii and the contraction of the electron density of the oxygen atom by bonded interactions. Journal of Physical Chemistry A, 117, 1632-1640.

Gibbs, G.V., Ross, N.L., Cox, D.F., Rosso, K.M., Iverson, B.B., and Spackman, M.A. (2013b) Pauling bond strength, bond length and electron density distribution. Physics and Chemistry of Minerals, 41, 17-25.

Gibbs, G.V., Wallace, A.F., Cox, D.F., Downs, R.T., Ross, N.L., and Rosso, K.M. (2009) Bonded interactions in silica polymorphs, silicates, and siloxane molecules, American Mineralogist, 94, 1085-1102.

Gibbs, G.V. Wang, D., Hin, C., Ross, N.L., Cox, D.F., Spackman, M.A., and Angel, R.J. (2012) Properties of atoms under pressure: Bonded interactions of the atoms in three perovskites. Journal of Chemical Physics, 137, 164313 (1-12).

Gibbs, G.V., Downs, R.T., Cox, D.F., Ross, N.L., Prewitt, C.T., Rosso, K.M. Lippmann, T., and Kirfel, A. (2008) Bonded interactions and the crystal chemistry of minerals: a review. Zeitschrift für Kristallographie, 223, 1-40.

Gilbert, B., Erbs, J.J., Penn, R.L., Petkov, V., Spagnoli, D., and Waychunas, G.A. (2013) A disordered nanoparticle model for 6-line ferrihydrite. American Mineralogist, 98, 1465-1476.

Goldschmidt, V.M. (1926) Die gesetze der krystallochemie. Naturwissenschaften, 14(21), 477-485.

Hawthorne, F.C. (1983) Graphical enumeration of polyhedral clusters. Acta Crystallographica A, 39, 724-736.

Hawthorne, F.C. (1992) The role of OH and H_2O in oxide and oxysalt minerals. Zeitschrift für Kristallographie, 201, 183-206.

Hawthorne, F.C. (2006) Landmark Papers: Structure Topology. Mineralogical Society of Great Britain & Ireland, London.

Hawthorne, F.C. (2012) A bond-topological approach to theoretical mineralogy: crystal structure, chemical composition and chemical reactions. Physics and Chemistry of Minerals, 39, 841-874.

Hawthorne, F.C. (2015) Toward theoretical mineralogy: a bond-topological approach. American Mineralogist, 100, 696-713.

Hawthorne, F.C. (2018) A bond-topological approach to borate minerals: A brief review. Physics and Chemistry of Glasses (Part B), 59, 121-129.

Hawthorne, F.C., and Herwig, S. (2020) A structure hierarchy for the aluminofluoride minerals. Canadian Mineralogist, 58 (in press).

Hawthorne, F.C., and Schindler, M. (2008) Understanding the weakly bonded constituents in oxysalt minerals. Zeitschrift für Kristallographie, 223, 41-68.

Hawthorne, F.C., and Schindler, M. (2014) Crystallization and dissolution in aqueous solution: A bond-valence approach. In: Structure and Bonding. Bond Valences (Eds.: I. D. Brown and K. R. Poeppelmeier), Springer, Heidelberg, Germany, 161-190.

Hawthorne, F.C., Oberti, R., Harlow, G.E., Maresch, W.V., Martin, R.F., Schumacher, J.C., and Welch, M.D. (2012) Nomenclature of the amphibole supergroup. American Mineralogist, 97, 2031-2048.

Hayes, K.F., Roe, A.L., Brown, G.E., Jr., Hodgson, K.O., Leckie, J.O., and Parks, G.A. (1987) In-situ X-ray absorption study of surface complexes at oxide/water interfaces: selenium oxyanions on α-FeOOH. Science, 238, 783-786.

Hiemstra, T.P., Venema, P., and Van Riemsdijk, W.H. (1996) Intrinsic proton affinity of reactive surface groups of metal (hydr)oxides: The bond-valence principle. Journal of Colloid & Interface Science, 184, 680-692.

Hirschmann, M.M., Abaud, C., and Withers, A.C. (2005) Storage capacity of H_2O in nominally anhydrous minerals in the upper mantle. Earth and Planetary Science Letters, 236, 167-181.

Hohenberg, P., and Kohn, W. (1964) Inhomogeneous electron gas. Physical Review B, 136, 864–871.

Horiuchi, H., and Sawamoto, H. (1981) β-Mg_2SiO_4: Single crystal diffraction study. American Mineralogist, 66(5-6), 568-575.

Huang, X.G., Xu, Y.S., and Karato, S.I. (2005) Water content in the transition zone from electrical conductivity of wadsleyite and ringwoodite. Nature, 434, 746-749.

Hüttig, G.F. (1920) Notiz zur Geometrie der Koordinationszahl. Zeitschrift für anorganische und allgemeine Chemie, 114, 24-26.

Ito, E., and Katsura, T. (1989) A temperature profile of the mantle transition zone. Geophysical Research Letters, 16(5), 425-428.

Johnson, S.B., Brown, G.E., Jr., Healy, T.W., and Scales, P.J. (2005) Adsorption of organic matter at mineral/water interfaces: 6. Effect of inner-sphere vs. outer-sphere adsorption on colloidal stability. Langmuir, 21(14), 6356-6365.

Kirfel, A., Lippmann, T., Blaha, P., Schwarz, K., Cox, D.F., Rosso, K.M., and Gibbs, G.V. (2005) Electron density distribution and bond critical point properties for forsterite, Mg2SiO4, determined with synchrotron single crystal X-ray diffraction data. Physics and Chemistry of Minerals, 32, 301-313.

Kohlstedt, D.L., Keppler, H., and Rubie, D.C. (1996) Solubility of water in the α, β and γ phases of $(Mg,Fe)_2SiO_4$. Contributions to Mineralogy and Petrology, 123, 345-357.

Kohn, W., and Sham, L. J. (1965) Self-consistent equations including exchange and correlation effects. Physical Reviews A, 140, 1133–1138.

Kumagai, N., Yu, A., and West, K. (1997) $Li_{1-x}Na_xV_3O_8$ as positive materials for secondary lithium batteries. Journal of Applied Electrochemistry, 27, 953-958.

Kunitz, W. (1930) Die Isomorphieverhoiltnisse in der Hornblende-gruppe. Neues Jahrbuch. Mineralogie Abh., 60, 171-250.

Landé, C. A. (1920) Uber die Grösse der Atome. Zeitschrift für Physics, 1, 191–197.

Li, Y-P., and Burns, P.C. (2000) Investigations of crystal-chemical variability in lead uranyl oxide hydrates. I. Curite. Canadian Mineralogist, 38, 727-735.

Liu, P., Kendelewicz, T., Brown, G.E., Jr., Nelson, E.J., and Chambers, S.A. (1998) Reaction of water with α-Al_2O_3 and α-Fe_2O_3 (0001) surfaces: synchrotron x-ray photoemission studies and thermodynamic calculations. Surface Science, 417, 53-65.

Mason, S. E., Trainor, T.P., and Chaka, A.M. (2011) Hybridization-reactivity relationship in Pb(II) adsorption on α-Al_2O_3-water interfaces: A DFT study. Journal of Physical Chemistry C, 115, 4008-4021.

Mason, S.E., Iceman, C.R., Trainor, T.P., and Chaka, A.M. (2010) Density functional theory study of clean, hydrated, and defective alumina (1-102). Physical Review B, 81, 125423 (1-12).

Mason, S.E., Iceman, C.R., Tanwar, K.S., Trainor, T.P., and Chaka, A.M. (2009) Pb(II) adsorption on isostructural hydrated alumina and hematite (0001) surfaces: A DFT study. Journal of Physical Chemistry C, 113, 2159-2170.

Mozzi, R.L., and Warren, B.E. (1969) The structure of vitreous silica. Journal of Applied Crystallography, 2(4), 164-172.

Mrose, M.E., and Rose, H.J. (1962) Behierite, (Ta,Nb)BO_4, a new mineral from Manjaka, Madagascar. Angewandte Chemie, 235.

Nemsak, S., Shavorskiy, A., Karslioglu, O., Zegkinoglou, I., Rattanachata, A., Conlon, C.S., Keqi, A., Greene, P.K., Burks, E.C., Salmassi, F., Gullikson, E.M., Yang, S-H., Liu, K., Bluhm, H., Fadley, C.S. (2014) Concentration and chemical-state profiles at heterogeneous interfaces with sub-nm accuracy from standing-wave ambient-pressure photoemission. Nature Communications 5, 5441 (7 pages).

Newberg, J.T., Starr, D.E., Yamamoto, S., Kaya, S., Kendelewicz, T., Mysak, E., Posgaard, S., Salmeron, M.B., Brown, G.E., Jr., Nilsson, A., and Bluhm, H. (2011) Autocatalytic surface hydrolyxation of MgO(100) terrace sites observed under ambient conditions. Journal of Physical Chemistry C, 115(26), 12864-12872.

Novak, G.A., and Gibbs, G.V. (1971) The crystal chemistry of the silicate garnets. American Mineralogist, 56, 791-825.

Novak, P., Scheifele, W., Joho, F., and Haas, O. (1995) Electrochemical insertion of magnesium into hydrated vanadium bronzes. Journal of the Electrochemical Society, 142, 2544-2550.

Ohtani, E., Litasov, K., Hosoya, T., Kubo, T., and Kondo, T. (2004), Water transport into the deep mantle and formation of a hydrous transition zone. Physics of Earth and Planetary Interiors, 143-144, 255-269.

Ohtani, E. (2021) Hydration and Dehydration in Earth's Interior. Annual Review of Earth and Planetary Sciences, 49, 253-278.

Panero, W.R., Smyth, J.R., Pigott, J.S., Liu, Z.X., and Frost, D.J. (2013) Hydrous ringwoodite to 5 K and 35 GPa: Multiple hydrogen bonding sites resolved with FTIR spectroscopy. American Mineralogist, 98(4), 637-642.

Parks, G.A. (1965) The isoelectric points of solid oxides, solid hydroxides, and aqueous hydroxo complex systems. Chemical Reviews, 65, 177–198.

Parks, G.A. (1967) Aqueous surface chemistry of oxides and complex oxide minerals. Isoelectronic point and zero point of charge, In: Equilibrium Concepts in Natural Water Systems: Advances in Chemistry Series (Ed.: R. F. Gould), 67, 121-160.

Pauling, L. (1927) Sizes of ions and structure of ionic crystals. Journal of the American Chemical Society, 49, 765-792.

Pauling, L. (1929) The principles determining the structure of complex ionic crystals. Journal of the American Chemical Society, 51, 1010-1026.

Pauling, L. (1960) The Nature of the Chemical Bond and the Structure of Molecules and Crystals: An Introduction to Modern Structural Chemistry. 3rd Ed., Cornell University Press, Ithaca, NY, 644 p.

Pauling, L., and Hendricks, S.B. (1925) The crystal structures of hematite and corundum. Journal of the American Chemical Society, 47(3), 781-790.

Pendás, A.M., and Hernández-Trujillo, J. (2012) The Ehrenfest force field: Topology and consequences for the definition of an atom in a molecule. Journal of Chemical Physics, 137, 134101(1-9).

de Picciotto, L.A., Adendorff, K.T., Liles, D.C., and Thackeray, M.M. (1993) Structural characterization of $Li_{1+x}V_3O_8$ insertion electrodes by single-crystal X-ray diffraction. Solid State Ionics, 62, 297-307.

Pickering, I.J., Brown, G.E., Jr., and Tokunaga, T.K. (1995) X-ray absorption spectroscopy of selenium transformations in Kesterson Reservoir soils. Environmental Science & Technology, 29, 2456-2459.

Preiser, C., Lösel, J., Brown, I.D., Kunz, M., and Skowron, A. (1999) Long range Coulomb forces and localized bonds. Acta Crystallographica B, 55, 698-711.

Prencipe, M. (2019) Quantum mechanics in Earth sciences: a one-century-old story. Rendiconti Lincei. Scienze Fisiche e Naturali 30, 239-259.

Purevjav, N., Okuchi, T., Tomioka, N., Abe, J., and Harjo, S. (2014) Hydrogen site analysis of hydrous ringwoodite in mantle transition zone by pulsed neutron diffraction. Geophysical Research Letters, 41, 6718-6724.

Purevjav, N., Okuchi, T., Wang, X., Hoffman, C., and Tomioka, N. (2018) Determination of hydrogen site and occupancy in hydrous Mg_2SiO_4 spinel by single-crystal neutron diffraction. Acta Crystallographica B, 74, 115-120.

Runtz, G.R., Bader, R.F.T., and Messer, R.R. (1977) Definition of bond paths and bond directions in terms of the molecular charge distribution. Canadian Journal of Chemistry, 55, 3040-3045.

Sayers, D.E., Stern, E.A., Lytle, F.W. (1971) New technique for investigating noncrystalline structures – Fourier analysis of extended X-ray absorption fine structure. Physical Review Letters, 27(18), 1204-1207.

Schindler, M., and Hawthorne, F.C. (2001a) A bond-valence approach to the structure, chemistry and paragenesis of hydroxy-hydrated oxysalt minerals: I. Theory. Canadian Mineralogist, 39, 1225-1242

Schindler, M., and Hawthorne, F.C. (2001b) A bond-valence approach to the structure, chemistry and paragenesis of hydroxy-hydrated oxysalt minerals: II. Crystal structure and chemical composition of borate minerals. Canadian Mineralogist, 39, 1243-1256.

Schindler, M., and Hawthorne, F.C. (2001c) A bond-valence approach to the structure, chemistry and paragenesis of hydroxy-hydrated oxysalt minerals: III. Paragenesis of borate minerals. Canadian Mineralogist, 39, 1257-1274.

Schindler, M., and Hawthorne, F.C. (2004) A bond-valence approach to the uranyl-oxide hydroxy-hydrate minerals: Chemical composition and occurrence. Canadian Mineralogist, 42, 1601-1627.

Schindler, M., Huminicki, D.M.C., and Hawthorne, F.C. (2006b) Sulfate minerals: I. Bond topology and chemical composition. Canadian Mineralogist, 44, 1403-1429.

Schindler, P.W., Wälti, E., and Furst, B. (1976b) The role of surface-hydroxyl groups in the surface chemistry of metal oxides. Chimia, 30, 107-109.

Schindler, M., Mutter, A., Hawthorne, F.C., and Putnis, A. (2004a) Prediction of crystal morphology of complex uranyl-sheet minerals. I. Theory. Canadian Mineralogist, 42, 1629-1649.

Schindler, M., Mutter, A., Hawthorne, F.C., and Putnis, A. (2004b) Prediction of crystal morphology of complex uranyl-sheet minerals. II. Observation. Canadian Mineralogist, 42, 1651-1666.

Schindler, P.W., Furst, B., Dick, R., and Wolf, P.U. (1976a) Ligand properties of silanol groups. 1. Surface complex-formation with Fe^{3+}, Cu^{2+}, Cd^{2+} and Pb^{2+}. Journal of Colloid & Interface Science, 55(2), 469-475.

Schindler, M., Hawthorne, F.C., Alexander, M.A., Kutluoglu, R.A., Mandaliev, P., Halden, N.M., and Mitchell, R.M. (2006a) Na-Li-$[V_3O_8]$ insertion electrodes: Structures and diffusion pathways. Journal of Solid-State Chemistry, 179, 2616-2628.

Schmandt, B., Jacobsen, S.D., Becker, T.W., Liu, Z., and Dueker, K.G. (2014) Dehydration melting at the top of the lower mantle. Nature, 344, 1265-1268.

Shannon, R.D. (1976) Revised effective ionic radii and systematic studies of interatomic distances in halides and chalcogenides. Acta Crystallographica A, 32, 751-767.

Shannon, R.D., and Prewitt, C.T. (1969) Effective ionic radii in oxides and fluorides. Acta Crystallographica B, 25, 925-946.

Simons, G., and Bloch, A.N. (1973) Pauli-force model potential for solids. Physical Review B, 7(6), 2754-2761.

Skinner, A.J., LaFemina, J.P., and Jensen, H.J.F. (1994) Structure and bonding of calcite: A theoretical study. American Mineralogist, 79, 205-214.

Slater, J.C. (1964) Atomic radii in crystals. Journal of Chemical Physics, 41, 3199−3204.

Smyth, J.R. (1987) β-Mg_2SiO_4: A potential host for water in Earth's mantle? American Mineralogist, 72, 1051-1055.

Smyth, J.R. (1994) A model for hydrous wadsleyite (β-Mg_2SiO_4): An ocean in the Earth's interior? American Mineralogist, 79, 1021-1024.

Smyth, J.R., and Jacobsen, S.D. (2006) Nominally anhydrous minerals and Earth's deep-water cycle. In: Earth's Deep-Water Cycle (Eds.: S. D. Jacobsen and S. Van Der Lee), Vol. 320, pp. 1-11. American Geophysical Union, Washington, D.C.

Smyth, J.R., Frost, D.J., Nestola, F., Holl, C.M., and Bromiley, G. (2006) Olivine hydration in the deep upper mantle: Effects of temperature and silica activity. Geophysical Research Letters, 33(15), L15301(1-5).

Smyth, J.R., Holl, C.M., Frost, D.J., Jacobsen, S.D., Langenhorst, F., and McCammon, C.A. (2003) Structural systematics of hydrous ringwoodite and water in Earth's interior. American Mineralogist., 88(10), 1402-1407.

Smyth, J.R., Kawamoto, T., Jacobsen, S.D., Swope, R.J., Hervig, R.L., and Holloway, J.R. (1997) Crystal structure of monoclinic hydrous wadsleyite [β-$(Mg_xFe_{1-x})_2SiO_4$]. American Mineralogist, 82, 270-275.

Stumm, W. (1992) Chemistry of the Solid-Water Interface: Processes at the Mineral-Water and Particle-Water Interfaces in Natural Systems. Wiley Interscience, New York, 428 p.

Stumm, W., Huang, C.P., and Jenkins, S.R. (1970) Specific chemical interaction affecting the stability of dispersed systems. Croatica Chemica Acta, 42, 223-245.

Stumm, W., Wehrli, B., and Wieland, E. (1987) Surface complexation and its impact on geochemical kinetics. Croatica Chemica Acta, 60, 429-438.

Sverjensky, D.A. (1994) Zero-point-of-charge prediction from crystal chemistry and solvation theory. Geochimica et Cosmochimica Acta, 58, 3123-3129.

Tait, K.T., Ercit, T.S., Abdu, Y.A., Černý, P., and Hawthorne, F.C. (2011) The crystal structure and crystal chemistry of manitobaite, ideally $(Na_{16}\square)$ $Mn^{2+}_{25}Al_8(PO_4)_{30}$, from Cross Lake, Manitoba. The Canadian Mineralogist 49(5), 1221-1242.

Taylor, M., and Brown, G.E., Jr. (1979) Structure of mineral glasses I: The feldspar glasses $NaAlSi_3O_8$, $KAlSi_3O_8$, $CaAl_2Si_2O_8$. Geochimica et Cosmochimica Acta, 43, 61-75.

Thomas, S.-M., Jacobsen, S.D., Bina, C.R., Reichart, P., Moser, M., Haun, E.H., Koch-Müller, M., Smyth, J.R., and Dollinger, G. (2015) Quantification of water in hydrous ringwoodite. Frontiers in Earth Science, 2, Article 38(10).

Thompson, A.B. (1992) Water in the Earth's upper mantle. Nature, 358, 295-307.

Towle, S.N., Bargar, J.R., Brown, G.E., Jr., and Parks, G.A. (1999) Sorption of Co(II) on metal oxide surfaces: II. Identification of Co(II)(aq) adsorption sites on (1-102) and (0001) surfaces of α-Al_2O_3 by grazing-incidence XAFS spectroscopy. Journal of Colloid & Interface Science, 217, 312-321.

Trainor, T.P., Eng, P.J., Brown, G.E., Jr., Robinson, I.K., and De Santis, M. (2002) Crystal truncation rod diffraction study of the clean and hydrated α-Al_2O_3 (1-102) surface. Surface Science, 496, 238-250.

Trainor, T.P., Chaka, A.M., Eng, P.J., Newville, M., Waychunas, G.A., Catalano, J.G., Brown, G.E., Jr. (2004) Structure and reactivity of the hydrated hematite (0001) surface. Surface Science, 573(2), 204-224.

Usher, C.R., Michel, A.E., and Grassian, V.H. (2003) Reactions on mineral dust. Chemical Reviews, 103(12), 4883-4939.

Waltersson, K. (1978) A method, based upon 'bond strength' calculations, for finding probable lithium sites in crystal structures. Acta Crystallographica A, 34, 901-905.

Wang, H., Lu, R., Downs, R.T., and Costin, G. (2006) Goethite, α-FeO(OH), from single crystal data. Acta Crystallographica E - Crystallographic Communications, 62(12), i250-i252.

Warren, B.E. (1929) The structure of tremolite $H_2Ca_2Mg_5(SiO_3)_8$. Zeitschrift für Kristallographie, 72, 42-57.

Wasastjerna, J.A. (1923) Radii of ions. Societas Scientiarum Fennica Communication Physics and Mathematics, 38, 1-25.

Watson, E.B. (1979) Zircon saturation in felsic liquids: Experimental results and applications to trace element geochemistry. Contributions to Mineralogy and Petrology, 70, 407-419.

Wilson, R.J. (1979) Introduction to Graph Theory. Longman, London.

Winter, J.K., and Ghose, S. (1979) Thermal expansion and high-temperature crystal chemistry of the Al_2SiO_5 polymorphs. American Mineralogist, 64, 573-586.

Yamamoto, S., Kendelewicz, T., Newberg, J.T., Ketteler, G., Starr, D.E., Mysak, E.R., Andersson, K., Ogasawara, H., Bluhm, H., Salmeron, M., Brown, G.E,. Jr., and Nilsson, A. (2010) Water adsorption on α-Fe_2O_3(0001) at near ambient conditions. Journal of Physical Chemistry C, 114, 2256-2266.

Yoon, T.H., Johnson, S.B., Musgrave, C.B., and Brown, G.E., Jr. (2004) Adsorption of organic matter at mineral/water interfaces: I. ATR-FTIR spectroscopic and quantum chemical study of oxalate adsorbed at boehmite/water and corundum/water interfaces. Geochimica et Cosmochimica Acta, 68, 4505-4518.

Zachariasen, W.H. (1954) Crystal chemical studies of the 5f-series of elements. XXIII. On the crystal chemistry of uranyl compounds and of related compounds of transuranic elements. Acta Crystallographica, 7, 795-799.

Zemann, J. (1986) The shortest known interpolyhedral O-O distance in a silicate. Zeitschrift für Kristallographie, 175, 299-303.

Zunger, A. (1980) Systematization of the stable crystal structure of all AB-type binary compounds: A pseudopotential orbital radii approach. Physical Review B, 22, 5839.

Zunger, A., and Cohen, M.L. (1978) Density-functional pseudopotential approach to crystal phase stability and electronic structure. Physical Review B, 18(10-15), 5449.

Figure 1: Level-line contour map of the electron density distribution for the coesite structure generated in a plane containing the nuclei of the atoms comprising the Si(1)−O(5)−Si(2) angle. The contour interval is 0.0625, 0.125, 0.250, ... e/Å^3. The circle centered at the nucleus of O(5), labeled **B&S** (Bragg, 1920; Slater, 1964) defines the outermost limits of the atomic radius (0.60 Å) for the O atom, the one labeled **S&P** (Shannon and Prewitt, 1969) defines the 1.25 Å outermost crystal radius for the oxide anion, and the one labeled **G** defines the Goldschmidt (1926) 1.32 Å

outermost limit of the ionic radius for the oxide anion (from Gibbs et al., 2013a). Permission has been granted by the American Chemical Society to re-use Figure 1 in Gibbs et al. (2013a).

Figure 2(a): Map of structure types for 99 AB compounds as a function of cation (r+) and anion (r-) radii. **Figure 2(b):** Map of structure types of the same AB compounds as a function of s and p orbital radii (r^A_σ and r^B_σ). The solid lines indicate the boundaries between structure types predicted by the radius ratio for [4]- and [6]-coordination and the dashed lines are drawn between the CsCl and halite structures and between the halite structures and the sphalerite and wurtzite structures (after Burdett et al., 1981).

Figure 3(a): Variation in range of coordination number as a function of Lewis acidity for 135 cations; the broken red lines denote the maximum extent of data according to Pauling's radius-ratio rule. **Figure 3b:** Variation in mean coordination number as a function of Lewis acidity for 135 cations; the broken black lines denote the maximum extent of data according to the radius-ratio values of Pauling (1960).

Figure 4(a): Correlations of average cation (M)-oxygen (O) distance (in Å) predicted from the sum of Shannon and Prewitt (1969) radii values for first- and second-row atoms with Pauling bond strength (s). **Figure 4(b)**: The same correlations after dividing the bond strength by the row number (r) of the M metal atom in the periodic table (from Gibbs et al., 2008). Permission has been granted by Walter de Gruyter GmbH 2021 to re-use of Figure 1 in Gibbs et al. (2008).

Figure 5: A scatter diagram of the individual Shannon (1976) bond lengths, $R(M–O)^{Shan} = r_c(M) + 1.24$ in Å where $r_c(M)$ are the crystal radii for the cations given in Shannon's (1976) Table 1 and 1.24 Å is the radius assumed for the oxide anion plotted in terms of bond lengths generated with the molecular-based power law expression $R(M–O)^{Mol} = 1.39(s/r)^{-0.22}$ (in Å). The solid line is the regression line $R(M–O)^{Shan} = 0.91R(M–O)^{Mole} + 0.18$ bounded by dashed line 95% confidence limits that define where future observation may be expected to fall (from Gibbs et al., 2015). Reprinted by permission from Springer Nature: Nature/Springer/Palgrave, Physics and Chemistry of Minerals, Bond length estimates for oxide crystals with a molecular power law expression; Gibbs, G.V., Ross, N.L., and Cox, D.F. (2015).

Figure 6(a): A scatter diagram of R(M-O) Å plotted in terms of the value of the electron density at the bond critical point, $\rho(r_c)$, for periodic table second row, r = 2, Al-O bonded interactions, periodic table third row, r = 3, Ca-O bonded interactions, periodic table fourth row, r = 4, Sn-O and Y-O bonded interactions, and periodic table fifth row, r = 5, La-O bonded interactions.

Figure 6(b): The bond length data displayed in (a) is plotted in terms of $\rho(r_c)/r$. A regression analysis of R(M-O) vs. $\rho(r_c)/r$ data for the perovskites resulted in the power law expression $R(M-O) = 1.41(\rho(r_c)/r)^{-0.21}$ (graphed as a solid line). A regression analysis of the optimized M-O bond lengths calculated for the oxide molecules resulted in the expression, $R(M-O) = 1.39(s/r)^{-0.22}$ (graphed as a dashed line). It is noteworthy that both $\rho(r_c)/r$ and s/r plot along the same axis in the figure both as a function of R(M-O) (from Gibbs et al., 2012).

Figure 7: Averaged experimental M-O bond lengths, <R(M-O)> Å, plotted in terms of the averaged value of the electron density, $<\rho(r_c)>/r$, Å^3, accumulated at the bond critical point, r_c,

between bonded pairs of M and O atoms for five rows of atoms of the periodic table. The open circle data are procrystal data calculated for first- and second-row bonded atoms (from Gibbs et al., 2014).

Figure 8: Polyhedron drawings of **(a)** the idealized hexagonal close-packed (hcp) structure of forsterite and **(b)** the actual structure of forsterite, illustrating the distortion from hcp resulting from cation-cation repulsion across shared edges of the $M(1)O_6$ and $M(2)O_6$ octahedra and the SiO_4 tetrahedron (after Brown, 1980).

Figure 9: (a) Perspective view of a portion of the olivine crystal structure illustrating oxygen bonded to M(1), M(2), and Si. **(b)** Portions of the distorted cube shown in the center of the figure to the left, flattened to illustrate angular distortions from ideal hexagonal close-packing geometry (after Brown, 1980).

Figure 10: Planar projections of the unique M-O-M-O and M-O-Si-O faces of the distorted cube of nearest-neighbor cations and oxygens in forsterite ($(Mg_{0.90}Fe_{0.10})_2SiO_4$), showing "bond-angle strain" values (in degrees), (i.e., the difference between bond angles of the perfect hexagonal close-packed olivine structure and the actual forsterite structure) and bond distances (in Å). Cell parameters and atomic coordinates of atoms in the asymmetric unit of the forsterite structure were used to calculate interatomic distances and angles are from Birle et al. (1968).

Figure 11: Bond length vs. bond strength curve for U-O and U-F bonds in a series of uranyl compounds (after Zachariasen, 1954). Reproduced with permission of the International Union of Crystallography.

Figure 12. The structure of $Na_{0.7}Li_{0.7}[V_3O_8]$ viewed down [010]; M(1): red circles; M(2): green circles; M(3): yellow circles; Black lines show the proposed paths of diffusion (modified from Schindler et al., 2008).

Figure 13. Bond-valence maps for Li^+ in $Na_{0.7}Li_{0.7}[V_3O_8]$ in the ac-plane at y = 0.25 and containing 15 contour levels with an interval of 0.30 vu; **(a)** calculated using information on V^{5+}, the contour line representing the bond-valence sum of 1.0 v.u. is marked with a thick black line; **(b)** calculated without V^{5+}; M(1): red circles; M(2): green circles; M(3): yellow circles; black lines show the proposed paths of diffusion; **(c)** cross sections of the narrow paths joining adjacent channels showing the variation in bond-valence sums for Li^+ and Na^+ (modified from Schindler et al., 2006a).

Figure 14. (a) Bond-valence map for Li^+ in $Li[V_3O_8]$ in the ac-plane at y = 0.25 and containing 15 contour levels with an interval of 0.07 v.u., **(b)** calculated without any information on V^{5+}; the first contour line denotes a bond-valence sum of 0.9 v.u. and the 1.0 v.u. contour line is marked by a thick black line; **(c)** cross sections of the narrow paths joining adjacent channels showing the variation in bond-valence sums for Li^+ and Na^+ (modified from Schindler et al., 2006a).

Figure 15: The bond-valence structure around (H_2O) as a function of local bond-topology; (**a**) a cation, C (green) bonded to an anion, S (yellow) with bond valence v v.u.; (**b**) a cation bonded to an (H_2O) group (O = orange; H = black) with bond valence v v.u.; the H atoms hydrogen-bond to

the anions S with bond valence v/2 v.u. per bond; (**c**) two cations bonded to an (H_2O) group with bond valence v.u. per bond; the H atoms hydrogen-bond to the anions S with bond valence **v** v.u. per bond; (**d**) two H atoms hydrogen-bonded to an (H_2O) group with bond valence v v.u. per bond; the H atoms of the (H_2O) group hydrogen-bond to the anions S with bond valence v v.u. per bond.

Figure 16: (a) Correlation between the Charge Deficiency per Anion (CDA) of structural units and the average number of bonds from the interstitial complex and adjacent structural units, <NB>, to O atoms in the corresponding structural units of uranyl oxide and uranyl oxysalt minerals. The upper and lower bounds of the distribution are used to define the characteristic range in the number of bonds accepted by a specific structural unit. **(b)** Derivation of the minimum and maximum number of bonds per anion of the structural unit from the interstitial species and adjacent structural units for a structural unit of CDA = 0.24 v.u..

Figure 17. Variation in Lewis acidity of a general interstitial complex as a function of the number of transformer (H_2O) groups per cation. The lines shown are for interstitial cations with formal charges and coordination numbers shown to the left of the plot. The range in Lewis basicity of the structural unit 0.17-0.25 v.u. is shown by the yellow box; the dashed red line shows the interpolated relation for a [9]-coordinated divalent interstitial cation. (modified after Hawthorne and Schindler, 2008).

Figure 18: Predicted versus observed number of transformer (H_2O) groups per cation for some well-refined sheet structure uranyl-oxide-oxysalt minerals.

Figure 19: Bond length–bond-valence curves for O–H bonds. The solid line is **Eq. [2]** and includes data points used for calibration. The dashed line is from Brown (1987). (after Bargar et al., 1997c).

Figure 20: Possible structures for selenite adsorbed to α-FeOOH: **(a)** an outer-sphere, ion-pair adsorption complex with the first hydration sphere shown as a shaded area; **(b)** a solid solution of selenite in the oxide phase; and **(c, d, e)** inner-sphere complexes sorbed on the goethite particle surface. Distances determined from the selenium EXAFS analysis are shown for the model structure **(e)**, which is consistent with the EXAFS data. The goethite is shown as the striped area below the line in **(e),** which represents the goethite-water interface (after Hayes et al., 1987).

Figure 21: Uptake of aqueous selenite oxyanions (solid symbols) and aqueous selenate oxyanions (hollow symbols) on goethite particle surfaces as a function of pH and ionic strength. The sorption of selenite oxyanions is not affected by increasing ionic strength (1 mM to 1000 mM $NaNO_3$), which is generally indicative of inner-sphere sorption complexes. However, selenate sorption is affected significantly by increasing ionic strength, which shifts the isotherms to lower pH. This behavior is generally indicative of outer-sphere sorption complexes (after Hayes et al., 1987).

Figure 22: Schematic illustration of $^{[4]}Pb^{2+}$ and $^{[6]}Co^{2+}$ adsorption complexes on the α-Al_2O_3(1-102) **(left-most)** and (0001) **(right)** surfaces, showing bond-valence sums (□s) to the surface oxo and hydroxo groups. The larger open circles represent oxygens, the grey circles represent Al^{3+}

ions, and the small black circles represent protons. Pb^{2+} and Co^{2+} ions are labeled (after Bargar et al., 1997a). The sum of bond valences to each surface oxygen calculated using the Brown and Altermatt (1985) bond valences for M-O bonds and the Bargar et al. (1997c) bond valences for H-O bonds is indicated above each site. This analysis suggests that Pb^{2+} does not bond to doubly-coordinated surface hydroxyl groups while Co^{2+} does (after Bargar et al., 1997c).

Figure 23: Plot of bond valence vs. bond length for Si-O, Al-O, Na-O, and Zr-O bonds using bond-valence parameters from Brown and Altermatt (1985) (from Farges et al., 1991).

Figure 24: Bond length-bond valence models for ZrO_6 polyhedra in an aluminosilicate glass/melt: **(a)** examples of unlikely geometries with over- and under-bonded oxygens; **(b)** one possible environment around ZrO_6 satisfying the Zr K-XAFS results of this study and Pauling's second rule. The sum of bond valences (Σs) at the three different types of oxygens (O_1, O_2, O_3) is shown (from Farges et al., 1991).

Figure 25: Bond length-bond valence models for ZrO_8 polyhedra in an aluminosilicate glass/melt: **(a)** examples of unlikely geometries with over- and under-bonded oxygens; **(b)** one possible environment around ZrO_8 satisfying the Zr K-edge XAFS results of this study and Pauling's second rule. Some environments are similar to that observed in the mineral zircon (outlined by dotted line) and may be responsible for an increase in Zr activity in highly polymerized melts (from Farges et al., 1991).

This is the peer-reviewed, final accepted version for American Mineralogist, published by the Mineralogical Society of America.
The published version is subject to change. Cite as Authors (Year) Title. American Mineralogist, in press.
DOI: https://doi.org/10.2138/am-2021-7938. http://www.minsocam.org/

Table 1. Comparison of Bonded (r_b), Crystal (r_c), and Ionic (r_i) Radii (r_b and r_c values from Gibbs et al., 2013b; r_i values from Shannon, 1976)

^{CN}M	⟨r_b(M)⟩	r_c(M)	ri(M)	⟨rb(O)⟩	^{CN}M	⟨rb(M)⟩	rc(M)	ri(M)	⟨rb(O)⟩
^{IV}**Al**	0.74	0.53	0.39	1.00	^{VI}**K**	1.44	1.52	1.38	1.43
^{V}**Al**	0.78	0.62	0.48	1.08	^{I}**H**	0.19	0.24	0.38	0.79
^{VI}**Al**	0.80	0.68	0.54	1.12	^{VI}**Li**	0.82	0.90	0.76	1.39
^{III}**As**$^{3+}$	0.87	0.92			^{IV}**Mg**	0.84	0.71	0.57	1.07
^{III}**B**	0.46	0.15	0.10	0.91	^{V}**Mg**	0.90	0.80	0.66	1.17
^{IV}**B**	0.49	0.25	0.11	0.99	^{VI}**Mg**	0.94	0.86	0.72	1.20
^{IV}**Be**	0.58	0.41	0.27	1.07	^{VIII}**Mg**	0.96	1.03	0.89	1.31
^{III}**C**	0.46	0.06	0.08	0.83	^{VI}**Mn**$^{2+}$	1.10	0.97	0.83	1.12
^{VI}**Ca**	1.18	1.14	1.00	1.18	^{VIII}**Mn**$^{2+}$	1.15	1.10	0.96	1.18
^{VII}**Ca**	1.22	1.20	1.06	1.23	^{III}**N**	0.60	0.04	0.10	0.64
^{VIII}**Ca**	1.25	1.26	1.12	1.27	^{V}**Na**	1.08	1.14	1.00	1.36
^{IX}**Ca**	1.25	1.32	1.18	1.26	^{VI}**Na**	1.09	1.16	1.02	1.35
^{VI}**Co**$^{2+}$	1.05	0.72	0.58	1.08	^{VII}**Na**	1.12	1.26	1.12	1.40
^{IV}**Fe**$^{2+}$	0.98	0.77	0.63	0.99	^{IV}**P**	0.63	0.31	0.17	0.91
^{VI}**Fe**$^{2+}$	1.08	0.92	0.78	1.10	^{IV}**S**	0.58	0.26	0.12	0.89
^{VIII}**Fe**$^{2+}$	1.13	1.06	0.92	1.17	^{IV}**Si**	0.67	0.40	0.26	0.95
^{IV}**Ge**	0.83	0.53	0.39	0.91	^{VI}**Si**	0.72	0.54	0.40	1.06

This is the peer-reviewed, final accepted version for American Mineralogist, published by the Mineralogical Society of America.
The published version is subject to change. Cite as Authors (Year) Title. American Mineralogist, in press.
DOI: https://doi.org/10.2138/am-2021-7938. http://www.minsocam.org/

Table 2: Comparison of selected interatomic distances (R(M-O) in Å) for the ideal hexagonal close-packed olivine structure type and the forsterite [$(Mg_{0.9}Fe_{0.10})_2SiO_4$] structure (after Brown, 1980).

SiO_4 Tetrahedron	**HCP****	**Forsterite (Fo)*****	**Δ = (HCP-Fo)**
R(Si-O)	1.690	1.637	-0.053
R(O-O)(s)[1*]	2.760	2.569	-0.191
R(O-O)(u)[2*]	2.760	2.757	-0.003
$M(1)O_6$ Octahedron			
R(M(l)-O)	1.952	2.101	0.149
R(O-O) (s,o)[3*]	2.760	2.854	0.094
R(O-O) (s,t)[4*]	2.760	2.557	-0.203
R(O-O)(u)[2*]	2.760	3.169	0.409
$M(2)O_6$ Octahedron			
R(M(2)-O)	1.952	2.135	0.183
R(O-O) (s,o)[3*]	2.760	2.854	0.094
R(O-O) (s,t)[4*]	2.760	2.593	-0.167
R(O-O) (u)[2*]	2.760	3.079	0.319
Metal-Metal Distances			
$R(M(1)_B\text{-}M(1)_B)$	2.760	2.997	0.217
$R(M(1)_B\text{-}M(2)_B)$	2.761	3.210	0.449
$R(M(1)_B\text{-}Si_B)$	2.323	2.703	0.380
$R(M(2)_B\text{-}Si_B)$	2.324	2.799	0.475

* [1](s) indicates shared edge. [2](u) indicates unshared edge. [3](s,o) indicates edge shared between octahedra. [4](s,t) indicates edge shared between octahedron and tetrahedron.

** Calculated using the cell parameters $a = 4\sqrt{3}/3\langle M\text{-}O\rangle = 4.508$Å; $b = 2\sqrt{6}\langle M\text{-}O\rangle \sim 9.563$Å; $c = 2\sqrt{2}\langle M\text{-}O\rangle \sim 5.521$Å where <M-O> is the average M-O distance. The only assumption made was that oxygen anions of 1.38 Å radius (Shannon (1976) for 4-coordinated oxygen) are in tangential contact.

***Interatomic distances for forsterite (Fo) [$(Mg_{0.9}Fe_{0.1})_2SiO_4$] are from Birle et al. (1968)

Table 3. Bond-valence table for M(2) M(1) Si_2 O_6

	2^+	2^+	4^+	∑anion
O1	$a^{x2\downarrow}$	$d^{x4\downarrow\ x2\rightarrow}$	f	2
O2	$b^{x2\downarrow}$	$e^{x2\downarrow}$	g	2
O3	$c^{x4\downarrow\ x2\rightarrow}$		$h^{x2\downarrow\ x2\rightarrow}$	2
∑cation	2	2	4	

This is the peer-reviewed, final accepted version for American Mineralogist, published by the Mineralogical Society of America.
The published version is subject to change. Cite as Authors (Year) Title. American Mineralogist, in press.
DOI: https://doi.org/10.2138/am-2021-7938. http://www.minsocam.org/

Table 4. System of equations for the a-priori bond-valences for $^{[8]}M^{2+}\,^{[6]}M^{2+}\,Si_2O_6$ clinopyroxene

v1		2	2	4	0	0	0	0	0		a		2
v2		0	0	0	4	2	0	0	0		b		2
v3		0	0	0	0	0	1	1	2		c		4
v4		1	0	0	2	0	1	0	0	x	d	=	2
v5		0	1	0	0	1	0	1	0		e		2
L1		1	-1	0	-1	1	0	0	0		f		0
L2		1	0	-1	1	-1	-2	1	1		g		0
L3		0	1	-1	0	0	0	-1	1		h		0

Table 5. A-priori bond-valences (vu), a-priori bond lengths (Å) and observed bond lengths (Å) for diopside and hedenbergite

Site		a-priori bond-valence	Diopside		Hedenbergite	
M(2)	a	0.325	2.367	2.360	2.367	2.355
	b	0.425	2.257	2.352	2.257	2.341
	c	0.125	2.758	2.561 2.717	2.758	2.627 2.719
M(1)	d	0.300	2.141	2.064 2.115	2.196	2.140 2.164
	e	0.400	2.014	2.050	2.068	2.087
Si	f	1.075	1.596	1.602	1.596	1.601
	g	1.175	1.561	1.584	1.561	1.586
	h	0.875	1.676	1.664 1.687	1.676	1.666 1.686
Reference				(1)		(2)

Ref: (1) Clark et al. (1969); (2) Cameron et al. (1973).

This is the peer-reviewed, final accepted version for American Mineralogist, published by the Mineralogical Society of America.
The published version is subject to change. Cite as Authors (Year) Title. American Mineralogist, in press.
DOI: https://doi.org/10.2138/am-2021-7938. http://www.minsocam.org/

Table 6: Brown-Altermatt Bond-Valence Analysis of Oxygen Coordination Environments in Wadsleyite (β-Mg_2SiO_4)

Oxygen Environment	Multiplicity	Bond Lengths (Å)[a]	Bond Valences (v.u.)[b]
O(1)-Mg(3)	[4]	2.129	0.417
O(1)-Mg(2)	[1]	2.035	0.397
B.V. sum			**2.065**
O(2)-Mg(2)	[1]	2.095	0.337
O(2)-Si	[2]	1.702	0.810
B.V. sum			**1.957**
O(3)-Mg(1)	[1]	2.115	0.320
O(3)-Mg(3)	[2]	2.123	0.313
O(3)-Si	[1]	1.638	0.963
B.V. sum			**1.909**
O(4)-Mg(1)	[1]	2.046	0.385
O(4)-Mg(2)	[1]	2.093	0.339
O(4)-Mg(3)	[1]	2.129	0.308
O(4)-Si	[1]	1.631	0.981
B.V. sum			**2.013**

[a] Bond lengths from Horiuchi and Sawamoto (1981)
[b] The following Brown-Altermatt (1985) bond-valence parameters were used:
r_0 (^{VI}Mg-O) = 1.693 Å; r_0 (^{IV}Si-O) = 1.624 Å

This is the peer-reviewed, final accepted version for American Mineralogist, published by the Mineralogical Society of America.
The published version is subject to change. Cite as Authors (Year) Title. American Mineralogist, in press.
DOI: https://doi.org/10.2138/am-2021-7938. http://www.minsocam.org/

Table 7. Bond-valence analyses for surface functional groups and Co^{2+} and Pb^{2+} sorption complexes on hydrated α-Al_2O_3 (0001) (Bargar et al. 1997c)

	$\Sigma^{S}_{m\text{-}o}$ at oxygen (v.u.)			
	No H-bonds	W/H bonds[a]	Oxygen coordination state[a]	Prediction
Mononuclear surface complexes				
$[^{Al}_{Al}>O^{-}]$	≤1.00	≤1.50	Unsaturated	Plausible[b]
$[^{Al}_{Al}>OH]$	≤1.88	1.81–2.13	Saturated	Most stable
$^{Al}_{Al}>O–Co$	1.35	≤1.60	Unsaturated	Plausible[b]
$^{Al}_{Al}>O–Pb$	1.53	≤1.78	Unsaturated	Plausible[b]
$^{Al}_{Al}>(OH)–Co$	≥2.03	≥2.03	Saturated	Most stable
$^{Al}_{Al}>(OH)–Pb$	≥2.21	≥2.21	Oversaturated	Doesn't occur[c]
Binuclear surface complexes[d]				
$[^{Al}_{Al}>HO_2^{+}]$	≥2.36	≥2.36	Oversaturated	Doesn't occur[c]
$^{Al}_{Al}>O<^{Co}_{Co}$	1.70	1.70	Unsaturated	Plausible[b]
$^{Al}_{Al}>O<^{Pb}_{Pb}$	2.06	2.06	Saturated	Stable

Table 8. Bond-valence analyses for surface functional groups and Co^{2+} and Pb^{2+} sorption complexes on hydrated α-Al_2O_3 (1$\bar{1}$02) (Bargar et al. 1997c)

		$\Sigma^{S}_{m\text{-}o}$ at oxygen (v.u.)			
	Mononuclear surface complexes	No H-bonds	W/H bonds[a]	Oxygen bonding state[a]	Prediction
Oxygens triply coord. by bulk Al	$[Al^{Al}{}_{Al}l\ \}\ O^{-½}]$	1.50	≤1.75	Unsaturated	Plausible[b]
	$[Al^{Al}{}_{Al}\ \}\ OH^{½}]$	≥2.18	≤2.18	Oversaturated	Doesn't occur[c]
	$Al^{Al}{}_{Al}\ \}\ O–Pb$	2.03	2.03	Saturated	Most stable
	$Al^{Al}{}_{Al}\ \}\ O–Co$	1.85	1.85	Unsaturated	Plausible[b]
Oxygens singly coord. by bulk Al	$[Al–OH^{-½}]$	≤1.38	≤1.88	Unsaturated	Plausible[b]
	$[Al–OH_2^{+½}]$	1.86–2.26	≥1.99	Saturated	Most stable

This is the peer-reviewed, final accepted version for American Mineralogist, published by the Mineralogical Society of America.
The published version is subject to change. Cite as Authors (Year) Title. American Mineralogist, in press.
DOI: https://doi.org/10.2138/am-2021-7938. http://www.minsocam.org/

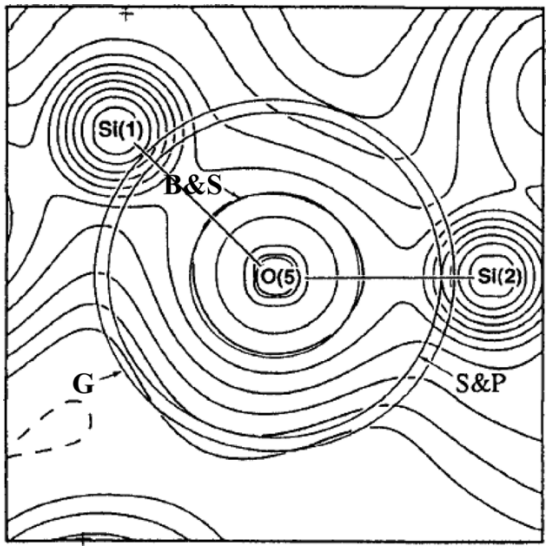

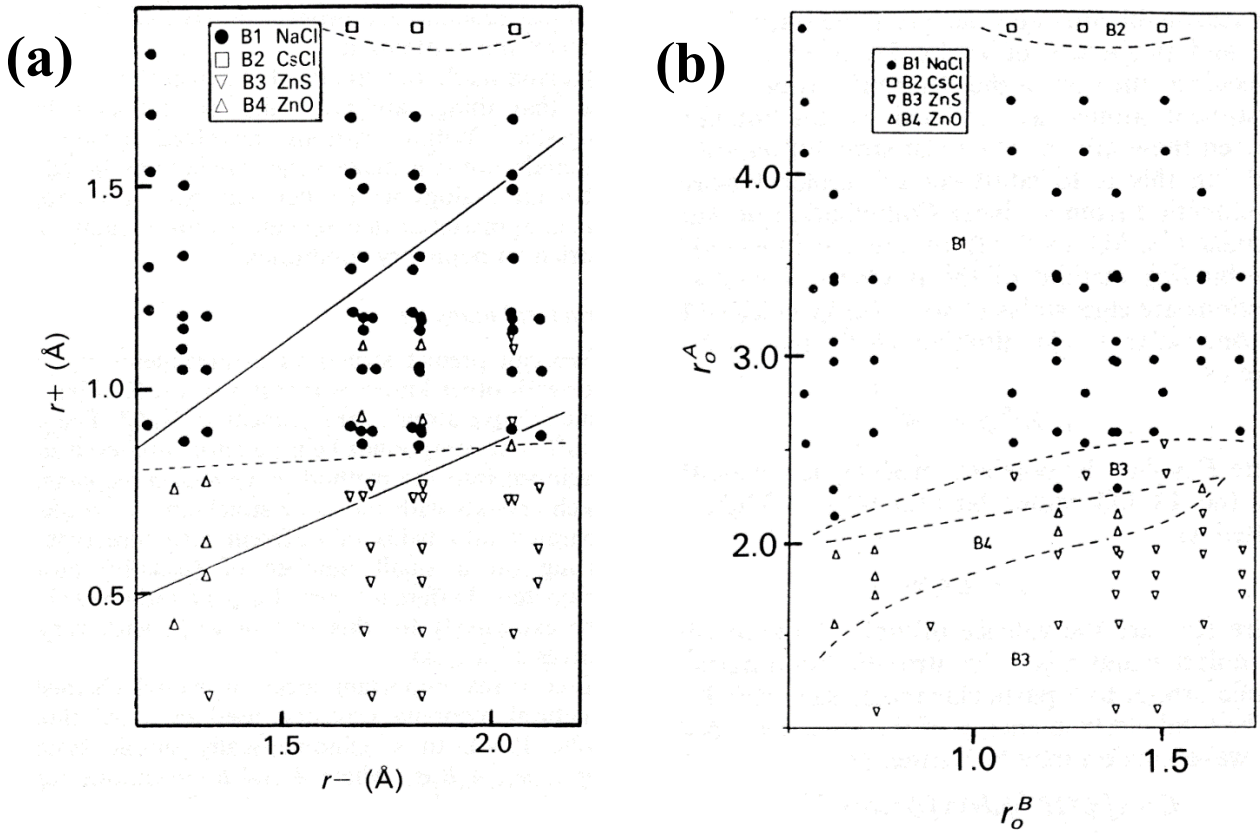

Figure 2

This is the peer-reviewed, final accepted version for American Mineralogist, published by the Mineralogical Society of America.
The published version is subject to change. Cite as Authors (Year) Title. American Mineralogist, in press.
DOI: https://doi.org/10.2138/am-2021-7938. http://www.minsocam.org/

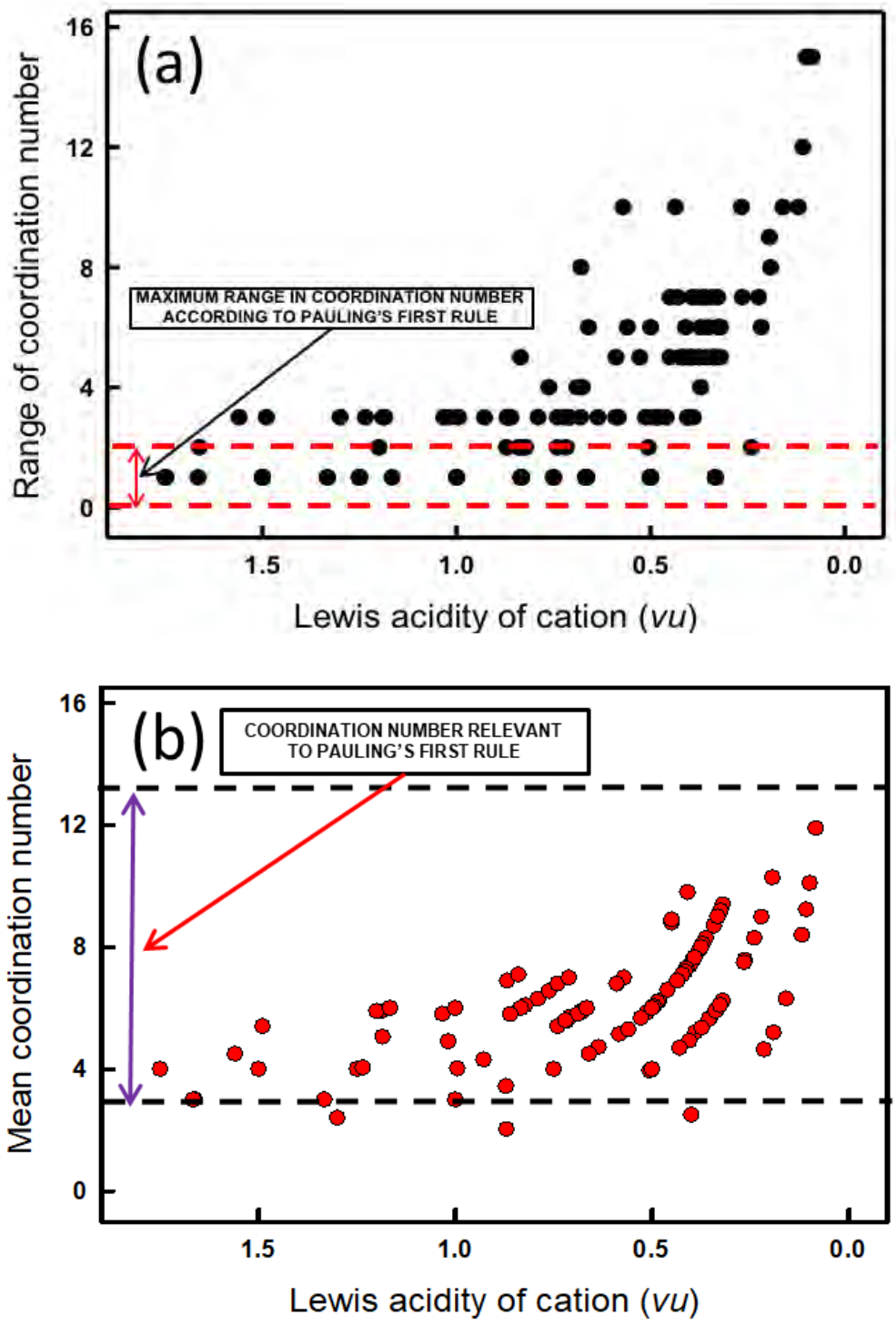

Figure 3

This is the peer-reviewed, final accepted version for American Mineralogist, published by the Mineralogical Society of America.
The published version is subject to change. Cite as Authors (Year) Title. American Mineralogist, in press.
DOI: https://doi.org/10.2138/am-2021-7938. http://www.minsocam.org/

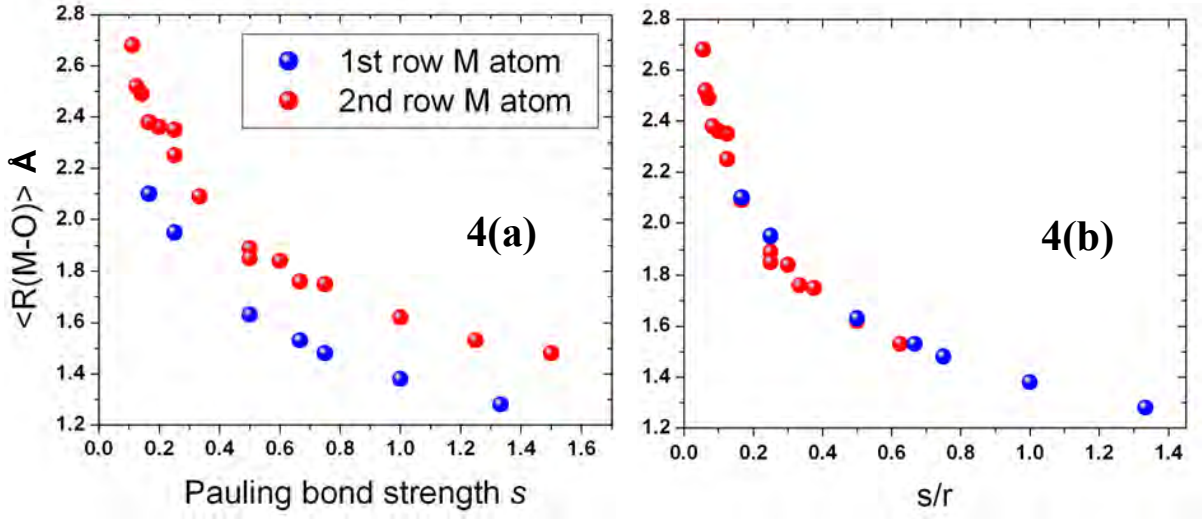

Figure 4

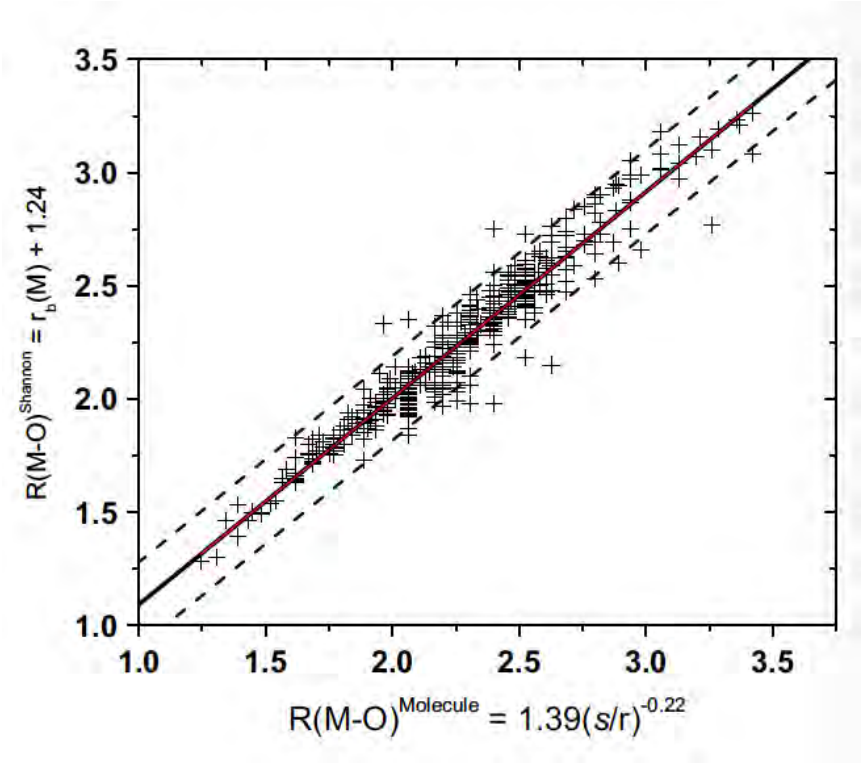

Figure 5:

This is the peer-reviewed, final accepted version for American Mineralogist, published by the Mineralogical Society of America.
The published version is subject to change. Cite as Authors (Year) Title. American Mineralogist, in press.
DOI: https://doi.org/10.2138/am-2021-7938. http://www.minsocam.org/

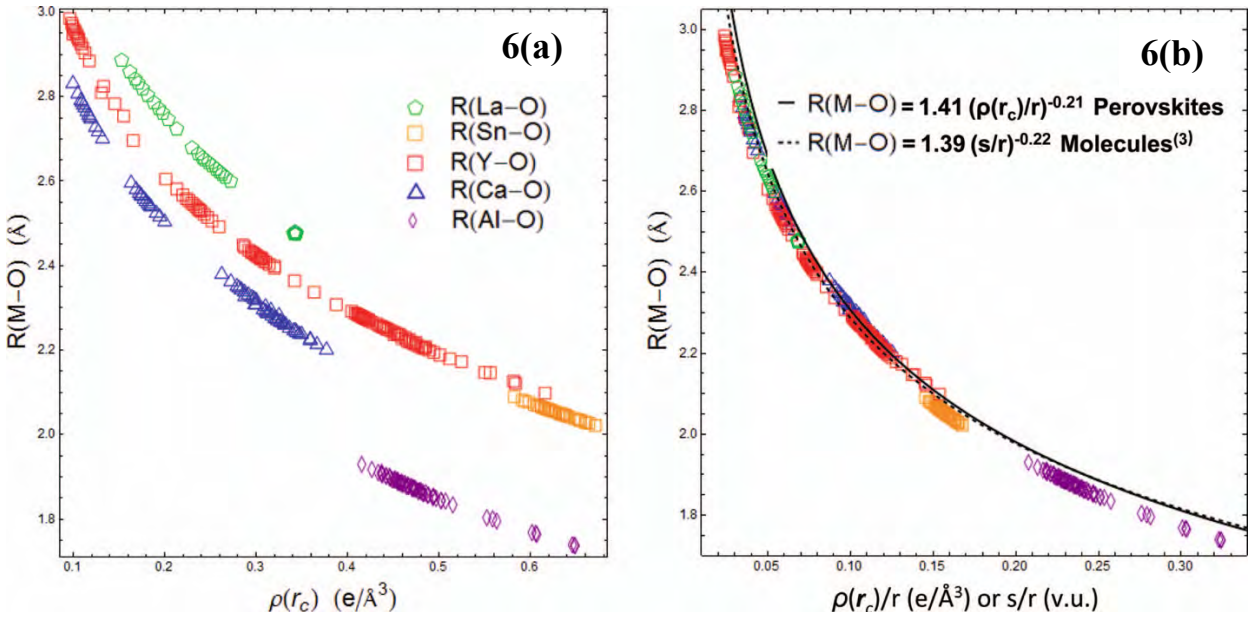

Figure 6

This is the peer-reviewed, final accepted version for American Mineralogist, published by the Mineralogical Society of America.
The published version is subject to change. Cite as Authors (Year) Title. American Mineralogist, in press.
DOI: https://doi.org/10.2138/am-2021-7938. http://www.minsocam.org/

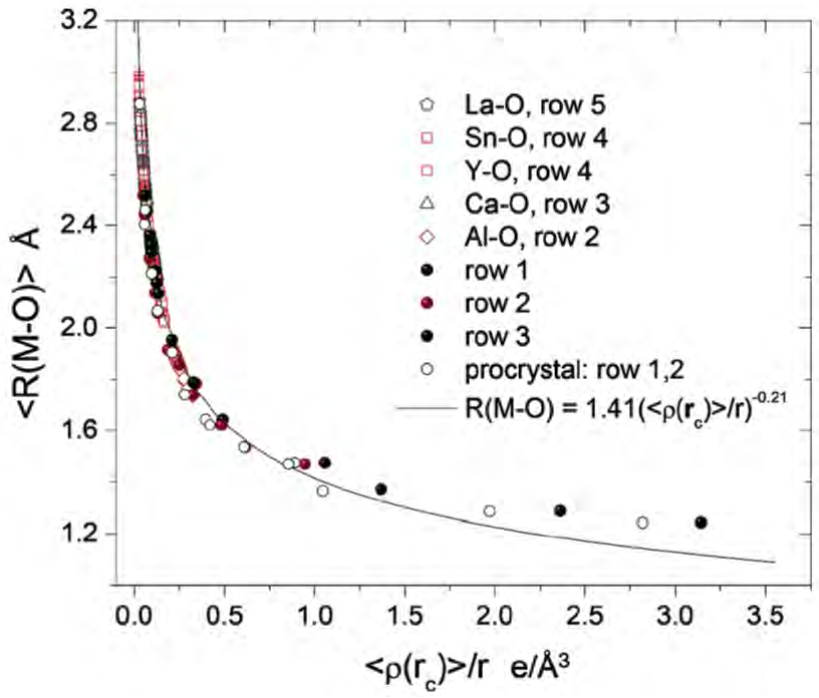

Figure 7:

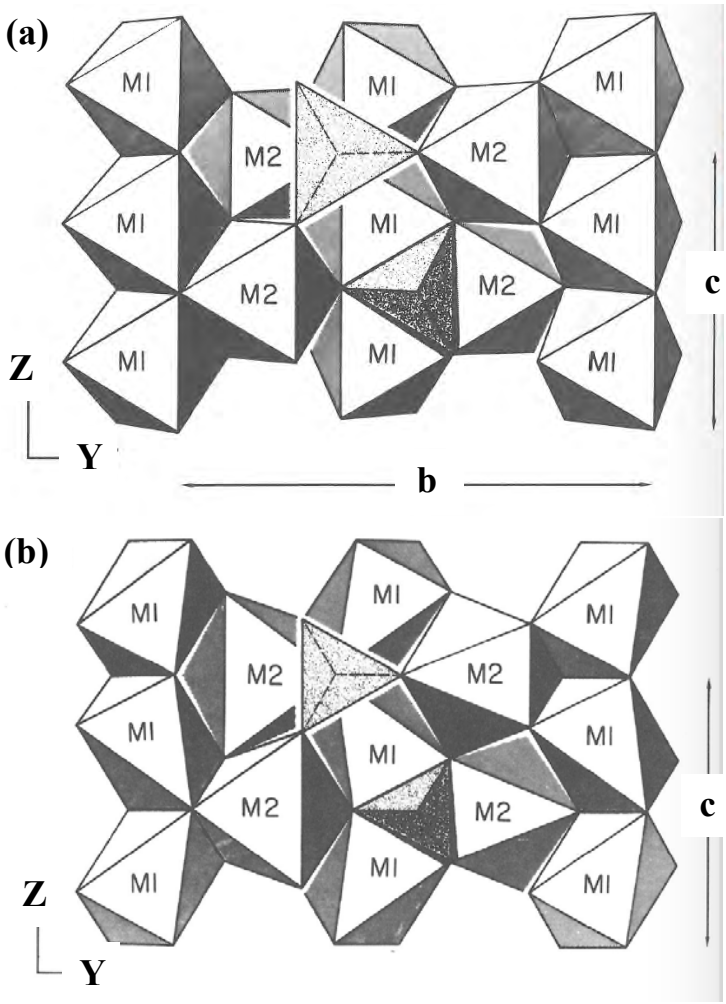

Figure 8:

This is the peer-reviewed, final accepted version for American Mineralogist, published by the Mineralogical Society of America.
The published version is subject to change. Cite as Authors (Year) Title. American Mineralogist, in press.
DOI: https://doi.org/10.2138/am-2021-7938. http://www.minsocam.org/

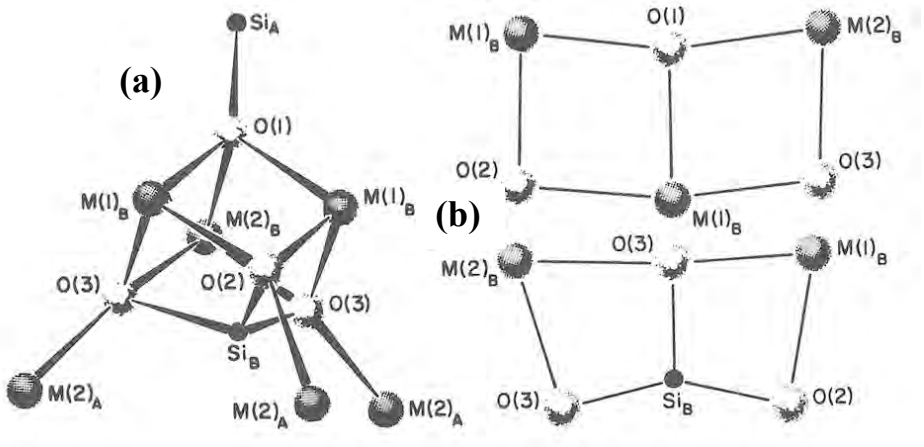

Figure 9:

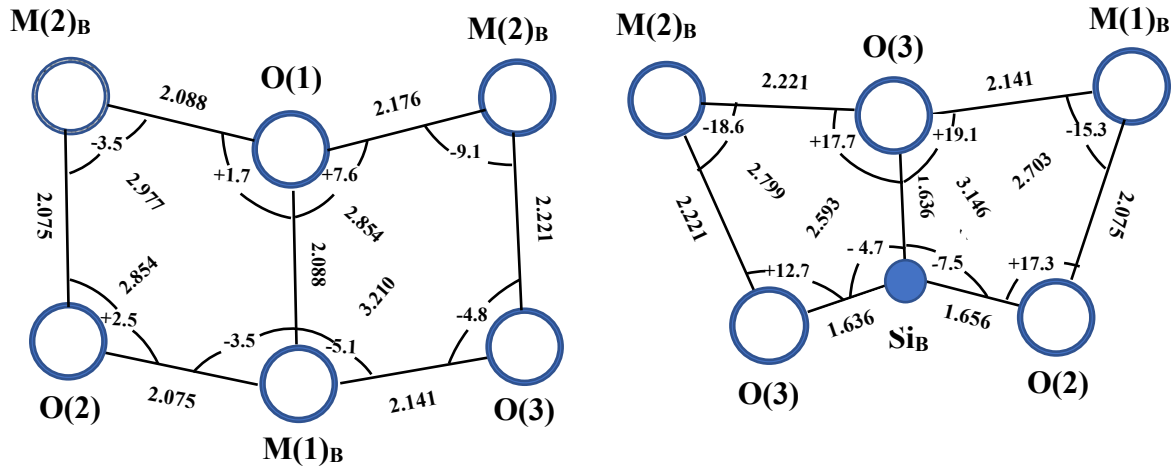

Figure 10:

This is the peer-reviewed, final accepted version for American Mineralogist, published by the Mineralogical Society of America.
The published version is subject to change. Cite as Authors (Year) Title. American Mineralogist, in press.
DOI: https://doi.org/10.2138/am-2021-7938. http://www.minsocam.org/

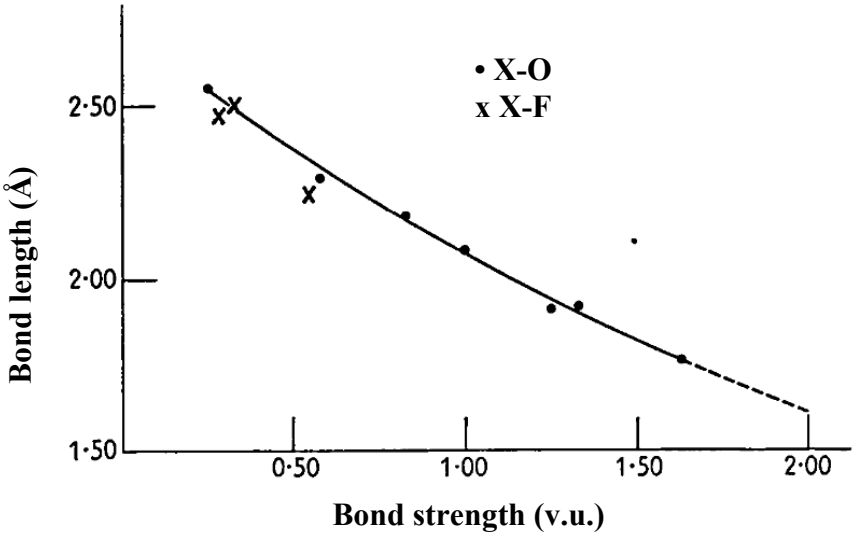

Figure 11:

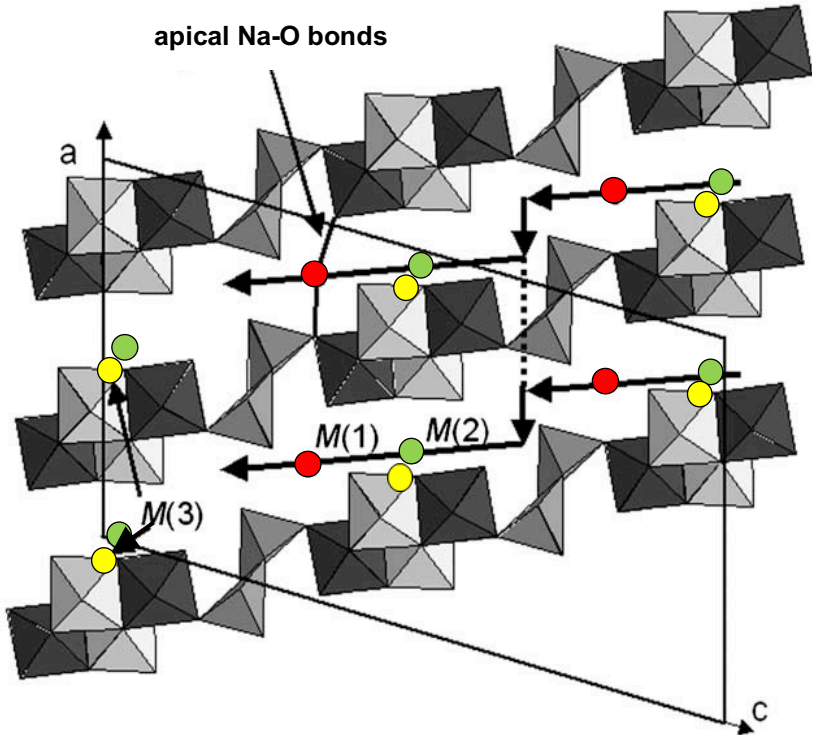

Figure 12.

This is the peer-reviewed, final accepted version for American Mineralogist, published by the Mineralogical Society of America.
The published version is subject to change. Cite as Authors (Year) Title. American Mineralogist, in press.
DOI: https://doi.org/10.2138/am-2021-7938. http://www.minsocam.org/

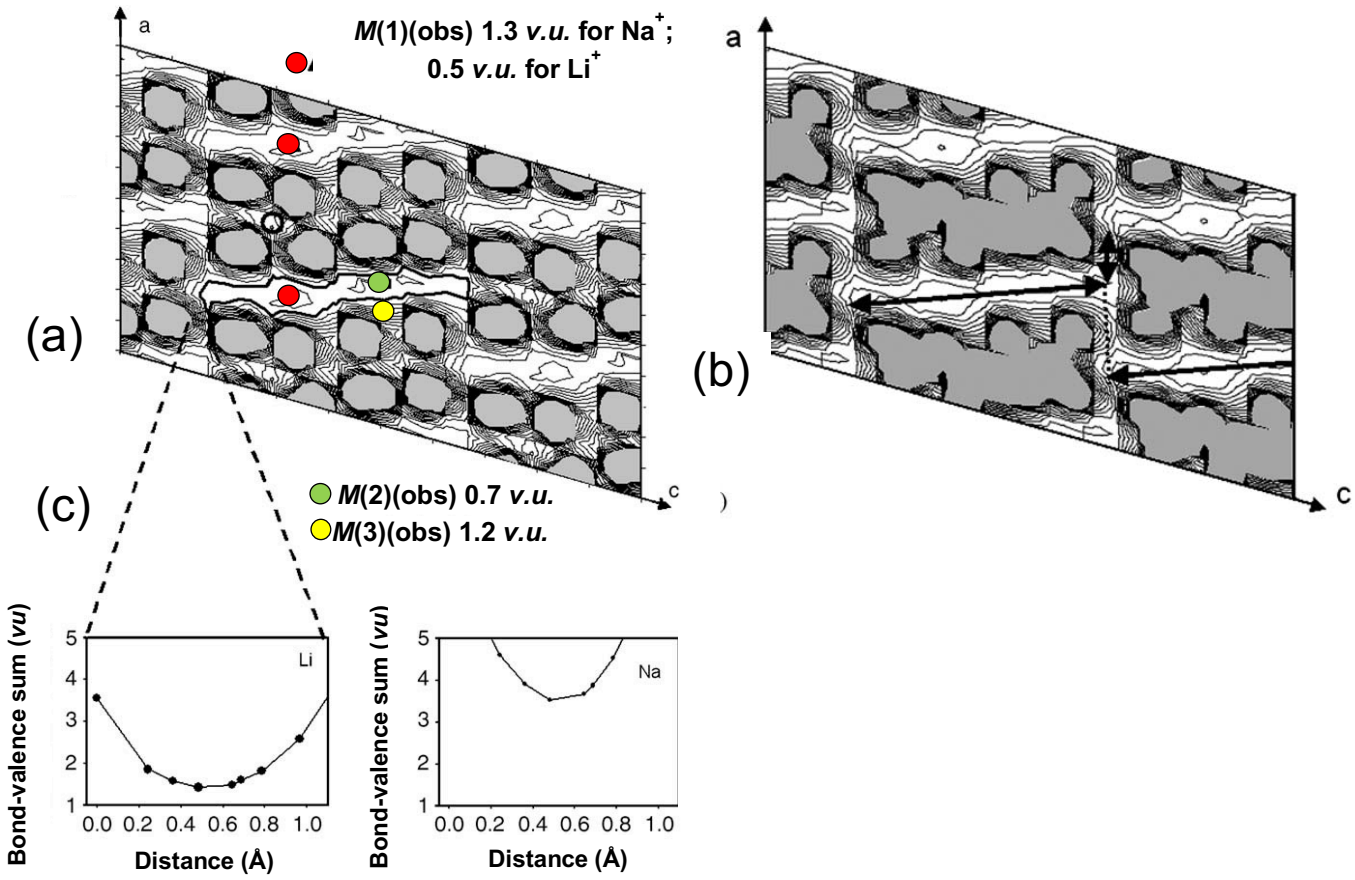

Figure 13.

This is the peer-reviewed, final accepted version for American Mineralogist, published by the Mineralogical Society of America.
The published version is subject to change. Cite as Authors (Year) Title. American Mineralogist, in press.
DOI: https://doi.org/10.2138/am-2021-7938. http://www.minsocam.org/

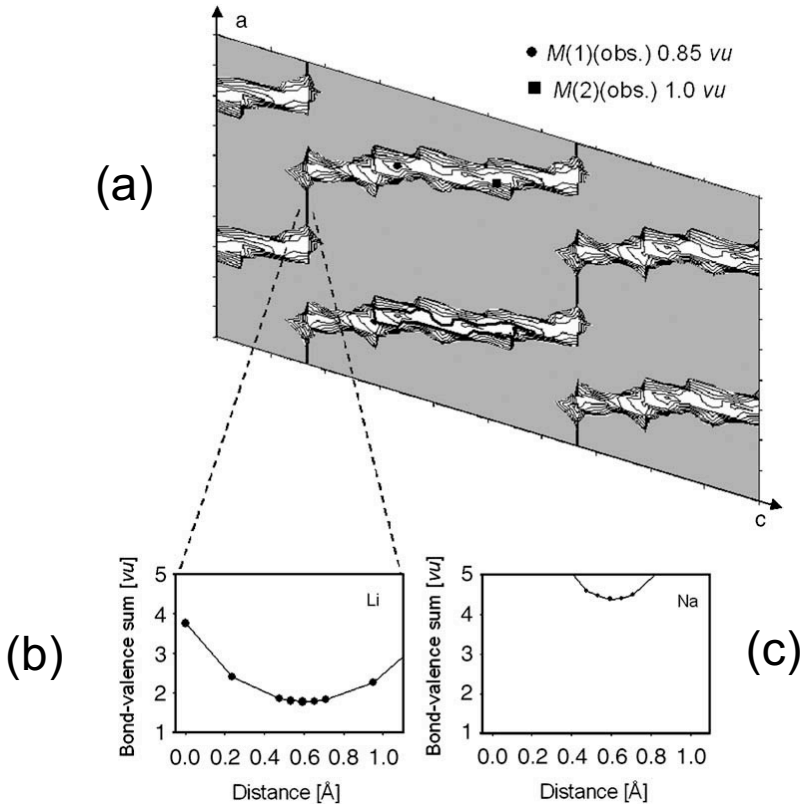

Figure 14.

This is the peer-reviewed, final accepted version for American Mineralogist, published by the Mineralogical Society of America.
The published version is subject to change. Cite as Authors (Year) Title. American Mineralogist, in press.
DOI: https://doi.org/10.2138/am-2021-7938. http://www.minsocam.org/

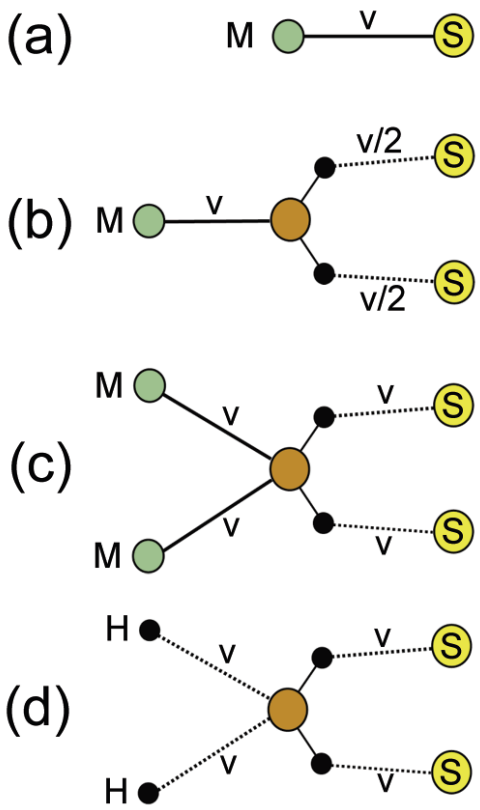

Figure 15: The bond-valence structure around (H_2O) as a function of local bond-topology; (**a**) a cation, C (green) bonded to an anion, S (yellow) with bond valence v v.u.; (**b**) a cation bonded to an (H_2O) group (O = orange; H = black) with bond valence v v.u.; the H atoms hydrogen-bond to the anions S with bond valence v/2 v.u. per bond; (**c**) two cations bonded to an (H_2O) group with bond valence v.u. per bond; the H atoms hydrogen-bond to the anions S with bond valence **v** v.u. per bond; (**d**) two H atoms hydrogen-bonded to an (H_2O) group with bond valence v v.u. per bond; the H atoms of the (H_2O) group hydrogen-bond to the anions S with bond valence v v.u. per bond.

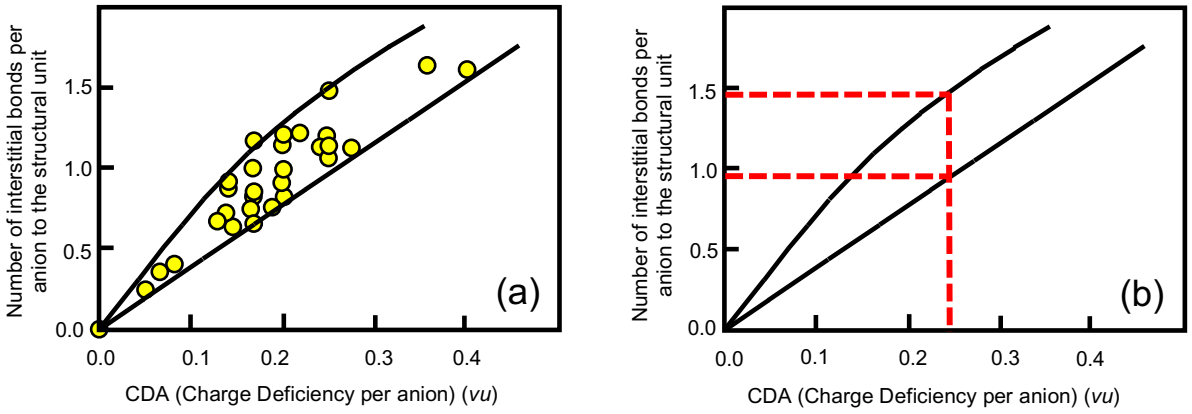

Figure 16: (a) Correlation between the Charge Deficiency per Anion (CDA) of structural units and the average number of bonds from the interstitial complex and adjacent structural units, <NB>, to O atoms in the corresponding structural units of uranyl oxide and uranyl oxysalt minerals. The upper and lower bounds of the distribution are used to define the characteristic range in the number of bonds accepted by a specific structural unit. **(b)** Derivation of the minimum and maximum number of bonds per anion of the structural unit from the interstitial species and adjacent structural units for a structural unit of CDA = 0.24 v.u..

This is the peer-reviewed, final accepted version for American Mineralogist, published by the Mineralogical Society of America.
The published version is subject to change. Cite as Authors (Year) Title. American Mineralogist, in press.
DOI: https://doi.org/10.2138/am-2021-7938. http://www.minsocam.org/

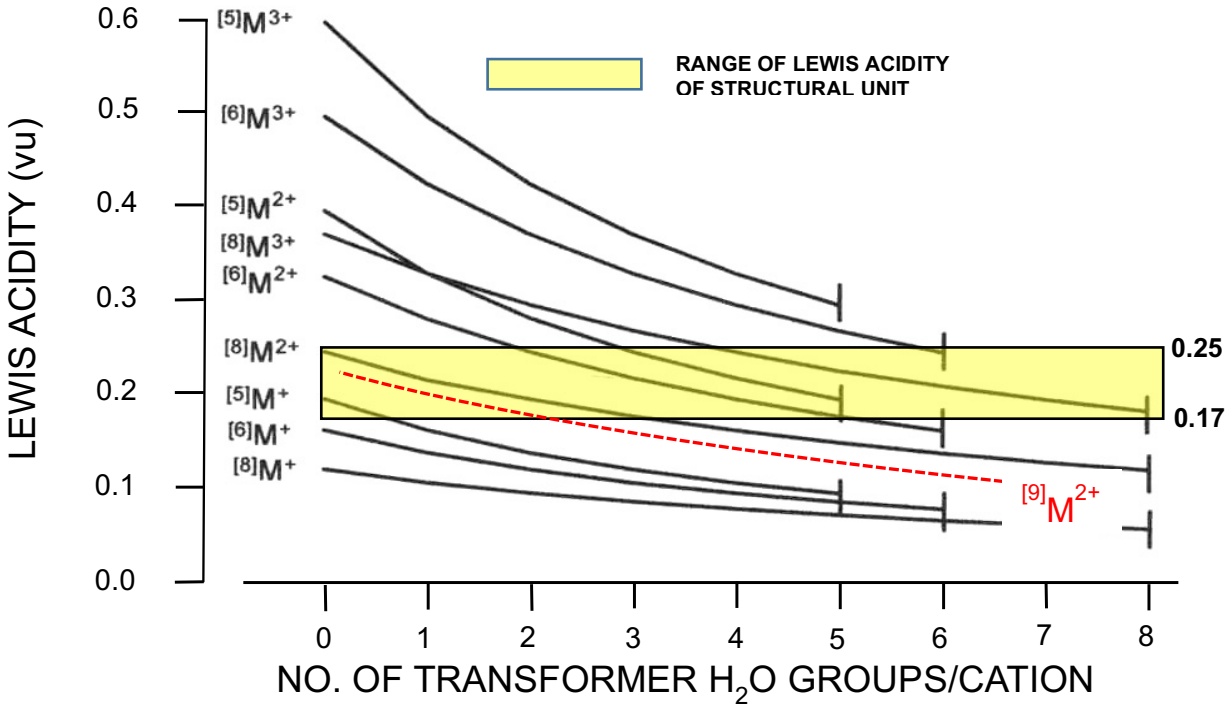

Figure 17. Variation in Lewis acidity of a general interstitial complex as a function of the number of transformer (H_2O) groups per cation. The lines shown are for interstitial cations with formal charges and coordination numbers shown to the left of the plot. The range in Lewis basicity of the structural unit 0.17-0.25 v.u. is shown by the yellow box; the dashed red line shows the interpolated relation for a [9]-coordinated divalent interstitial cation. Modified after Hawthorne and Schindler (2008).

This is the peer-reviewed, final accepted version for American Mineralogist, published by the Mineralogical Society of America.
The published version is subject to change. Cite as Authors (Year) Title. American Mineralogist, in press.
DOI: https://doi.org/10.2138/am-2021-7938. http://www.minsocam.org/

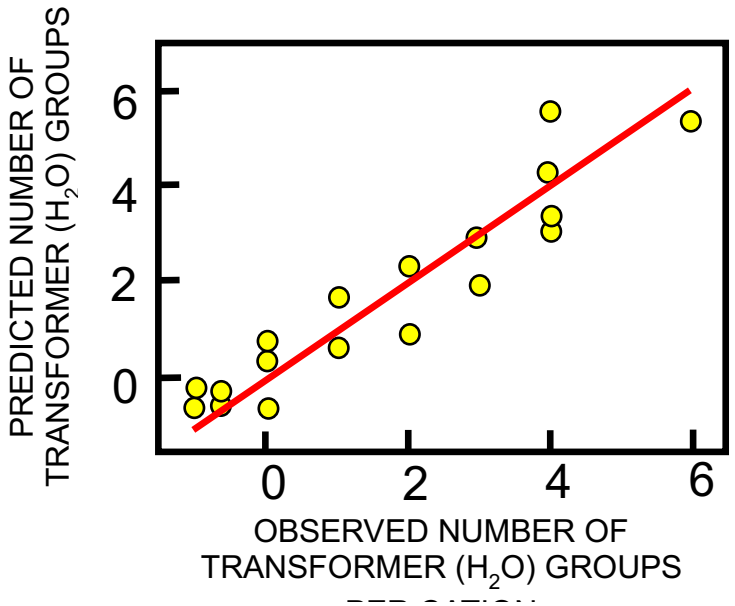

Figure 18:

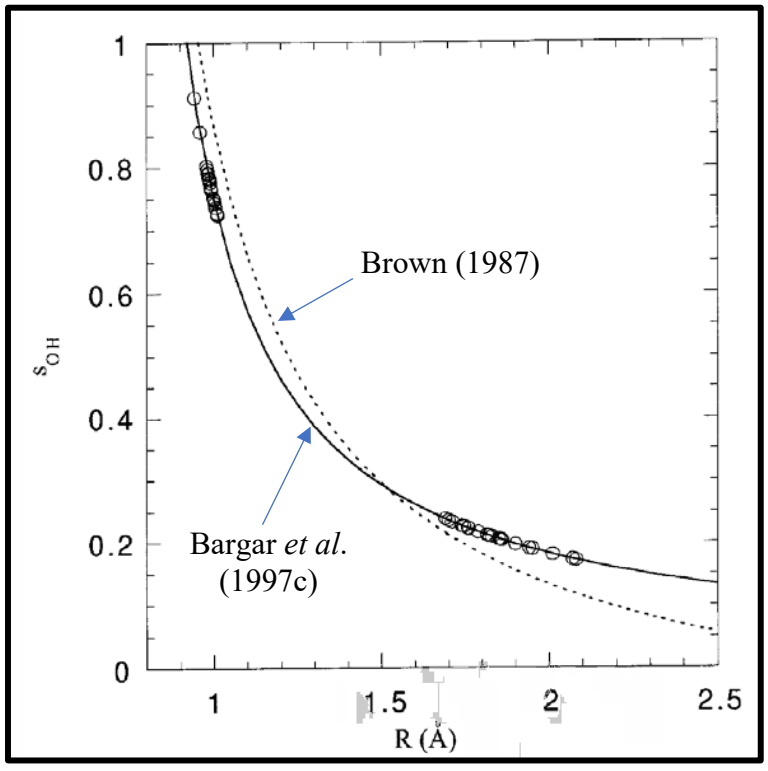

Figure 19:

This is the peer-reviewed, final accepted version for American Mineralogist, published by the Mineralogical Society of America.
The published version is subject to change. Cite as Authors (Year) Title. American Mineralogist, in press.
DOI: https://doi.org/10.2138/am-2021-7938. http://www.minsocam.org/

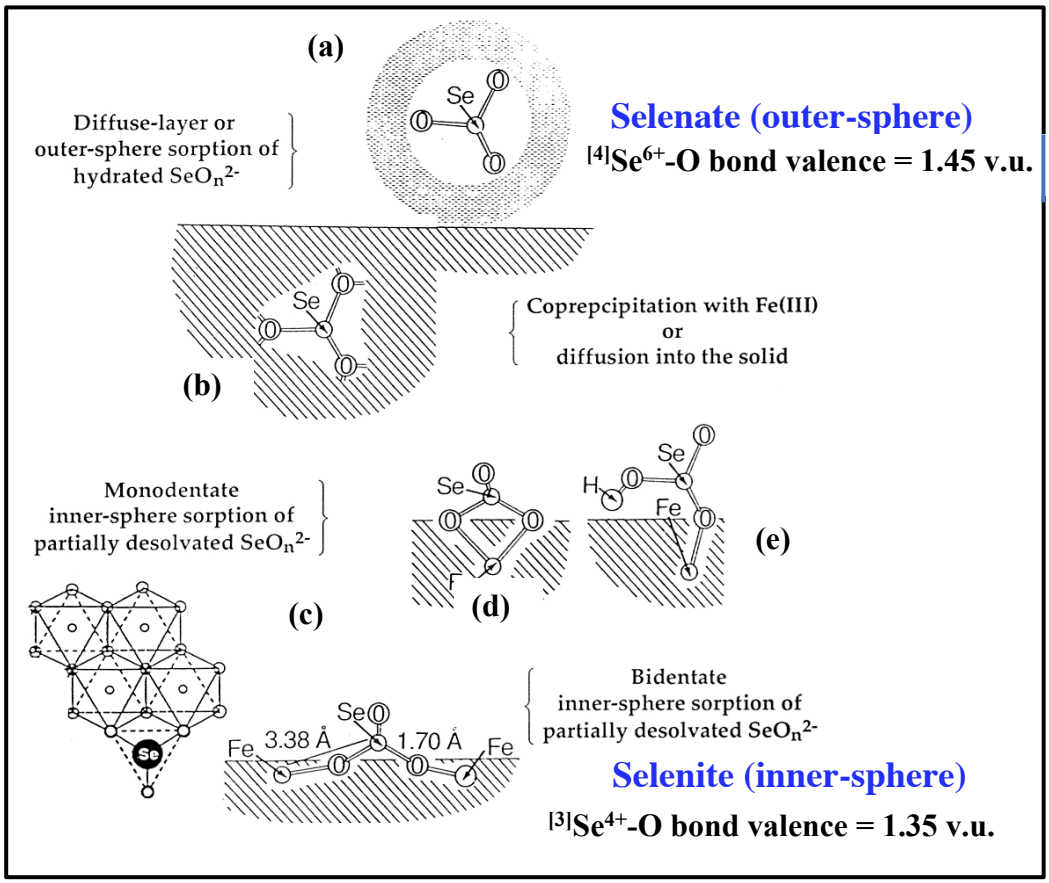

Figure 20:

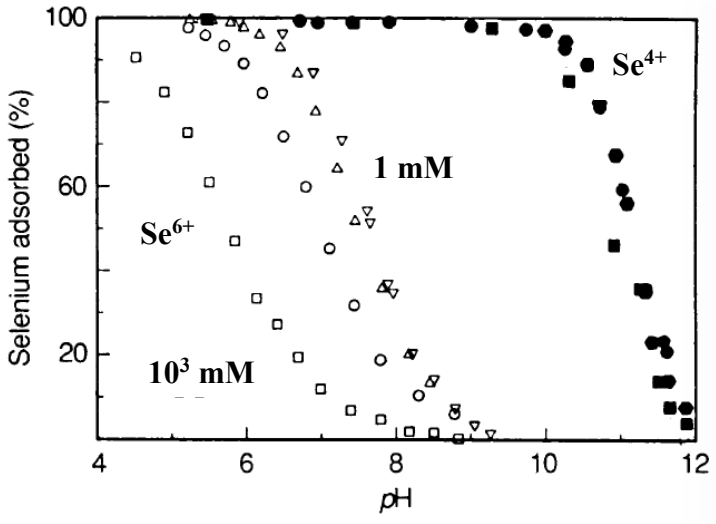

Figure 21:

This is the peer-reviewed, final accepted version for American Mineralogist, published by the Mineralogical Society of America.
The published version is subject to change. Cite as Authors (Year) Title. American Mineralogist, in press.
DOI: https://doi.org/10.2138/am-2021-7938. http://www.minsocam.org/

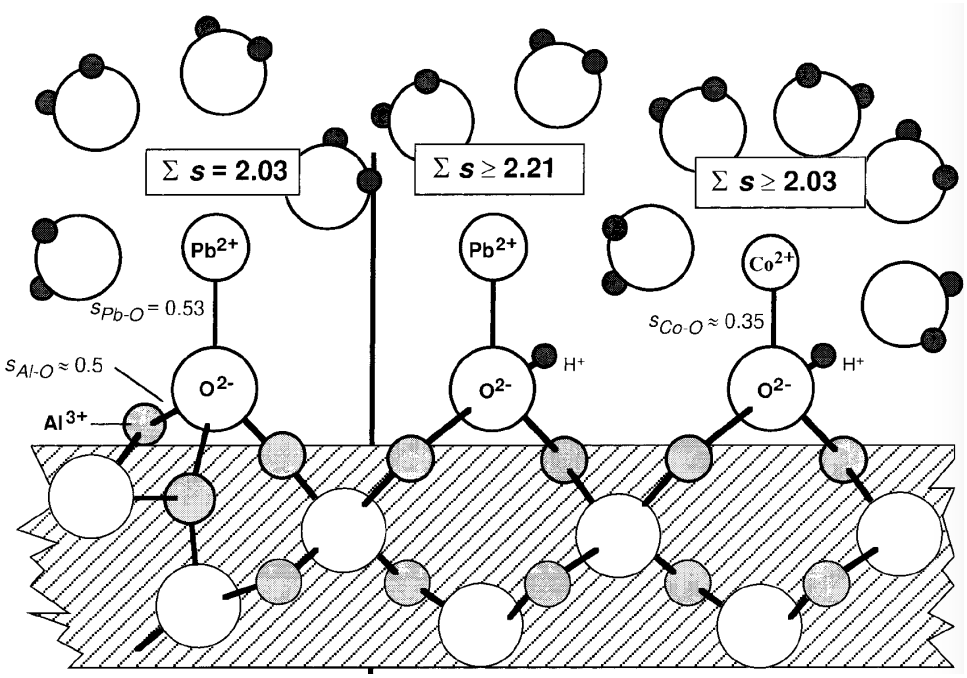

Figure 22:

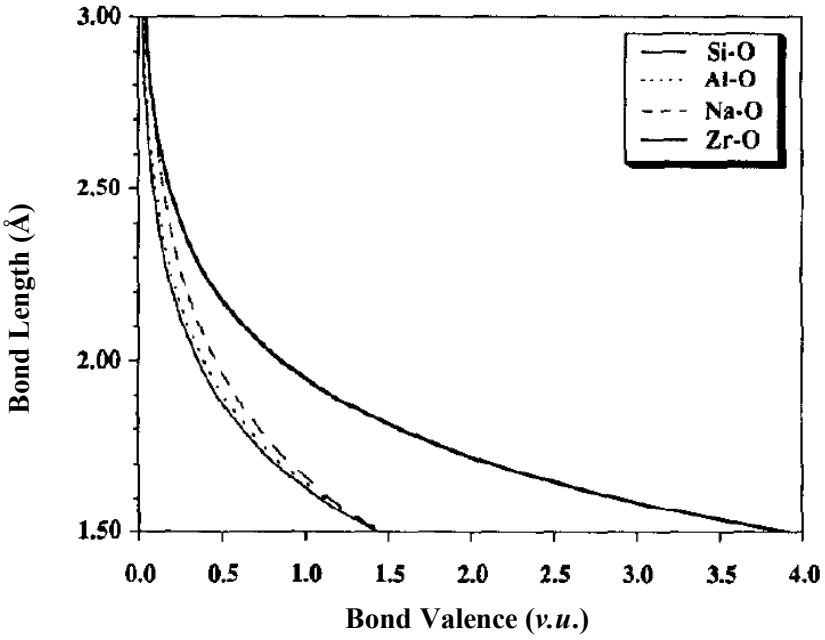

Figure 23:

This is the peer-reviewed, final accepted version for American Mineralogist, published by the Mineralogical Society of America.
The published version is subject to change. Cite as Authors (Year) Title. American Mineralogist, in press.
DOI: https://doi.org/10.2138/am-2021-7938. http://www.minsocam.org/

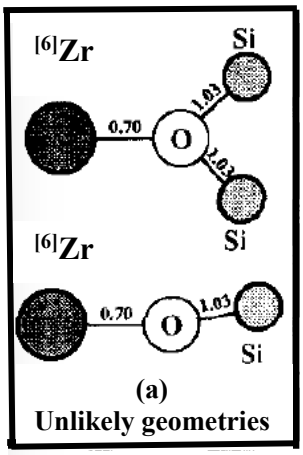

(b)

$s(O_1) = 1.97$

$s(O_2) = 1.90$

$s(O_3) = 1.92$

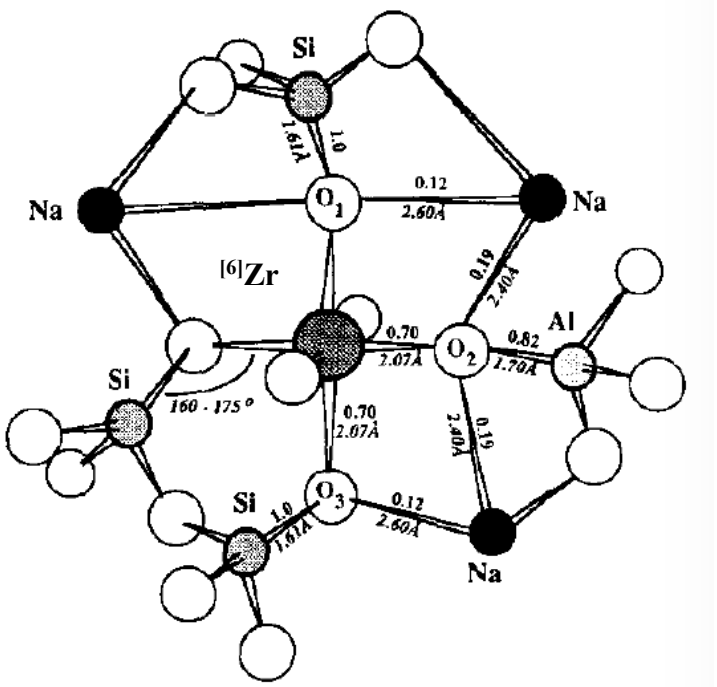

Figure 24:

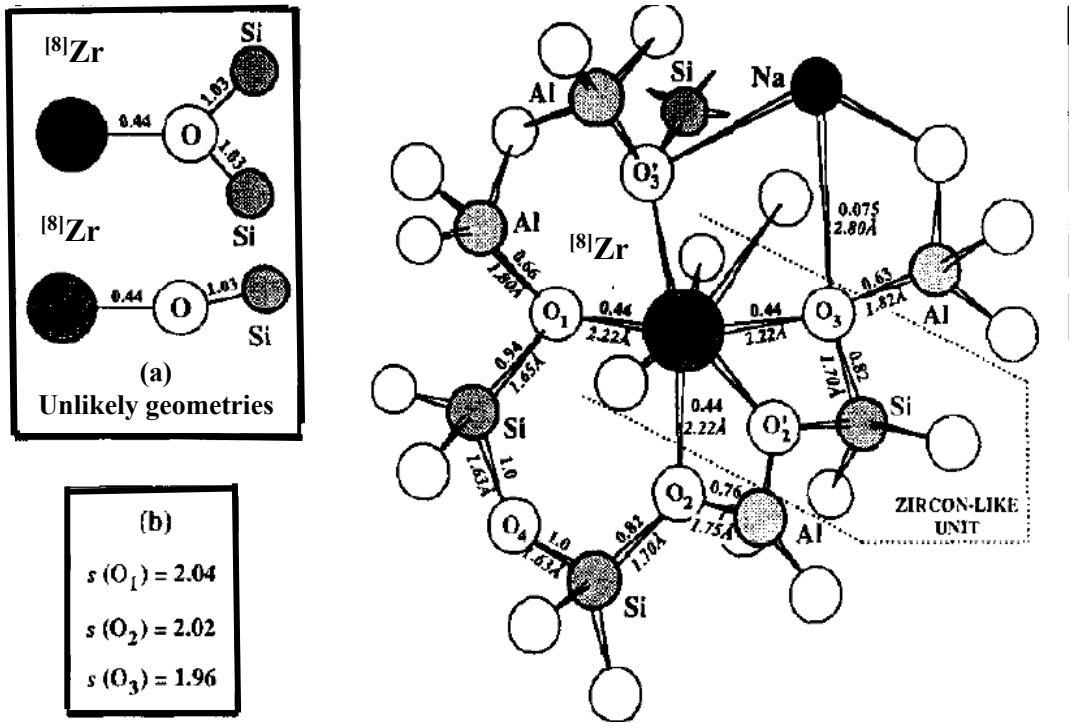

Figure 25: